

*Digital Comprehensive Summaries of Uppsala Dissertations
from the Faculty of Science and Technology 2276*

Molecular Copper and Ruthenium Water Oxidation Electrocatalysts for Light-Driven Water Splitting

LUDOVICO RICCARDI



ACTA UNIVERSITATIS
UPSALIENSIS
2023

ISSN 1651-6214
ISBN 978-90-386-5743-1
urn:nbn:se:uu:diva-501240



UPPSALA
UNIVERSITET

Dissertation presented at Uppsala University to be publicly examined in Senaatszaal: Auditorium, De Zaaie, Eindhoven, Tuesday, 30 May 2023 at 13:30 for the degree of Doctor of Philosophy. The examination will be conducted in English. Faculty examiner: Jarl Van der Vlugt (University of Oldenburg, Germany).

Abstract

Riccardi, L. 2023. Molecular Copper and Ruthenium Water Oxidation Electrocatalysts for Light-Driven Water Splitting. *Digital Comprehensive Summaries of Uppsala Dissertations from the Faculty of Science and Technology* 2276. 154 pp. Eindhoven: Technische Universiteit Eindhoven. ISBN 978-90-386-5743-1.

In recent years, there has been a growing awareness of the need to transition to renewable energy to mitigate the effects of climate change and reduce greenhouse gas emissions. Governments, businesses, and individuals are investing in renewable energy infrastructure and technologies to create a more sustainable energy future. This thesis explores transition metal-based molecular complexes for water oxidation catalysis and their integration into water-splitting devices. Water oxidation (WO) is a key reaction in all processes intended to produce chemical fuels from water. When water splitting is driven by solar light, it is also referred to as artificial photosynthesis.

The work focuses on a molecular copper catalyst with a tetra-amidate macrocyclic ligand (TAML), called [CuMac]²⁻, which can be isolated as a (Me₄N)₂[CuMac] salt. Derivatives of the organic ligand scaffold bearing either two ester or two carboxylic acid functionalities were synthesized to enable heterogenization of [CuMac]²⁻. The compounds were evaluated for their oxygen evolution reaction (OER) activity at different operational pH. However, introducing the carboxylic moieties appeared to be kinetically detrimental to the OER activity compared to that of the parent [CuMac]²⁻. A study on identifying possible short-lived intermediates in the catalytic cycle of [CuMac]²⁻ is presented. UV-visible transient absorption spectroscopy was used to deduce the electron transfer mechanism and kinetics of catalyst oxidation in an attempt to understand the catalytic cycle's early steps. Using [Ru(bpy)₃]Cl₂ and persulfate as the photosensitizer and the oxidative quencher, respectively, flash-photolysis was employed to gather evidence of the one-electron oxidized catalyst and to follow intermediates that could previously not be resolved temporally by electrochemical means.

Printed electrodes (PEs) were fabricated using graphite as the conductive material and a polymer binder P(MMA-*s*-HEMA). The PEs were then covalently functionalized with [CuMac]²⁻ using an in-situ electroreduction of the corresponding bis(diazonium) compound (N₂)₂[CuMac]. The resulting heterogenized catalyst's activity was evaluated by cyclic voltammetry to find that it was impeded compared to that of [CuMac]²⁻ in homogeneous solution phase.

Finally, a ruthenium-based coordination oligomer water oxidation catalyst was integrated into a flow-electrolyzer powered by a perovskite/perovskite tandem solar cell to drive water splitting by light. An operational voltage of 1.4 V was achieved, and a solar-to-hydrogen efficiency (STH) of 12.5 %. However, the stability of the system remains to be improved, which could be achieved by changing the membrane separating the two electrolyte compartments. Such adjustments can fine-tune the local pH surrounding the catalyst, which is an essential parameter for catalyst activity and integrity.

Keywords: Water oxidation, Molecular catalyst, Electrocatalyst, Water splitting, Electrolyzer

Ludovico Riccardi, Department of Chemistry - Ångström, Synthetic Molecular Chemistry, 523, Uppsala University, SE-751 20 Uppsala, Sweden.

© Ludovico Riccardi 2023

ISSN 1651-6214

ISBN 978-90-386-5743-1

URN urn:nbn:se:uu:diva-501240 (<http://urn.kb.se/resolve?urn=urn:nbn:se:uu:diva-501240>)

Molecular Copper and Ruthenium Water Oxidation Electrocatalysts for Light-Driven Water Splitting

PROEFSCHRIFT

ter verkrijging van de graad van doctor aan de Technische Universiteit
Eindhoven, op gezag van de rector magnificus prof.dr. S. Lenaerts,
voor een commissie aangewezen door het College voor Promoties, in
het openbaar te verdedigen op dinsdag 30 mei 2023 om 13:30 uur

door

Ludovico Riccardi

geboren te Verbania, Italië

Dit proefschrift is goedgekeurd door de promotoren en de samenstelling van de promotiecommissie is als volgt:

Voorzitter: prof.dr. E.W. Meijer

1^e promotor: prof.dr.ir. R.A.J. Janssen

2^e promotor: prof.dr. S. Ott (Uppsala University)

Leden: prof.dr. J.N.H. Reek (Universiteit van Amsterdam)
 prof.dr.ir J.I. van der Vlugt (University of Oldenburg)
 prof.dr. E. Borbas (Uppsala University)
 prof.dr. R.P. Sijbesma
 prof.dr.ir. A.R.A. Palmans

Het onderzoek in dit proefschrift wordt beschreven is uitgevoerd in overeenstemming met de TU/e Gedragscode Wetenschapsbeoefening.

MOLECULAR COPPER AND RUTHENIUM WATER
OXIDATION ELECTROCATALYSTS FOR LIGHT-DRIVEN
WATER SPLITTING

Ludovico Riccardi

Printed by: Proefschrift Specialist
Dutch summary translated by: Guus Aalbers
Swedish summary translated by: Martin Axelsson

The research is part of the European School on artificial leaf: electronics and Devices (eSCALED) program. The project has received funding from the European Union's Horizon 2020 research and innovation program under grant agreement No. 765376. This work has also received funding from the Spinoza.

The extensive research presented in this thesis was conducted by the author of this work.

A catalogue record is available from the Eindhoven University of Technology Library
ISBN: 978-90-386-5743-1

TABLE OF CONTENTS

1. INTRODUCTION	11
1.1 ENERGY TRANSITION	11
1.2 SOLAR FUELS AND WATER SPLITTING	12
1.3 eSCALED PROJECT AND THESIS AIM	14
1.4 WATER OXIDATION	15
1.4.1 MOLECULAR CATALYSTS	15
1.4.2 HETEROGENIZATION OF MOLECULAR CATALYSTS	17
1.5 SOLAR DRIVEN ELECTROLYSIS	18
1.5.1 PV-EC VS. PEC CONFIGURATIONS	19
1.6 REFERENCES	21
2. THEORY AND TECHNIQUES	25
2.1 VOLTAMMETRY	25
2.1.1 ELECTROCHEMISTRY INTRODUCTION	25
2.1.2 CYCLIC VOLTAMMETRY	27
2.2 TIME-RESOLVED SPECTROSCOPY	32
2.2.1 TIME-CORRELATED SINGLE-PHOTON COUNTING	34
2.2.2 PUMP-PROBE SPECTROSCOPY	36
2.3 SOLAR CELL CHARACTERIZATION	40
2.3.1 PHOTO-TO-ELECTRICAL ENERGY	40
2.3.2 SOLAR CELL EFFICIENCY	41
2.3.3 MULTIJUNCTION PV	43
2.4 PV-EC DESIGN AND CHARACTERIZATION	44
2.4.1 H ₂ CONVERSION THERMODYNAMICS	44
2.5 REFERENCES	46
3. TETRA-AMIDATE MACROCYCLIC LIGAND COPPER-BASED WATER OXIDATION CATALYSTS	49
3.1 INTRODUCTION	49
3.2 RESULTS AND DISCUSSION	51

3.2.1 MATERIAL SYNTHESIS AND CHARACTERIZATION	51
3.2.2 ELECTROCHEMICAL AND OPTICAL PROPERTIES	53
3.2.3 CATALYST STABILITY AND EVALUATION OF WATER OXIDATION REACTION	60
3.3 CONCLUSION	62
3.4 EXPERIMENTAL DETAILS	63
3.5 REFERENCES	69

4. MECHANISTIC INVESTIGATION OF THE PHOTO-OXIDATION OF [CuMac]²⁻ **71**

4.1 INTRODUCTION	71
4.2 RESULTS	74
4.2.1 [Ru(BPY) ₃] ²⁺ /Na ₂ S ₂ O ₈ PHOTOLUMINESCENCE QUENCHING	74
4.2.2 FLASH-PHOTOLYSIS: [CuMac] ²⁻ OXIDATION	80
4.3 CONCLUSIONS	85
4.4 EXPERIMENTAL DETAILS	87
4.5 REFERENCES	88

5. IMMOBILIZATION OF A MOLECULAR Cu-BASED WOC ON PRINTED ELECTRODES THROUGH COVALENT INTERACTION **91**

5.1 INTRODUCTION	91
5.1.1 HETEROGENIZATION: DIAZONIUM GRAFTING	91
5.1.2 NITROXIDE-MEDIATED RADICAL POLYMERIZATION	93
5.1.3 SCREEN-PRINTING TECHNOLOGY	95
5.2 RESULTS AND DISCUSSION	96
5.2.1 POLYMERIZATION OF THE BINDER	96
5.2.2 FABRICATION OF PRINTED ELECTRODES (PES)	98
5.2.3 dNH ₂ MAC SYNTHESIS AND COVALENT GRAFTING	105
5.2.4 NOVEL ANODE MATERIAL STABILITY AND ACTIVITY	107
5.3 CONCLUSIONS	110
5.4 EXPERIMENTAL METHODS	110
5.5 REFERENCES	114

<u>6. RUTHENIUM COORDINATION OLIGOMER-BASED ANODE FOR PHOTOELECTROCHEMICAL WATER OXIDATION USING A TANDEM SOLAR CELL</u>	117
6.1 INTRODUCTION	117
6.2 RESULTS	119
6.2.1 RU-BDA OLIGOMER: ANODE PREPARATION AND CHARACTERIZATION	119
6.2.2 STABILITY AND PERFORMANCE OF THE FLOW-ELECTROLYZER	121
6.2.3 PV-POWERED HYDROGEN /OXYGEN EVOLUTION	124
6.3 CONCLUSIONS	127
6.4 EXPERIMENTAL DETAILS	128
6.5 REFERENCES	130
<u>7. OUTLOOK</u>	133
<u>SUMMARY</u>	137
<u>SUMMARY (SWEDISH)</u>	141
<u>SUMMARY (DUTCH)</u>	145
<u>CURRICULUM VITAE</u>	149
<u>ACKNOWLEDGMENTS</u>	151

List of Abbreviations

2-PACz [2-(9 <i>H</i> -carbazol-9-yl)ethyl] phosphonic acid	GDL gas diffusion layer
AEM anion exchange membrane	GHG greenhouse gas
AFM atomic force microscopy	GS ground state
ALD atomic layer deposition	HEMA (hydroxyethyl) methacrylate
AM air mass	HER hydrogen evolution reaction
AP artificial photosynthesis	HIPS high-impact polystyrene
BCP bathocuproine	HOMO high occupied molecular orbital
BDD boron-doped diamond	HTE high-temperature electrolysis
DCM dichloromethane	I2M interaction two metal centers
DMF dimethylformamide	IC internal conversion
DMSO dimethyl sulfoxide	IOH indium oxide
DSSC dye-sensitized solar cell	ISC intersystem crossing
CCD charge-coupled device	ITO indium-tin oxide
CCE controlled current electrolysis	LA liquid alkaline
CCM catalyst-coated membrane	LED light-emitting diodes
CCS catalyst-coated substrate	LMCT ligand-to-metal charge transfer
CIGS copper indium gallium selenide	LTE low-temperature electrolysis
CNT carbon nanotube	LUMO low occupied molecular orbital
COF covalent organic framework	MALDI matrix-assisted laser desorption/ionization
CPE controlled potential electrolysis	MBM poly(methylmethacrylate)- <i>b</i> - poly(1,4-butadiene)- <i>b</i> - poly(methylmethacrylate)
CV cyclic voltammetry	MEA membrane electrode assembly
DFT density functional theory	MLCT metal-to-ligand charge transfer
DPV differential pulse voltammetry	MMA methyl methacrylate
EC electrochemical cell	MOF metal organic framework
ECSA electrochemical active surface area	MS mass spectrometry
EPR electron paramagnetic resonance	MW molecular weight
ET electron transfer	NHE normal hydrogen electrode
FF fill-factor	
FOWA foot of the wave analysis	
FTO fluorine-doped tin oxide	
GC glassy carbon	

NMP nitroxide-mediated polymerization	S _n electronic singlet state
NMR nuclear magnetic resonance	SEC size exclusion chromatography
OD optical density	SET single electron transfer
OER oxygen evolution reaction	SET-WNA single electron transfer water nucleophilic attack
OTTLE optical transparent thin layer electrochemical	SS steady state
SEM scanning electron microscopy	SV Stern-Volmer
PBS phosphate buffer solution	STH solar-to-hydrogen
PCE power conversion efficiency	T _n electronic triplet state
PCET proton-coupled electron transfer	TA transient absorption
PEC photo-electrochemical	TAML tetra-amidate macrocyclic ligand
PEM proton exchange membrane	TBAPF ₆ tetrabutylammonium hexafluorophosphate
PE printed electrode	TCSPC time-correlated single photon counting
PGM platinum group metal	TFE 2,2,2 trifluoro ethanol
PGMEA propylene glycol methyl ether acetate	THF tetrahydrofuran
PL photoluminescence	TOF turnover frequency
PMT photomultiplier	TON turnover number
PP pump-probe	TR time-resolved
ppb part per billion	UV-vis ultraviolet-visible
PS polystyrene	WNA water nucleophilic attack
PV photovoltaic	WOC water oxidation catalyst
PV-EC photovoltaic-electrochemical	WS water splitting
RBS Rutherford backscattering	XAS X-ray absorption spectroscopy
RDS rate-determining step	XPS X-ray photoelectron spectroscopy
RI refractive index	

I

INTRODUCTION

1.1 ENERGY TRANSITION

One of the biggest challenges our society faces in the 21st century is the energy revolution, the transition from fossil fuel-based energy sources to more renewable ones. How we sustain our energy demand is the crucial aspect that will determine humankind's development in the next future. As the world population keeps growing, so will our energy needs. It has been forecast that by 2050 about ten billion people will live on Earth ^[1], most of which will be in developing countries. Ideally, we should aim to reduce energy consumption, but this is incompatible with our present economic system ^[2], in which we are increasingly pushed to produce and consume. Furthermore, the disparity is a worldwide spread phenomenon, with poorly distributed or traded resources, whereas we should provide energy equitably among individuals ^[3].

More than a century ago, Arrhenius identified CO₂ as a greenhouse gas (GHG), highlighting the relation between its atmospheric concentration and its potential to affect global climates ^[4]. In the following years, his observation, the idea that CO₂ from the combustion of hydrocarbons negatively impacts the climate, became widely accepted. When the CO₂ concentration increases rapidly, the geosphere's carbon cycle is oversaturated, and excess CO₂ cannot be recycled. It persists in the atmosphere and traps heat from solar radiation. To make things even more complicated, the very reason for our industrial and technological boom during the last few centuries is one contributing factor to our doom; the heavy exploitation of fossil fuels.

Worldwide GHG emissions are a complex number to estimate and are often subject to controversy. However, we can agree that the more prominent contributor is the energy sector (energy used in industry, buildings, and transports), followed by the agriculture and food sector (livestock, land usage, deforestation, sea exploitation), which make up about 95% of the total GHG releases ^[5–9].

Therefore, our energy system is facing a double challenge: enhancing its capacity while reducing the emission of pollutants to compensate for the effects of global warming. One strategy is to produce fuels based on renewable sources. Can we supply the whole global population with basic/decent living standards without further burdening our planet's ecosystem and threatening our survival? We should aim to develop energy systems with zero net carbon footprint and provide it accessibly and affordably. Doing so would tackle several other problems, for energy is one, if not the most important priority humankind has. Think of poverty, food and water scarcity, health, education, and conflicts, all complications that would be settled if there was an adequate and reliable energy supply around the globe.

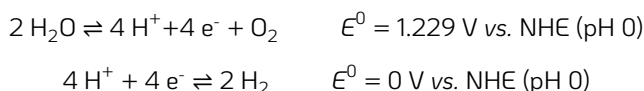
1.2 SOLAR FUELS AND WATER SPLITTING

Renewable energy is defined as energy derived from natural sources that are replenished at a higher rate than they are consumed ^[10]. Solar, wind, hydro, tidal, and geothermal energies fall within the description. Biomass, typically considered as renewable, is not strictly sustainable, as it requires extensive cultivable land, water, and time for the vegetation to be grown. Additionally, in producing energy, biomass releases CO₂ into the atmosphere providing a net-zero GHG contribution provided the emitted CO₂ is captured and converted later by natural photosynthesis.

In 2021, about 18.9 TW of power was consumed worldwide ^[2], while the Sun provides us with about 170000 TW in the form of radiation, colliding with our atmosphere incessantly. Based on the forecasts mentioned above, given that providing ten billion people with a decent living standard (5 - 10 kW), we would need to harness 50 - 100 TW to satisfy our energy hunger. Ideally, that amount of power (~ 60 TW) could be obtained by using 0.32% of Earth's surface land as "solar farms", with a solar energy conversion efficiency of 10 % ^[11].

Notably, solar energy is seemingly interminable for our purposes but is also intermittent in terms of day/night cycles, weather, and seasonal dependency. Furthermore, there is a mismatch between its supply peak (noon) and our demand, occurring for most civilian uses in the morning and later in the evening. Hence, taking inspiration from nature, we must store solar energy into chemical energy to use and transport it if we desire to exploit solar radiation. Solar energy has much potential to offer, with possibilities ranging from electrical energy, thermal energy, and solar fuels. These technologies require improvements in terms of efficiency, scalability, and commercialization cost to compete in the market with current primary fossil-based energy sources ^[12].

While the idea of storing solar energy through photochemical reactions was proposed as early as 1912 by the Italian scientist Ciamician^[13], it is only in recent years that there is an increasing interest in driving catalytic chemical fuel production using sunlight. *Artificial photosynthesis* (AP), introduced by Fujishima and Honda^[14], is one example of the direct conversion of sunlight into storable chemicals such as hydrogen by a *water splitting* (WS) reaction. This transformation is composed of the oxidation of water into molecular oxygen and protons (oxygen evolution reaction, OER), and the latter species are reduced into molecular hydrogen (hydrogen evolution reaction, HER):



Hydrogen is, therefore, a secondary energy source, as we need to spend some to produce it in the first place. At the same time, it displays a chemical energy density of 120 MJ kg⁻¹, outstanding compared to gasoline (46 MJ kg⁻¹), natural gas (54 MJ kg⁻¹), or other oil derivatives. It also benefits from producing zero carbon emissions and affording only water upon combustion.

We have discussed above that for sustainable production, solar radiation can be easily employed because of its large abundance. Water is the other primary resource for water splitting or other solar fuel technologies. If we aspire to replace most of our energy carriers with clean hydrogen, water better be abundant if we do not want to see wars over something far more indispensable than oil. Now, the question is: do we have enough water on our planet to be used in these applications? Estimating the hydrogen demand in the far future, we predict that we will need 2.3 Gt of H₂ per year, equivalent to 20.5 Gt of water, which is the equivalent of 1.5 ppm of Earth's freshwater or 30 ppb of salt water^[15]. With recent advancements in desalination processes, such as reverse osmosis, the use of salt water in electrolyzers might become a reality since their costs are negligible compared to water splitting^[16,17], other than being a realistic solution for water scarcity. Overall, the water possibly required for a clean hydrogen economy will be about 33% less than the current amount employed in fossil fuels production processes (e.g., mining, cooling, etc.)^[18]. Those numbers are small considering that 70% of global water usage is consumed for agricultural purposes^[15,19], around 25% of which is in the meat and dairy sector^[20].

We highlighted the extraordinarily high gravimetric energy density of hydrogen, having the highest value of all known substances that afford chemical energy. The drawback lies in its volumetric energy density being extremely low at atmospheric pressure (0.01 MJ L⁻¹), making it difficult for practical uses or transport in these conditions. Hydrogen compression or liquefaction is not a long-lasting solution since it requires extreme pressures and temperatures, easily translated into energy-

demanding processes. Solid-state hydrogen storage might be the turn, especially using metal hydrides, which can achieve volumetric densities higher than the liquid hydrogen itself and enable adsorption and desorption of the gas, operated at nearly room temperature ^[21].

Water-splitting is a highly endergonic reaction ^[22], with a free Gibbs energy of $\Delta G^0 = 237 \text{ kJ mol}^{-1}$, corresponding to 1.23 eV of energy for each of the two electrons needed to split one molecule of water. To drive the electrochemical reaction at an appreciable rate, activation barriers need to be overcome such that the electrical potential needed is higher than the thermodynamic potential of $E^0 = 1.23 \text{ V}$. To keep the potential low, catalysts are indispensable to drive this reaction at an appreciable rate for practical applications. This thesis focuses on the study of molecular catalysts to be integrated into AP devices, specifically on water oxidation catalysts (WOCs).

1.3 eSCALED PROJECT AND THESIS AIM

eSCALED is a European Joint Doctorate program with the scientific aim of advancing AP systems' technology level to produce solar fuels such as hydrogen from water splitting, and other carbon-based feedstock from CO₂ reduction. With its multidisciplinary approach, the project brings together fourteen early-stage researchers within twelve institutions across Europe. Each is responsible for developing different modules of an AP device (photovoltaic cells, membranes, electrodes, and catalyst materials for OER and HER) or designing a scalable device prototype, testing the performance when the distinctive components are combined.

Within eSCALED, the present thesis explores the use of earth-abundant molecular complexes for water oxidation catalysis and their integration in water-splitting devices through developing heterogenized molecular catalysts. Bearing that in mind, a derivative of a copper-based WOC suitable for future immobilization onto a solid-state material was synthesized and characterized (chapter 3). This chapter is followed by a study on identifying possible short-lived intermediates and gain insight into mechanistic details spectroscopically, inducing the oxidation of the catalyst photochemically (chapter 4). Pursuing the development of solid-state anodes, screen-printing techniques were used to fabricate carbon-based electrodes, which were covalently functionalized with the molecular catalyst (chapter 5). Finally, a molecular-based catalyst was integrated into a flow cell electrolyzer and coupled with a solar cell to drive the WS reaction (chapter 6). Each study was realized in a different institution within the program, specifically chapter 3 was conducted at the Institut Català d'Investigació Química (ICIQ), Tarragona, Spain; chapter 4 at Uppsala University,

Sweden; chapter 5 at the Institut des Sciences Analytiques et de Physico-Chimie pour l'Environnement et les Matériaux (IPREM), Pau, France; and chapter 6 at Technische Universiteit Eindhoven, the Netherlands.

1.4 WATER OXIDATION

The oxidation of water is ideal for solar fuel transformations, as it provides protons and electrons that are needed for hydrogen production or other carbon-based feedstock (carbon monoxide, formaldehyde, methanol, *etc.*) in case CO₂ is used as substrate. Other than being thermodynamically up-hill ($E^0(\text{O}_2 / \text{H}_2\text{O}) = 1.23 \text{ V} - 0.059 \text{ V} \times \text{pH}$) versus the normal hydrogen electrode (NHE), the OER requires two molecules of water, the transfer of four electrons and four protons and a concerted O-O bond formation. These particular characteristics usually result in the necessity of high overpotentials (η) to overcome the kinetic barrier, making the formation of O₂ the bottleneck in developing water-spitting systems^[22]. To understand the reason behind the choice of molecular catalysts, an introduction will be given to their advantages, reaction mechanisms to oxidize water, drawbacks, and necessary steps for future scalable applications.

1.4.1 Molecular catalysts

Molecular catalysts based on transition metal complexes are a promising class of materials to introduce into artificial photosynthetic systems. The tunability of their ligand and coordination environment allows the design of improved materials, reducing the overpotential at which they operate together with the enhancement of the intrinsic activity and, possibly, their stability^[23,24]. Furthermore, having a single active center for each molecular species is also beneficial for metal-atom utilization, an essential factor in case rare metals are being used^[25]. Since water oxidation requires four oxidation steps, the rule of thumb for WOC is to use σ -donating ligand systems, reducing the energy required to access highly oxidative states. Proton-coupled electron transfers (PCET) also play an important role, allowing the generation of neutral intermediates, which otherwise would generate high-energy species due to the building up of coulombic charges.

Transition metals also represent a well-defined active center, enabling the investigation of reaction mechanisms by electrochemical and spectroscopical techniques, which, combined with O-labelling experiments, can lead to new insights and informed optimizations. Two classes of reaction mechanisms have been identified

depending on the conceptual O-O bond formation step, which frequently has been identified as the rate-determining step (RDS) of the catalytic cycle^[26–30]: Water nucleophilic attack (WNA) and interaction of two metal-oxyl radicals (I2M). Both mechanisms require the WOC to be oxidatively activated, which usually takes place through a series of electron transfers and a water molecule binding, yielding a metal-oxo species (Figure 1.1). WNA occurs when a nucleophilic water molecule interacts with the electrophilic metal-oxo group forming a σ O-O bond yielding the corresponding hydroperoxide species. The latter would undergo a concerted two-electron transfer to afford molecular oxygen, restoring the initial catalyst and closing the catalytic cycle. Alternatively, the hydroperoxide formation can follow two consecutive single electron transfers (SET-WNA), generating a two centers-three electrons intermediate, described for a family of copper complexes^[24,31,32]. Catalysts belonging to this category will show a positive H/D kinetic isotope effect in the O-O formation step, as the incoming water molecule loses a proton to a hydrogen-bound Lewis base (water molecule)^[28,33].

I2M occurs when two metal centers display a significant radical oxyl character and are placed nearby, and the ligand system provides an electronic coupling across them. The reaction yields an M-O-O-M peroxide bridge between the two metals, which is reduced by two consecutive one-electron transfers. The RDS is proposed to be the transformation of the peroxo bridge species to the corresponding terminal hydroperoxy specie M-OOH^[28,34–36]. This mechanism can occur intramolecularly in dinuclear complexes or intermolecularly in a mononuclear or *trans* dinuclear catalyst (Figure 1.1).

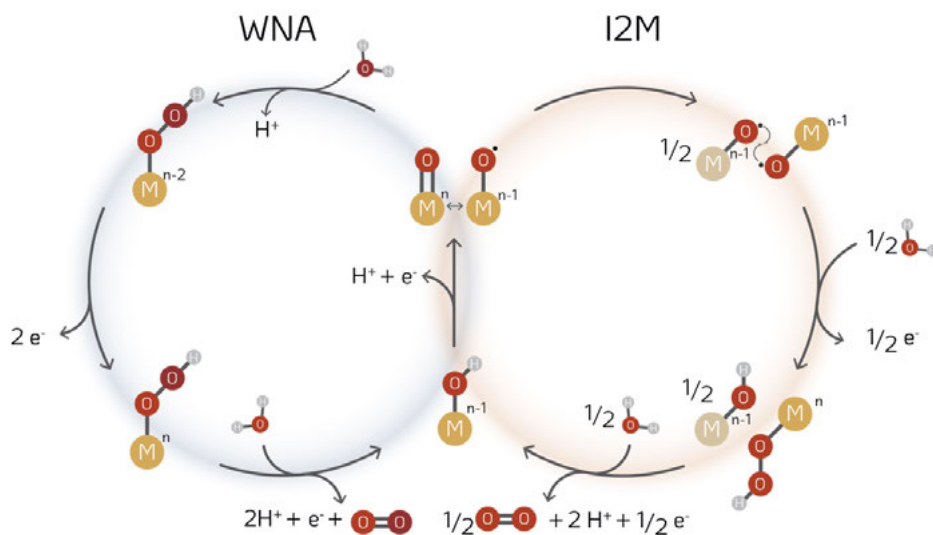


Figure 1.1. Schematic of WNA and I2M reaction mechanisms.

The main challenges imposed by the use of earth-abundant first-row transition metals are predominantly related to their electronic properties^[37,38]. Contrary to their second- or third-row counterparts, their valence *d* orbitals are less extended, which usually results in a poor overlap with the σ orbitals of ligand systems. This difference causes more remarkable lability for such coordination bonds, which can facilitate deactivation and decomposition pathways, compromising the stability of the catalyst. It is particularly true in aqueous media where ligand protonation can hinder the coordination to the metallic center, or the oxidative environment can transform the molecular species into oxides, generally in form of films or nanoparticle materials. In such cases, these can be the real active form, while the initial complex only acts as a pre-catalyst. Another factor influencing the catalyst performance is the need to accommodate several oxidation states. Because first-row transition metals possess fewer electrons than the corresponding second- and third-row elements, their ionic radii are susceptible to more considerable changes induced by a change in redox state. This factor reflects in a higher reorganization energy upon an electron transfer, which translates to kinetic constraints and increases the energetic barriers of the reactions.

Rational ligand design assisted earth-abundant WOC development over the last years to overcome the above-described limitations^[39]. Common strategies that have been adopted so far rely on strong σ -donating groups to stabilize high valence intermediates, which are necessarily formed upon fourfold oxidation of the catalyst to oxidize water. Another approach consists of using multi-dentate ligands to disfavor ligand detachment pathways^[40]. One of the benefits of molecular catalysts is that their mechanisms can be studied relatively easily by a range of spectroscopic, kinetic, and computational techniques. Within this context, the elementary steps of a catalytic cycle can be characterized, and kinetic bottlenecks and decomposition pathways can be identified. Once this information is known, a thoughtful synthetic modification of the ligand system through electronic and/or steric design can improve the intrinsic activity of the catalyst.

1.4.2 Heterogenization of molecular catalysts

The immobilization of molecular catalysts onto supports or solid-state electrodes is urgently researched as these compounds' main disadvantages are related to stability issues and solvent incompatibility. AP devices must have the catalytic centers supported onto the electrodes for future and scalable applications. Heterogeneous catalyst materials seem to serve the cause well, but those are usually based on noble metals such as Ru, Ir, or Pt, the prices of which are constantly increasing. The

advantages of such materials are their stability, recycling ease, and separation from the substrate when, for example, maintenance is needed ^[41].

On the other side, molecular catalysts have various characteristics that make them appealing. They operate at low temperatures and usually have high selectivity for specific products. Moreover, they allow tunability and modifications due to their well-defined structures, and their catalytic mechanisms are well-known or can be investigated. Since molecular catalysts are so versatile, a big challenge nowadays is to "heterogenize" these molecules onto a surface to combine the advantages of homogeneous molecular with heterogeneous catalysts ^[25,42]. Although we have not reached a level advanced enough for them to be employed in commercial devices, progress has been made in recent years showing different approaches that could be successful with adequate improvements.

Catalysts have been anchored on conducting or semiconductor metal oxide surfaces such as TiO₂, SiO₂, Fe₂O₃, fluorine-doped tin oxide (FTO), and indium tin oxide (ITO) ^[41,43,44]. Carboxylic acid ^[45] derivatives are an anchoring option for these materials, but unfortunately, they operate well only in organic media. Phosphate ^[45,46] or silicate functionalities show better hydrolytic stability. This approach is preferred in the development of photo-electrochemical (PEC) devices, in which the light-absorbing material and the catalytic centers are combined. This results in a valuable approach for photo-electrodes, where the charges are separated and injected directly into the catalyst. Alternatives for this grafting on metals or semiconducting surfaces are through ^[47] covalent bonds, such as diazonium reduction ^[48,49]. This interaction is strong and persistent and can be done in situ via electrochemical reduction. The non-covalent surface binding uses strong van der Waals interactions between graphitic-carbon surfaces and polyaromatic functionalities. Being a straightforward and convenient method yielding in stable grafted electrocatalysts, this strategy has seen many applications in recent years, primarily employing the pyrene moiety as surface binder ^[47,50–52].

1.5 SOLAR DRIVEN ELECTROLYSIS

Several technologies are employed in electrolytic hydrogen production, the most researched are high-temperature electrolysis (HTE) ^[53–55], low-temperature electrolysis (LTE), and PEC water splitting ^[56].

LTes are probably the most mature methods, and they directly produce hydrogen from sole electricity with operational temperatures below 100 °C. Different technology systems are recognized: liquid alkaline (LA), proton-exchange membrane (PEM), and

anion-exchange membrane (AEM) electrolyzers. LAs are historically the first electrolyzers employed, and they consist of a cathode and an anode separated by a diaphragm and immersed in an alkaline electrolyte, usually potassium hydroxide ^[57]. The basic pH conditions enable the use of platinum-group metal-free catalysts (Ni, Fe, Co) ^[37,58], which improves their durability. The large electrode distance in these systems contributes to avoiding hydrogen crossover to the anodic compartment, which would create an explosive mixture with the oxygen (4% mol H₂) ^[59], but it causes ohmic losses, resulting in the reduction of energy efficiency. When the electrode configuration is changed, and the anode and cathode are drawn closer to the membrane, we reach a zero-gap electrolyzer. In this case, the membrane is a solid electrolyte, and depending on its pH, we can have proton conductivity (using a PEM) or anion conductivity (using an AEM). The membrane's thickness is crucial for balancing the ohmic losses with hydrogen crossover ^[60,61]. PEM and AEM electrolyzers can be powered by photovoltaics to finalize the AP device, fully decoupling the light harvesting and the water splitting.

Finally, and contrary to the previous case, PEC electrolyzers combine solar absorption, voltage generation, and catalytic electrodes in a single system. Semiconductors are used to absorb light and generate charge carriers that are consumed by the catalysts to drive the electrochemical reactions. The two components need to be in close contact so that the charges are extracted before they can recombine.

1.5.1 PV-EC vs. PEC configurations

Conceptually, the difference between PV-EC and PEC systems stands in the spatial arrangement of the photo-absorber material ^[62,63]. While in a PEC, the semiconductor and the catalysts are present in the same medium, in a PV-EC, the photovoltaic part is spatially decoupled from the electrochemical cell (Figure 1.2).

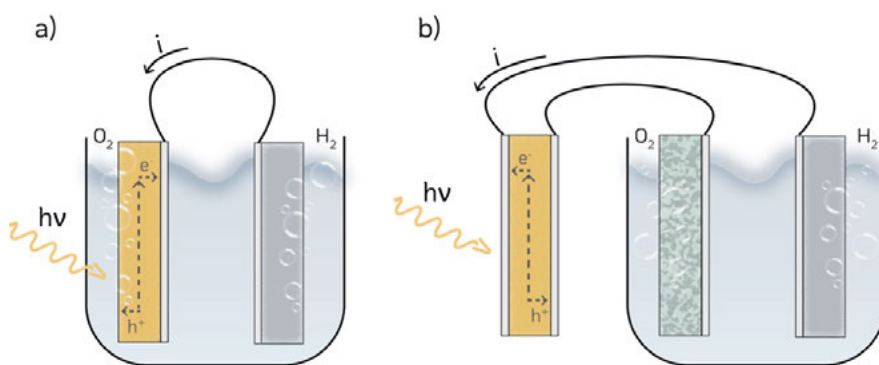


Figure 1.2. Schematic illustrations of a) PEC and b) PV-EC electrolyzers.

In a PEC configuration, the semiconductor/electrolyte interface significantly impacts the stability, as it is prone to undergo undesired transformations. These processes are driven by the harsh conditions that the semiconductor is exposed to, local pH gradients, the presence of possible radicals following chemical reactions, and the oxidative/reductive environment that surrounds the active centers. A solution to this problem is the addition of a further layer acting as a protection against decomposition. Depending on the geometry of the cell, this protection layer may need to be transparent while matching the energy level of the semiconductor and catalyst to facilitate charge injection. Alternatively, inert glass or polymeric resins can be used, but the latter will hinder charge transport across the layer, and thus, the catalyst needs to be spatially decoupled from the photo-absorber, possibly by wire connections or by other approaches ^[64–66].

As Jacobson *et al.* have shown ^[67], the difference between the PEC and PV-EC is just a matter of topology design, where the charge transport between photo-absorber and catalyst sites is moved from a nanometer scale to longer scales and eventually to wire connections. However, in a monolithic configuration where the PV-EC uses a thin metal or conductive layer that acts on one side as an electrode of the PV system and other side as the support for an OER or HER catalyst, the differentiation between PV-EC and PEC becomes almost semantics. One advantage of PV-EC is that it allows a modular approach to the research, as the two parts can be studied and improved separately. Over the years, progress in the photovoltaic field has been impressive, with a substantial reduction in the production cost of modules. Efficiencies of several low-cost photovoltaic technologies such as single-junction solar cells based on crystalline silicon (26.8%), perovskite (25.7%), and organic (18.2%) semiconductors have been increasing while in tandem cell configurations using perovskite/silicon (32.5%), perovskite/perovskite (28.0%), perovskite/organic (23.4%) efficiencies are approaching or have passed the 30% threshold ^[68,69]. This greatly favors the development of PV-EC, making it possible for the technology to achieve STH efficiencies higher than 10% in many cases ^[70,71]. Furthermore, catalysts do not contribute to absorption losses in PV-EC systems. The ultimate choice for PV-EC or PEC made systems in the future will depend on the balance of a multitude of parameters involving efficiency, manufacturability, durability, recyclability, availability of materials, sustainability, and cost for production, installation, and operation.

1.6 REFERENCES

- [1] D. Adam, *Nature* **2021**, 597, 7877, 462–465.
- [2] British Petroleum, *BP Energy Outlook: 2022 Edition*, **2022**.
- [3] N. Armaroli, V. Balzani, *Angew. Chem. Int. Ed.* **2007**, 46, 52–66.
- [4] S. Arrhenius, *The London, Edinburgh, and Dublin Philosophical Magazine and Journal of Science* **1896**, 41, 251, 237–276.
- [5] H. Ritchi, M. Roser, P. Rosado, “CO₂ and Greenhouse Gas Emissions,” **2020**.
<https://ourworldindata.org/co2-and-other-greenhouse-gas-emissions>
- [6] T. R. H. Pearson, S. Brown, L. Murray, G. Sidman, *Carbon Balance Manage.* **2017**, 12, 3.
- [7] S. Kruid, M. N. Macedo, S. R. Gorelik, W. Walker, P. Moutinho, P. M. Brando, A. Castanho, A. Alencar, A. Baccini, M. T. Coe, *Front. For. Glob. Change* **2021**, 4.
- [8] P. R. Shukla, J. Skea, A. al Khouradajie, R. van Diemen, D. McCollum, M. Pathak, s. Some, P. Vyas, R. Fradera, M. Belkacemi, A. Hasija, G. Lisboa, S. Luz, *Mitigation of Climate Change Climate Change 2022 Working Group III Contribution to the Sixth Assessment Report of the Intergovernmental Panel on Climate Change*, **2022**.
- [9] M. Crippa, E. Solazzo, D. Guizzardi, F. Monforti-Ferrario, F. N. Tubiello, A. Leip, *Nat. Food* **2021**, 2, 198–209.
- [10] United Nations, “What is renewable energy?”, <https://www.un.org/en/climatechange/what-is-renewable-energy>
- [11] R. E. Smalley, *MRS Bull* **2005**, 30, 412–417.
- [12] S. N. Lewis, *Science* **2016**, 351, 6271, 353–362.
- [13] G. Ciamician, *Science* **1912**, 36, 926, 385–394.
- [14] A. Fujishima, K. Honda, *Nature* **1972**, 238, 37–38.
- [15] R. R. Beswick, A. M. Oliveira, Y. Yan, *ACS Energy Lett.* **2021**, 6, 9, 3167–3169.
- [16] M. A. Khan, T. Al-Attas, S. Roy, M. M. Rahman, N. Ghaffour, V. Thangadurai, S. Larter, J. Hu, P. M. Ajayan, M. G. Kibria, *Energy Environ. Sci.* **2021**, 14, 4831–4839.
- [17] X. Shi, X. Liao, Y. Li, *Renew. Energy* **2020**, 154, 786–796.
- [18] Y. Jin, P. Behrens, A. Tukker, L. Scherer, *Renew. Sustain. Energy Rev.* **2019**, 115, 109391.
- [19] Energy Agency - IEA, **2017- Water-Energy Nexus** <https://www.iea.org/reports/water-energy-nexus>
- [20] A. Y. Hoekstra, *Anim. Front.* **2012**, 2, 2, 3–8.
- [21] K. T. Møller, T. R. Jensen, E. Akiba, H. Li, *Prog. Nat. Sci.: Mater. Int.* **2017**, 27, 34–40.
- [22] S. Ye, C. Ding, C. Li, *Adv. Inorg. Chem.*, **2019**, 74, 3–59.
- [23] M. J. Craig, G. Coulter, E. Dolan, J. Soriano-López, E. Mates-Torres, W. Schmitt, M. García-Melchor, *Nat. Commun.* **2019**, 10, 4993.
- [24] P. Garrido-Barros, R. Matheu, C. Gimbert-Suriñach, A. Llobet, *Curr Opin. Electrochem.* **2019**, 15, 140–147.
- [25] B. Zhang, L. Sun, *Chem. Soc. Rev.* **2019**, 48, 2216–2264.
- [26] M. Okamura, M. Kondo, R. Kuga, Y. Kurashige, T. Yanai, S. Hayami, V. K. K. Praneeth, M. Yoshida, K. Yoneda, S. Kawata, S. Masaoka, *Nature* **2016**, 530, 7591, 465–468.

-
- [27] Y. Tanahashi, K. Takahashi, Y. Tsubonouchi, S. Nozawa, S. Adachi, M. Hirahara, E. A. Mohamed, Z. N. Zahran, K. Saito, T. Yui, M. Yagi, *Proc. Natl. Acad. Sci.* **2021**, *118*, 52, e2113910118.
- [28] D. W. Shaffer, Y. Xie, D. J. Szalda, J. J. Concepcion, *Inorg. Chem.* **2016**, *55*, 22, 12024–12035.
- [29] Y. Zhang, H. Zhang, A. Liu, C. Chen, W. Song, J. Zhao, *J. Am. Chem. Soc.* **2018**, *140*, 9, 3264–3269.
- [30] C. Casadevall, V. Martin-Diaconescu, W. R. Browne, S. Fernández, F. Franco, N. Cabello, J. Benet-Buchholz, B. Lassalle-Kaiser, J. Lloret-Fillol, *Nat. Chem.* **2021**, *13*, 8, 800–804.
- [31] I. Funes-Ardoiz, P. Garrido-Barros, A. Llobet, F. Maseras, *ACS Catal.* **2017**, *7*, 3, 1712–1719.
- [32] P. Garrido-Barros, I. Funes-Ardoiz, S. Drouet, J. Benet-Buchholz, F. Maseras, A. Llobet, *J. Am. Chem. Soc.* **2015**, *137*, 21, 6758–6761.
- [33] T. J. Meyer, M. v. Sheridan, B. D. Sherman, *Chem. Soc. Rev.* **2017**, *46*, 6148–6169.
- [34] X. Sala, S. Maji, R. Bofill, J. García-Antón, L. Escriche, A. Llobet, *Acc. Chem. Res.* **2014**, *47*, 2, 504–516.
- [35] P. Garrido-Barros, C. Gimbert-Suriñach, R. Matheu, X. Sala, A. Llobet, *Chem. Soc. Rev.* **2017**, *46*, 6088–6098.
- [36] X. P. Zhang, H. Y. Wang, H. Zheng, W. Zhang, R. Cao, *Chinese J. Cat.* **2021**, *42*, 1253–1268.
- [37] A. Singh, L. Spiccia, *Coord. Chem. Rev.* **2013**, *257*, 17–18, 2607–2622.
- [38] L. H. Zhang, S. Mathew, J. Hessels, J. N. H. Reek, F. Yu, *ChemSusChem* **2020**, *14*, 1, 234–250.
- [39] M. Kondo, H. Tatewaki, S. Masaoka, *Chem. Soc. Rev.* **2021**, *50*, 6790–6831.
- [40] A. Prevedello, I. Bazzan, N. Dalle Carbonare, A. Giuliani, S. Bhardwaj, C. Africh, C. Cepek, R. Argazzi, M. Bonchio, S. Caramori, M. Robert, A. Sartorel, *Chem. Asian J.* **2016**, *11*, 8, 1281–1287.
- [41] W. Li, D. He, S. W. Sheehan, Y. He, J. E. Thorne, X. Yao, G. W. Brudvig, D. Wang, *Energy Environ. Sci.* **2016**, *9*, 1794–1802.
- [42] S. Berardi, S. Drouet, L. Francàs, C. Gimbert-Suriñach, M. Guttentag, C. Richmond, T. Stoll, A. Llobet, *Chem. Soc. Rev.* **2014**, *43*, 7501–7519.
- [43] A. M. Oertel, V. Ritleng, M. J. Chetcuti, *Organometallics* **2012**, *31*, 7, 2829–2840.
- [44] S. W. Sheehan, J. M. Thomsen, U. Hintermair, R. H. Crabtree, G. W. Brudvig, C. A. Schmuttenmaer, *Nat Commun* **2015**, *6*, 6469.
- [45] M. Wang, Y. Yang, J. Shen, J. Jiang, L. Sun, *Sustain. Energy Fuels* **2017**, *1*, 1641–1663.
- [46] M. Schreier, J. Luo, P. Gao, T. Moehl, M. T. Mayer, M. Grätzel, *J. Am. Chem. Soc.* **2016**, *138*, 6, 1938–1946.
- [47] P. Kang, S. Zhang, T. J. Meyer, M. Brookhart, *Angew. Chem. Intern. Ed.* **2014**, *53*, 33, 8709–8713.
- [48] P. Allongue, M. Delamar, B. Desbat, O. Fagebaume, R. Hitmi, J. Pinson, J. M. Savéant, *J. Am. Chem. Soc.* **1997**, *119*, 1, 201–207.
- [49] J. Pinson, F. Podvorica, *Chem. Soc. Rev.* **2005**, *34*, 429–439.
- [50] P. Garrido-Barros, C. Gimbert-Surinifach, D. Moonshiram, A. Picón, P. Monge, V. S. Batista, A. Llobet, *J. Am. Chem. Soc.* **2017**, *139*, 37, 12907–12910.

-
- [51] H. Lei, C. Liu, Z. Wang, Z. Zhang, M. Zhang, X. Chang, W. Zhang, R. Cao, *ACS Catal.* **2016**, 6, 10, 6429–6437.
- [52] P. D. Tran, A. le Goff, J. Heidkamp, B. Jusselme, N. Guillet, S. Palacin, H. Dau, M. Fontecave, V. Artero, *Angew. Chem. Intern. Ed.* **2011**, 50, 1371–1374.
- [53] V. Subotić, T. Napporn, *Metal Oxide-Based Nanostructured Electrocatalyst for Fuel Cells, Electrolyzers, and Meta-Air Batteries*, Elsevier BV, **2021**, 213–234.
- [54] K. Du, E. Gao, C. Zhang, y. Ma, P. Wang, R. Yu, W. Li, K. Zheng, X. Cheng, D. Tang, B. Deng, H. Tin, D. Wang, *Nat. Commun.* **2023**, 1, 14.
- [55] M. Lin, C. Suter, S. Diethelm, J. Van herl, S. Haussener, *Joule*, 2022, 6, 9, 2102–2121.
- [56] K. Sivula, R. van de Krol, *Nat. Rev. Mat.* **2016** 1, 2, 15010.
- [57] W. Hug, J. Divisek, J. Mergel, W. Seeger, H. Steen, *Int. J. Hydrog. Energy* **1992**, 17, 9, 699–705.
- [58] E. López-Fernández, C. Sacedón, J. Gil-Rostra, F. Yubero, A. González-Elipe, A. de Lucas-Consuegra, *Molecules* **2021**, 26, 21, 6326.
- [59] M. A. Butler, *J. Electrochem. Soc.* **1991** 138, 9, L46
- [60] K. Baik, B. Hong, M. Kim, *Renew. Energ.* **2013**, 57, 234–239.
- [61] P. Trinke, P. Haug, J. Brauns, B. Bensmann, R. Hanke-Rauschenbach, T. Turek, *J. Electrochem. Soc.* **2018**, 165, 7, F502–F513.
- [62] J. H. Kim, D. Hansora, P. Sharma, J. W. Jang, J. S. Lee, *Chem. Soc. Rev.* **2019**, 48, 1908–1971.
- [63] Z. Wang, Y. Gu, L. Wang, *Front. Energy* **2021**, 15, 596–599.
- [64] S. Tembhurne, F. Nandjou, S. Haussener, *Nat. Energy* **2019**, 4, 399–407.
- [65] H.C. Fu, P. Varadhan, C.H. Lin, J.H. He, *Nat. Commun.* **2020**, 11, 3930.
- [66] I. Poli, U. Hintermair, M. Regue, S. Kumar, E. v. Sackville, J. Baker, T. M. Watson, S. Eslava, P. J. Cameron, *Nat. Commun.* **2019**, 10, 2097.
- [67] T. J. Jacobsson, V. Fjällström, M. Edoff, T. Edvinsson, *Energy Environ. Sci.* **2014**, 7, 2056–2070.
- [68] M. A. Green, E. D. Dunlop, J. Hohl-Ebinger, M. Yoshita, N. Kopidakis, K. Bothe, D. Hinken, M. Rauer, X. Hao, *Prog. Photovolt.: Res. Appl.* **2022**, 30, 7, 687–701.
- [69] The National Renewable Energy Laboratory, “Best Research-Cell Efficiency Chart,” <https://www.nrel.gov/pv/cell-efficiency.html>
- [70] Y. Shi, T. Y. Hsieh, M. A. Hoque, W. Cambarau, S. Narbey, C. Gimbert-Surinăch, E. Palomares, M. Lanza, A. Llobet, *ACS Appl. Mater. Interfaces* **2020**, 12, 50, 55856–55864.
- [71] S. Esiner, J. Wang, R. A. J. Janssen, *Cell. Rep. Phys. Sci.* **2020**, 1, 5, 100058.

2

THEORY AND TECHNIQUES

2.1 VOLTAMMETRY

2.1.1 Electrochemistry introduction

Electron transfer is one of the most fundamental processes responsible for change in matter and occurs everywhere around us. Energy conversion in biological systems such as cellular respiration in animals and photosynthesis in plants, decomposition of organic material, combustion and corrosion are only a few examples. Electron transfer reactions, also known as redox reactions, involve the exchange of one or more electrons between two substances, where the species donating the electron is oxidized and the one accepting the electron is reduced. Redox reactions can also be performed electrochemically when electrodes are used to receive (anode) or provide (cathode) electrons. In electrochemical reactions, the redox species can spatially be separated but must be enclosed in a combined electrical–ionic circuit to maintain a conductive pathway of charges. When a potential difference exists between the electrodes where redox reactions occur, an electric current can be generated to perform work in an external circuit. Alternatively, applying a potential, chemical transformations can be accomplished that store electrical energy in charged species or chemical bonds. Hence, electrochemical processes can be used in exergonic reactions between reactants producing energy and driving endergonic reactions by supplying electric work. Electrochemistry is a physical-chemistry discipline that deals with chemical transformation at the interface of polarized interfaces in a vast number of technologies and phenomena.

Electrochemical reactions most commonly occur at the interface of a solid electrode and a liquid electrolyte containing the species that are reduced or oxidized. The processes at the electrode/electrolyte interface are controlled by kinetic and thermodynamic parameters ^[1]. Considering a reaction,



where O and R are the oxidized and reduced species, respectively, and the number n of electrons, e^- , are provided by a conducting substrate. The overall electrochemical processes can be considered as a combination of three processes: (1) the diffusion of molecular species O and R to and from the electrode, respectively; (b) the kinetics of the heterogeneous electron transfer across the electrode-solution interface; and (3) the thermodynamic equilibrium of the oxidized and reduced species. In the following, a brief introduction will be given to the laws that govern these processes. A complete description can be found in the literature ^[1–3].

Before electron transfer between an electrode surface and the species in solution takes place, the latter needs to diffuse from the bulk of the solution to the interface. Net diffusion occurs when there is a gradient in the concentration of a species within a medium. We can define the molar flux j_{mol} (in $\text{mol m}^{-2} \text{s}^{-1}$) of a species to the electrode surface by Fick's first law:

$$j_{\text{mol}} = -D \frac{\partial C}{\partial x}$$

where D is the diffusion constant (in $\text{m}^2 \text{s}^{-1}$) and C is the concentration (in mol m^{-3}), and x is the spatial coordinate (in m). The negative sign shows the net flow towards the less concentrated region. To represent how the concentration changes over time t (in s) in a linear space increment, we can use Fick's second law:

$$\frac{\partial C(x,t)}{\partial t} = -\frac{\partial j_{\text{mol}}}{\partial x} = D \frac{\partial^2 C}{\partial x^2}$$

At the electrode surface, the redox reaction occurs. The rates for the forward reaction k_f and the backward reaction k_b depend on the applied potential E (in V) relative to the standard potential E^0 (in V) and are given by:

$$k_f = k_0 \exp\left(-\frac{\alpha n F \eta}{RT}\right)$$

$$k_b = k_0 \exp\left(\frac{(1 - \alpha) n F \eta}{RT}\right)$$

Where $\eta = E - E^0$, R is the universal gas constant (in $\text{J mol}^{-1} \text{K}^{-1}$), T is the absolute temperature (in K), n is the number of electrons transferred, F is the Faraday constant (in C mol^{-1}), α the dimensionless transfer coefficient ($0 \leq \alpha \leq 1$), and k_0 the standard heterogeneous rate constant (in m s^{-1}). The net current density j (in A m^{-2}) at the electrode is the sum of the current densities in the forward (cathodic current) and backward directions (anodic current) and can be expressed as:

$$j = j^0 - j^R = nF(k_f[\text{O}] - k_b[\text{R}])$$

The current passing through the electrode (i), with electrode surface area A (in m^2), is then given by:

$$i = nFk_0A \left([O] \exp\left(-\frac{\alpha nF\eta}{RT}\right) - [R] \exp\left(\frac{(1-\alpha)nF\eta}{RT}\right) \right)$$

The equation, known as the Butler–Volmer equation, is the fundamental relationship between current and applied potential. The measured current at the electrode is thus a function of the applied potential and the chemical species concentration. In particular, their equilibrium results from the chemical and electrical energies and is governed by the potential applied at the electrode surface. The dynamic equilibrium ($i = 0$) is described by Nernst equation:

$$E = E^0 - \frac{RT}{nF} \ln \frac{[R]}{[O]}$$

The equilibrium is achieved when the chemical contribution of the free energy gradient is equal to the electrical contribution.

2.1.2 Cyclic voltammetry

Cyclic voltammetry (CV) is a linear sweep technique in which the potential measured between the working electrode and a reference electrode is cycled linearly over time between two pre-set values. This produces a triangular input waveform, and its slope is called the scan rate v (in V s^{-1}). The experiment uses a three-electrode setup, consisting of a reference, a working, and a counter electrode, controlled by a potentiostat that applies a potential between the working electrode and the counter electrode and simultaneously measures the magnitude of current generated. The reference electrode experiences a negligible current during the experiment and measures the potential to enable a controlled and coherent variation of the potential at the working electrode. Figure 2.1 shows the cyclic voltammograms of chemical and electrochemical reversible redox reactions.

It is essential at this point to distinguish the concept of chemical (C) and electrochemical (EC) reversibility of a process, which both have different impacts on the voltammogram (Figure 2.1b). While the former assesses the chemical stability of the new molecule at the electrode, the latter measures how fast the standard electron transfer rate constant (k_0 from the Butler–Volmer equation) is compared to the mass transfer coefficient m_i (in m s^{-1}). m_i is defined as the ratio of the diffusion constant D and the thickness of the Nernst diffusion layer δ (in m) at the electrode:

2.

$$m_t = \frac{D}{\delta}$$

For electrochemical reversibility, we can differentiate between three different situations of the magnitude of k_0 compared to m_t :

$$\begin{array}{ll} k_0 > m_t & \text{EC reversible} \\ k_0 < m_t & \text{EC irreversible} \\ k_0 \approx m_t & \text{quasi-reversible} \end{array}$$

Since electrochemical methods make use of concentrated ionic solutions, which, other than increasing electric conductivity, suppress ionic migration and leave diffusion as the only reliable transport method. The thickness δ of the diffusion layer depends on the time t needed to record the voltammogram and is thus proportional to the inverse voltage scan rate ν^{-1} . Using the general relation $\delta \propto \sqrt{Dt}$, we can write $\delta \propto \sqrt{D\nu^{-1}}$, from which we infer that:

$$m_t \propto \sqrt{D\nu}$$

The relation shows that increasing the scan rate too high will result in a deviation of reversibility; hence, each voltammogram is determined and affected by the ν used. In an ideal reversible transfer, the potential difference between the anodic and cathodic peak current (ΔE_p) is maintained constant and it is given by:

$$\Delta E_p = 2.218 \frac{RT}{nF} = \frac{57}{n} \text{ mV} \quad (T = 298 \text{ K})$$

Where n is the number of electrons involved in the process.

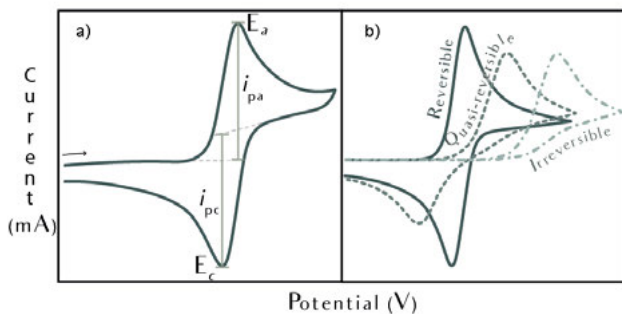


Figure 2.1. a) Voltammogram of one electron process, showing current intensities and potentials of anodic and cathodic peaks, i_{pa} , i_{pc} , E_a and E_c respectively. b) Examples of different EC and C irreversible voltammograms.

To understand the peak current in a cyclic voltammogram, we note that experimentally recorded current is determined by the molar flux j_{mol} and the electrode area via:

$$i = nFAj_{\text{mol}}$$

Moreover, applying Fick's law within the diffusion layer and ignoring the minus sign, we obtain:

$$i = nFAD \frac{\partial C}{\partial x}$$

Because the maximum possible concentration gradient is C/δ and $\delta \propto \sqrt{Dv^{-1}}$. The maximum current density scales with \sqrt{Dv} . The full analysis involves the diffusion and the Nernst equation in which the $[O]/[R]$ ratio becomes time-dependent. The solution for a reversible case can be written as:

$$i_p = 0.446 nFAC \sqrt{\frac{nFDv}{RT}}$$

This equation, known as the Randles – Ševčík relation, states that for a freely diffusion-controlled reversible redox process, the peak current i_p is proportional to the bulk concentration of the species (C) and the square root of the scan rate $v^{1/2}$.

If the electrode has a porous structure or a rough and irregular distribution, the electrochemical active surface area (ECSA) can be calculated from current signals at non-Faradaic processes. While Faradaic processes consist of all chemical transformations that include charge transfers, non-Faradaic processes generate a current due to charge accumulation at the electrode/solution interface, showing a behavior typical of capacitor components. More in-depth information on this interface, the double-layer capacitance, can be found in other sources ^[4]. The ECSA can be evaluated by the use of:

$$\text{ECSA} = \frac{C_{\text{dl}}}{C_s}$$

Where C_{dl} is the capacitance (in C V⁻¹) of the double layer and C_s (in C V⁻¹ m⁻²) is the specific capacitance considering the electrode material and the electrolyte in use. The latter describes the capacitance of an ideal flat surface of a given material. C_{dl} can then be calculated from cyclic voltammetry experiments, using the current from a non-faradaic potential window ^[5,6]:

$$C_{\text{dl}} = \frac{i}{v}$$

Species absorbed on the electrode surface, as by physisorption or covalent bonds, give rise to different behavior than species freely diffusing in solution. For an adsorbed electroactive species, the cyclic voltammogram is symmetrically shaped with, in an ideal case, no separation between the cathodic and anodic peak potentials centered at E^0 . In practice, a deviation from EC reversibility due to a slower electron transfer rate constant will separate the two current peaks. The current response is a function of the surface coverage Γ^0 (in mol m^{-2}) of electroactive species on the electrode surface A . Assuming a monolayer coverage, the peak current can be described by the equation:

$$i_p = \nu A \Gamma^0 \frac{n^2 F^2}{4RT}$$

Integration of the area under the voltammogram provides the total charge (Q) responsible for electroactive molecules within the diffusive layer that raises the electric signal.

$$Q = \frac{\int_{E_1}^{E_2} i_{\text{act}} dE - \int_{E_1}^{E_2} i_{\text{dl}} dE}{\nu}$$

The first integral term refers to the signal recorded in the presence of the electrochemically active species. The second one is the integrated area in the same interval for a sample in the absence of the electroactive species (Faradaic and non-Faradaic, thus considering the only double layer contribution. For redox-active species in solution, the total number of molecules converted equals:

$$n_{\text{mol}} = \frac{Q}{nF}$$

While for immobilized molecules, the surface coverage is:

$$\Gamma^0 = \frac{Q}{nFA}$$

Voltammetry is also a versatile tool to identify and study homogeneous chemical reactions (C) coupled with heterogeneous electron transfers (E). Rationally, we can think of different scenarios for the coupled reactions to occur, such as a step-wise electrochemical electron transfer followed by a chemical reaction (EC) or the chemical step followed by the electrochemical one (CE). Other examples are systems involving multiple electron transfers due to radical formation in small organic molecules or ligand exchange in coordination complexes, resulting in reaction schemes like ECE or ECEC. Savéant extensively studied these mechanisms and introduced the kinetic zone diagrams. Those maps represent cyclic voltammetric responses as a function of equilibrium rate constant and a kinetic parameter, λ , which measures the competition between a chemical reaction and analyte diffusion ^[2]. For a given system, it is thus

possible to identify the different reaction mechanisms through a scan rate dependence, reflecting the molecular species' diffusion rate.

Most importantly, for our purposes, Savéant described the multi-electron process as catalysis for a one-electron one-substrate electrocatalytic reaction (EC') in voltammetry analysis. In this case, a molecular catalyst acts as an electron shuttle between the electrode surface and the substrate regenerating its original form at every reaction ^[7,8]. The current response in a catalytic process is vastly enhanced and loses its dependency on the scan rate. In this case, the zone diagram representing the CV waveform is a function of the dimensionless kinetic parameter $\lambda = [RT/F][k_e C/\nu]$ and an excess factor, $\gamma = C_S/C_A$. k_e is the rate constant of the homogeneous electron transfer, ν is the scan rate, C_S and C_A are the bulk concentration of substrate and catalyst respectively ^[8,9].

We use voltammetry to evaluate the catalytic reactions of active materials, as they give rise to precise voltammetric responses, but other electrochemical methods can contribute to obtain additional helpful information. The Faradaic efficiency (η_F) is one fundamental parameter related to electrocatalysis. It defines the ratio of electrons utilized in the evolution of a particular product to the total current liberated, usually in an electrolysis experiment. It is then a measure of the selectivity of the investigated system if multiple products are expected (e.g., CO₂ reduction reaction) or an indication that the catalyst is undergoing unwanted or unexpected side reactions.

$$\eta_F = \frac{n_P}{Q/nF}$$

Where n_P are the moles of product, Q is the charge passed throughout the experiment, and n is the number of electrons involved in the catalytic reaction. To express the intrinsic activity and the robustness of a material, we can use the turnover number (TON), which is a dimensionless number defining the amount of generated product per catalytic center under specific conditions until the decay of the activity ^[10]. However, if the simple catalyst bulk concentration is taken in the catalyst moles determination, it will result in an underestimation of the TON if we deal with homogeneous catalysis. To circumvent this issue, Savéant proposed a new model to calculate TON that takes into account the electroactive catalyst material within a thin reaction layer at the electrode interface ^[11]

$$\text{TON} = \frac{n_P}{n_A} = \frac{2 kt}{1 + \exp \left[\frac{F}{RT} (E_{\text{cat}}^0 - E) \right]}$$

Where n_P and n_A are the moles of the product and the catalyst respectively, k is the observed rate constant of the overall catalytic cycle, t is the time, E_{cat}^0 is the standard potential for the formation of the product by the catalyst, and E is the operational potential.

To determine the catalytic observed rate constant, a method called foot of the wave analysis (FOWA) was developed, allowing the determination of k through the study of the CV current near the onset of the catalytic reaction^[11–14].

$$\frac{i}{i_p} = \frac{2.24 \sqrt{\frac{RT}{Fv}} 2kC_A}{1 + \exp\left[\frac{F}{RT} (E - E_{\text{cat}}^0)\right]}$$

Where i is the current at the catalytic regime, i_p is the current of the one-electron wave (in the absence of substrate), v is the scan rate and C_A is the initial concentration of substrate.

2.2 TIME-RESOLVED SPECTROSCOPY

Many chemical, physical, and biological events occur on extremely short timescales. Vibrations, molecular motions, short-lived excited states, photo-induced reactions, and proton and electron transfers are only a few examples (Figure 2.2). Time-resolved spectroscopy examines absorption, emission, or scattering phenomena in systems to investigate the temporal evolution of these processes and gain insight into their dynamics and mechanisms. Time-resolved spectroscopy is a powerful tool for studying photochemical reactions because they can be coherently initiated by applying a short-pulsed excitation.

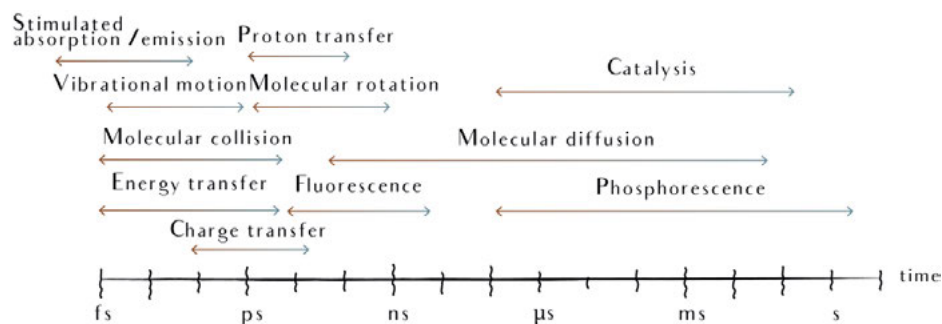


Figure 2.2. Overview of characteristic timescales of different molecular processes.

This branch of spectroscopy emerged in 1940 when the stopped-flow technique was introduced ^[15], which allowed to determine reaction kinetics in the milliseconds timescale. The next temporal resolution improvement had to wait until the 1960s when pump-probe methods were developed. In this case, two light flashes are incident on the sample; the first one is meant to perturb the system under investigation, while the second records the perturbation's effect. The delay between two flashes was controlled by a rotating shutter, giving rise to the time evolution of the response to the perturbation ^[16]. Early experimental setups allowed studies in the microsecond to nanosecond regimes. Progress, in terms of temporal resolution to even shorter timescales, became possible with the introduction of the laser (light amplification by stimulated emission of radiation). Lasers provide revolutionary precision and control over emitted light's wavelength, coherence, and pulse duration. Ultrafast lasers have achieved pulse durations of femtoseconds, enabling the detection of vibrational motions and energy and electron transfer reactions that occur in this time regime ^[17].

The excited states of molecules and their interconversions are often described with Jablonski diagrams (Figure 2.3). The absorption of a photon with sufficient energy excites a molecule from the singlet ground state (S_0) to an electronically excited singlet state (S_1, S_2, \dots, S_n). At room temperature, excitation ($S_n \leftarrow S_0$) predominantly occurs from the lowest vibrational level in S_0 . Depending on the surplus of energy of the absorbed photon, the electronically excited state is formed in a vibrationally excited state. When the molecule is in a liquid or solid, the excess vibrational energy is quickly dissipated (less than a picosecond) to the environment to produce the molecule in the lowest vibrational state of S_1 . In case a higher electronically excited singlet state was formed initially ($\geq S_2$), this thermal relaxation usually also involves internal conversion (IC), a radiation-less transition from a higher to a lower electronic state (e.g., $S_n \rightarrow S_1$). Singlet excited states, including S_1 , are usually short-lived, with lifetimes ranging from picoseconds to nanoseconds. The singlet excited state S_1 can release its excited-state energy and return to the ground state ($S_1 \rightarrow S_0$) by internal conversion or radiative emission (fluorescence). Still, other processes, either intramolecular or intermolecular, can also occur. One of these is intersystem crossing (ISC), in which there is a change in the spin multiplicity and the S_1 state converts into a triplet state ($S_1 \rightarrow T_1$). While spin-selection rules generally forbid singlet-triplet transitions, they can become weakly allowed, e.g., via spin-orbit coupling. The lowest triplet excited state (T_1) has a longer lifetime (microseconds to milliseconds) than its singlet counterpart (S_1) because the transition to the ground state ($T_1 \rightarrow S_0$) is spin-forbidden and thus slow. Radiative emission involving a $T_1 \rightarrow S_0$ transition is termed phosphorescence. ISC rates and T_1 states lifetime are often affected by the spin-orbit coupling constant, which scales with

2.

Z^4 , with Z the atomic number. Hence molecules comprising transition metals (high Z) often exhibit fast ISC and relatively short T_1 lifetime.

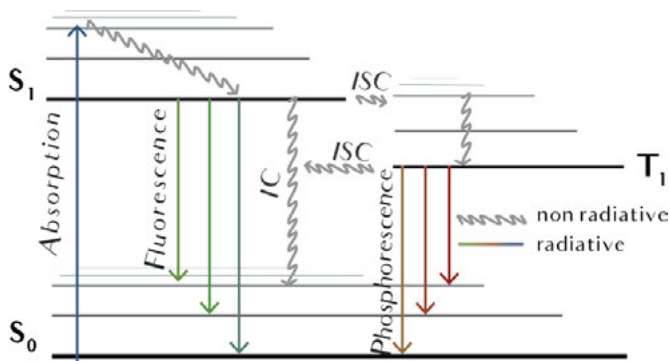


Figure 2.3. Jablonski diagram of photo-physical processes in molecules.

Diverse time-resolved spectroscopic techniques exist, and depending on the photo-physical properties intended to be observed (e.g., absorption, emission), they differ in experimental design, instrument setup and detection systems^[17–20]. Here we will cover two techniques used in this thesis. The first is time-correlated single-photon counting (TCSPC), a method to determine the excited state's lifetime by measuring its radiative decay's temporal evolution. The second is pump-probe spectroscopy which records both transient absorption and transient emission.

2.2.1 Time-correlated single-photon counting

By measuring the temporal evolution of the intensity of light emitted by a sample following pulsed excitation, it is possible to determine the excited state's lifetime (or lifetime distribution). To illustrate this, we consider a sample where many molecules go to populate an S_1 state, following a short laser pulse. Assuming the molecules fluoresce, the fluorescent light intensity $I(t)$ will be proportional to the number of excited states $n(t)$ at any time t . Assuming that the decay of the S_1 state is purely monomolecular and occurs via fluorescence, ISC, or IC only, the population n decreases following the equation:

$$-\frac{dn}{dt} = (k_F + k_{ISC} + k_{IC})n$$

$$k_F + k_{ISC} + k_{IC} = 1/\tau$$

Here k_F , k_{ISC} , and k_{IC} are the rate constants for fluorescence, intersystem crossing, and internal conversion, respectively, and τ is the excited state lifetime. Integration of the

above equation and considering that $I(t)$ is proportional to $n(t)$, the intensity for a single emitting species with time can be described by a single-exponential equation:

$$I(t) = I_0 \exp\left(-\frac{t}{\tau}\right)$$

Hence measuring $I(t)$ gives information on τ . In practice, the decay of luminescent light can follow a more complex mechanism and show biexponential, multi-exponential, or non-exponential decay behavior.

Time-correlated single-photon counting (TCSPC) is a statistical technique to measure $I(t)$. In TCSPC, one measures the time interval Δt between a short excitation pulse and the first photon emitted by the sample to arrive at the detector. By repeating this experiment many times, the distribution of Δt 's is obtained, representing $I(t)$. TCSPC can be considered a stopwatch experiment because it determines the time interval Δt that passed from the time the laser is flashed (t_{start}) and the time when the photomultiplier detects the first photon (t_{stop}). In the experiments used in this thesis, t_{start} is determined by a trigger signal that causes the laser to give a ~ 50 ps pulse at 405 nm. The first photon emitted by the sample is detected by a sensitive microchannel plate photomultiplier which generates the stop pulse at t_{stop} . The stop time is passed through a time-to-amplitude converter (TAC) which gives a voltage signal proportional to a time delay. The TAC stores the time delay ($\Delta t = t_{\text{stop}} - t_{text{start}}$) for every photon. Using a high repetition rate laser, it is possible to detect a large number of photons and measure a histogram with good statistics of the number of photons in function of the time delay Δt (Figure 2.4).

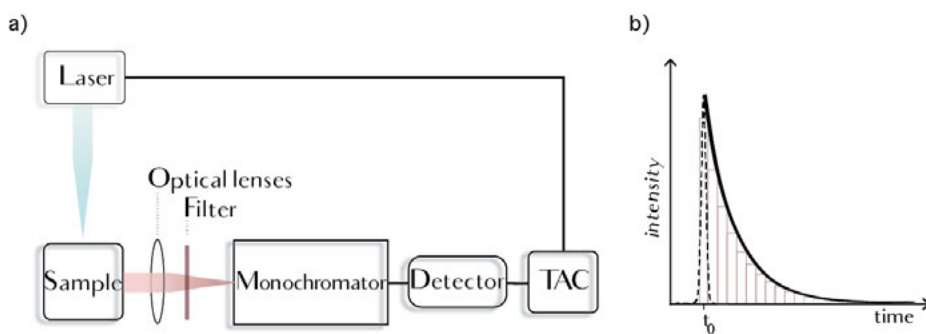


Figure 2.4. a) Scheme of TCSPC experiment. b) Fluorescence single exponential decay signal.

In TCSPC, it is essential to attenuate the excitation light sufficiently so that the detector record only "first" photons. In practice, this is achieved when the average count rate at the detector is 1-5 % of the excitation rate. The excitation rate can be high, up to

several tens of MHz, but care must be taken to ensure that the excitation rate is low compared to the inverse lifetime ($1/\tau$). TCSPC is a versatile, robust, and inherently sensitive method. Changes in the light intensity or pulse instability do not affect the measurements as it relies on photon counting only. Moreover, high-energy laser pulses are not needed. On the other hand, a limitation is given by the detection of a single wavelength, which makes the recording of entire time-resolved spectra a tedious job. TCSPC studies described in this thesis were performed on an Edinburgh Instruments LifeSpec-PS spectrometer by photo-excitation with a 405 nm picosecond laser (PicoQuant PDL 800B) operated at 100 kHz and by detection with a Peltier-cooled Hamamatsu microchannel plate photomultiplier (R3809U-50).

2.2.2 Pump-probe spectroscopy

Pump-probe spectroscopy is a technique that allows measuring (probe) the absorption spectrum of transient species generated by optically exciting a sample with a short flash of light (pump). It uses two distinct light sources, a pump pulse and a probe pulse, and records changes in optical density (ΔOD) by measuring the intensity of the probe light before and after the pump pulse. By varying the time delay between pump and probe, spectral changes can be monitored over time.

Usually, a pump pulse of high intensity is used to excite the sample to bring a sufficiently large number of chromophores to the excited state. The probe pulse is lower in intensity and can be tuned to investigate different parts of the electromagnetic spectrum. The measured change in absorbance or optical density (ΔOD) is a function of the wavelength and the time delay (Δt) between the pump and the probe flash. A schematic representation of the experimental setup is shown in Figure 2.5. The ΔOD , *i.e.*, the change in optical density of the sample after a laser pump flash, can be determined from the transmitted light by:

$$\Delta OD(\lambda, t) = \log \left(\frac{I_0(\lambda)}{I_{\text{pump}}(\lambda, t)} \right) - \log \left(\frac{I_0(\lambda)}{I_{\text{no-pump}}(\lambda)} \right) = \log \left(\frac{I_{\text{no-pump}}(\lambda)}{I_{\text{pump}}(\lambda, t)} \right)$$

Here $I_0(\lambda)$ is the probe light spectrum before passing the sample, $I_{\text{no-pump}}(\lambda)$ is the probe light spectrum passing through the sample without prior excitation. $I_{\text{pump}}(\lambda, t)$ is the probe light spectrum passing the sample at a time t after excitation with a pump pulse. Note that $\Delta OD(\lambda, t)$ is not dependent on the spectrum or intensity of the incident probe light $I_0(\lambda)$.

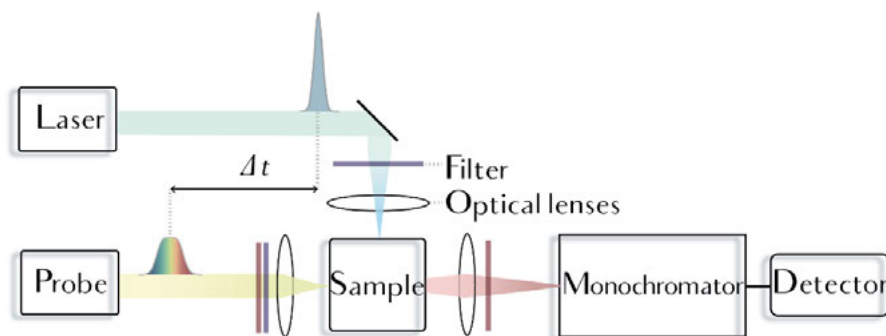


Figure 2.5. Scheme of pump-probe laser spectroscopy.

The $\Delta OD(\lambda, t)$ spectrum contains contributions of different signals and can be positive or negative in sign (Figure 2.6). A prominent feature often observed in transient spectra is the so-called ground state bleach $\Delta OD < 0$. When a sample fraction is excited, the same fraction of chromophores no longer contributes to the ground state absorption, yielding a negative ΔOD in this region. The second factor is stimulated emission $\Delta OD < 0$. This particular emission occurs when the probe light interacts with an excited-state molecule and induces the emission of a second photon with the same direction and polarization as the incident photon ($h\nu + S_1 \rightarrow 2h\nu + S_0$). Because stimulated emission represents an increase in probe light intensity following a pump pulse, it is also registered as $\Delta OD < 0$. Another process affecting the signal is excited-state absorption (e.g., $S_n \leftarrow S_1$). Excited-state absorption represents optically-allowed transitions from the excited state to higher-excited states induced by the probe light. The new absorption results in an attenuation of the probe light spectrum and effects in a positive ΔOD . Lastly, and similarly to the previous one, if a new species is generated along the time of the experiment as a consequence of a reaction, the transient or long-lived species will show a positive ΔOD [21]. The ΔOD , as a function of t and the wavelength λ , can be described by the Beer-Lambert law of the single absorption variations:

$$\Delta OD(\lambda, t) = -\varepsilon_g(\lambda)C_{ex}(t)d - \phi(\lambda)C_{ex}(t) + \varepsilon_{ex}(\lambda)C_{ex}(t)d + \varepsilon_T(\lambda)C_T(\lambda)d$$

Here ε and C are the extinction coefficient and the concentration, respectively, of the ground state (g), the excited state (ex), and of any transient or long-lived species (T), ϕ is the photon flux contribution to the stimulated emission, and d is the path length of the sample.

Pump-probe laser spectroscopy setups are most of the time designed for either spectral resolution or kinetic resolution. In spectral mode, the probe is directed to a spectrograph and a multi-channel detector (e.g., CCD camera). After going through the sample, the whole spectrum is recorded at a selected time following the pump pulse. In

kinetic mode, a relevant wavelength is selected by a monochromator and probe light is detected by a single-channel detector (e.g., PMT or photodiode) and ΔOD is stored as a function of time in a kinetic trace (Figure 2.6)

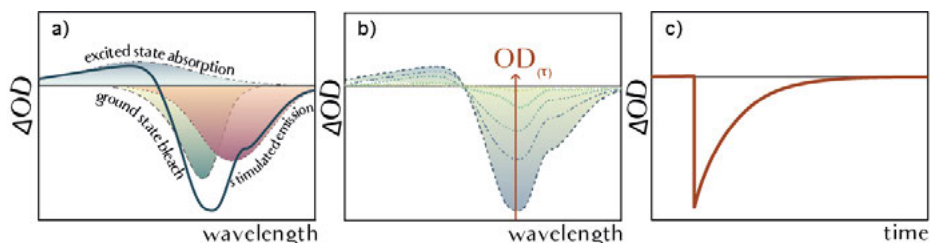


Figure 2.6. a) Example of transient absorption spectrum and its contributions in $\Delta OD(\lambda, t)$. b) two-dimensional data matrices $\Delta OD(\lambda, t)$, and c) kinetic trace of the $\Delta OD(\lambda, t)$ over the time.

Pump-probe experiments described in this thesis for transient absorption kinetic analysis were performed on an Applied Photophysics, LKS.8 flash photolysis spectrometer. A Q-switched Nd:YAG laser (Quantel, BrilliantB) provided sample photoexcitation that delivered tripled frequency pulses at 532 nm (~ 7 ns) and tuned to the desired wavelength by an optical parametric oscillator (OPO). Probe light was supplied by an un-pulsed (for traces longer than 100 μ s) or pulsed (for shorter time windows) 150 W xenon lamp. The transmitted light wavelength was selected by a monochromator and set to a bandwidth of 1 nm before reaching the 5-stage P928 photomultiplier tube (Hamamatsu). The signal was digitized using an Agilent Technologies Infinium digital oscilloscope (600 MHz).

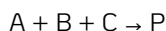
Analysis of spectroscopic properties that vary linearly with the concentration, e.g., absorption, can be used to directly determine reaction rates as the time derivative of optical signatures. Thus, it is possible to use optical signals for data analysis. Kinetic analysis of transient absorption signals is used to elucidate the reaction mechanism responsible for the decay (radiative or not) of an excited state chromophore or the energy or electron transfer between the latter and a suitable reactant present in the sample. Follow-up reactions can be studied if the newly generated intermediate gives rise to a spectroscopical feature detectable by the system. Unimolecular processes, like fluorescence, follow a first-order single exponential decay. Considering a transformation proceeding irreversibly:



The corresponding rate laws before and after integration are:

$$-\frac{d[A]}{dt} = k_1 [A] \quad [A] = [A]_0 \exp(-k_1 t)$$

Here $[A]$ and $[A]_0$ are the concentrations of A at the time t and at the time t_0 , respectively. k_1 is the reaction rate constant. The same method can be applied to higher-order reactions under pseudo-first-order conditions. In this case, the concentrations of all but one reactant are present in significant excess ($[B]$ and $[C]$), which allows the assumption that their concentration remains constant throughout the experiment. The kinetic order is then reduced to the one species at a lower concentration ($[A]$)



$$-\frac{d[A]}{dt} = k [A] [B] [C] \quad -\frac{d[A]}{dt} = k_{\text{obs}} [A]$$

$$[A](t) = [A]_0 \exp(-k_{\text{obs}} t) \quad k_{\text{obs}} = k [B][C]$$

Here we identify an experimental rate constant k_{obs} as a function of the actual reaction rate constant k and the concentration of the reactants in excess.

Many chemical processes are more complex than the above examples and require more detailed mathematical derivations. Generally, we recognize three categories: reversible, concurrent (first-order), and consecutive or multistep reactions. Concurrent reactions include processes leading to the products from the same starting material (e.g., radiative and non-radiative emissions) or competing chemical reactions evolving different products. In a generic case, we can consider,

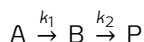


Where the experimentally observed rate constant is composed of the sum of the single constant of each process, we can then identify the rate law and its time integral:

$$-\frac{d[A]}{dt} = (k_1 + k_2 + k_3) [A] \quad [A](t) = [A]_0 \exp\left(-t \sum k_n\right)$$

With $\sum k_n = k_1 + k_2 + k_3 + \dots k_n$. This model assumes the reactions not being in equilibrium. Kinetic analysis through the detection of any product (P_1, P_2, P_3) will always reflect $\sum k_n$, as the formation of any P_n relates to the loss of A and consequently, all reactions it can undergo.

Another important reaction mechanism is based on multistep reactions, in which the product of a first reaction, referred to as intermediate, is further depleted due to an additional reaction producing the final product.



The rate laws can be written for each species as:

$$-\frac{d[A]}{dt} = k_1[A] \quad \frac{d[B]}{dt} = k_1[A] - k_2[B]$$

The consumption profile of A obeys, as part of a simple first-order reaction, a single exponential function over time. The intermediate B instead follows the equation:

$$[B](t) = [A]_0 \frac{k_1}{k_2 - k_1} (\exp(-k_1 t) - \exp(-k_2 t))$$

Furthermore, its concentration is expected to reach a maximum at:

$$t_{\max} = \frac{1}{k_1 - k_2} \ln \left(\frac{k_1}{k_2} \right)$$

After which, the conversion to P takes over and its concentration decreases.

Further development of this model, as introducing a reversible transformation between A and B and assuming that the conversion of B into P is so fast that B is not appreciably observed, results in the steady-state approximation. For a more detailed derivation of this method or extensive mechanistic and kinetic analysis, it is possible to rely on other texts ^[22,23].

2.3 SOLAR CELL CHARACTERIZATION

2.3.1 Photo-to-electrical energy

The photovoltaic effect involves the direct conversion of light into an electrical potential. The effect occurs when a semiconductor absorbs a photon with an energy $h\nu > E_g$, where E_g is the bandgap of the semiconductor material, *i.e.*, the energy gap between the valence and conduction bands. Photoexcitation thus creates an electron-hole pair. Suppose these charge carriers are separated and collected at opposite electrode contacts. In that case, the electrical potential generated can create an electrical current in an external circuit where the energy can be used directly or stored ^[24]. Since the development of the first p-n junction crystalline silicon photovoltaic cell in

1956, enormous progress has been made. Nowadays, widely different materials are used and considered for photovoltaic energy conversion. Most abundant are crystalline silicon cells (c-Si). Still, more recently, thin-film solar cells are developed ^[25], e.g., cells based on amorphous silicon (a-Si), cadmium telluride (CdTe), gallium indium diselenide (CIGS), or gallium arsenide (GaAs). The third and latest generation of materials for this technology includes organic (polymer) solar cells ^[26], dye-sensitized solar cells (DSSC) ^[27], and metal-halide perovskite solar cells ^[28]. While different absorber materials can be used, they must possess a defined optical bandgap. In the case of organic molecules, the optical bandgap is given by the difference in energy between the highest occupied and lowest unoccupied molecular orbitals (HOMO and LUMO). Without a bandgap, photoexcitation would not give rise to a splitting of the quasi-Fermi levels of electrons and holes or chemical potential.

2.3.2 Solar cell efficiency

Solar irradiance spectrum and its intensity at the Earth's surface depends on many factors such as geographical latitude, altitude, the angle of incidence varying throughout the day, and atmospheric weather events. Because of these variables, a reliable metric of comparison for solar cell performances requires standard illumination conditions. This is achieved by the air mass (AM) concept. The AM is a measure of the distance that sunlight travels across the Earth's atmosphere when it collides with a given angle θ relative to the zenith. The AM1.5G spectrum ($\theta = 48.2^\circ$; $1/\cos \theta = 1.5$) is the standard spectrum and contains both direct and globally (G) diffuse light. It is defined with a light intensity of 100 mW cm^{-2} . Usually, solar simulators are employed as a source of radiation for testing solar cells. The spectrum of such a solar simulator is often quite different from the AM1.5G spectrum and corrections for the spectral mismatch are needed in such cases.

The solar cell response is usually characterized by its J - V curve under (simulated) AM1.5G illumination, which shows the current density produced when a specific voltage is established. J - V curves are recorded by sweeping the potential and registering the current density. The cell response is subject to illumination conditions. In the dark, the cell will produce a minimal current flow (dark current) due to the acceleration of thermally generated charges because of an electric field. The dark current density can be described by the diode equation ^[29].

$$J(V) = J_0 \left(\exp \left(\frac{qV}{k_B T} \right) - 1 \right)$$

Where J_0 is the dark saturation current density, V is the potential across the cell, q is the elementary charge, and k_B is the Boltzmann constant. Under illumination, a

2.

photocurrent density is produced (J_{ph}), which opposes the dark current density under forward bias ($V > 0$).

$$J(V) = J_0 \left(\exp \left(\frac{qV}{k_B T} \right) - 1 \right) - J_{ph}$$

From the J - V curve characteristics, photovoltaic parameters of the cells can be identified. In particular, the short-circuit current density (J_{SC}) is the current density flowing through the cell when it is not subjected to any voltage bias. The open-circuit voltage (V_{OC}) is the voltage across the cell in the absence of any current. The output power density P of a cell is the product of voltage and the current density (Figure 2.7) and maximizes in the maximum power point (V_{max} , J_{max}) where:

$$P_{max} = V_{max} J_{max}$$

The relation between P_{max} and J_{SC} and V_{OC} is commonly described by the fill factor (FF). The fill factor is a dimensionless parameter that indicates the ratio of the maximum power of the cell relative to the product of J_{SC} and V_{OC} :

$$FF = \frac{J_{max} V_{max}}{J_{SC} V_{OC}}$$

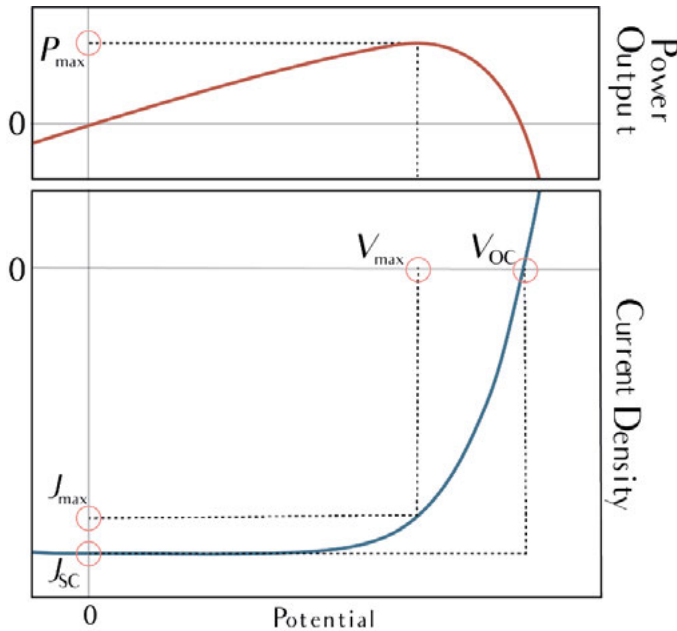


Figure 2.7. J - V curve dark/illumination, J - V with characteristic parameters and power output curve.

The overall performance of a photovoltaic cell is expressed by its power conversion efficiency (PCE), which is the ratio of the maximum energy output to the incident light power.

$$\text{PCE} = \frac{P_{\max}}{P_{\text{in}}} = \frac{J_{\text{SC}} V_{\text{OC}} \text{FF}}{P_{\text{in}}}$$

It is important to note that J_{SC} , V_{OC} , FF, and PCE all depend on the illumination conditions and can only be compared to other cells when standard measurement conditions (25 °C, AM1.5G spectrum at 100 mW cm⁻²) are used.

2.3.3 Multijunction PV

The maximum achievable power conversion efficiency of a solar cell depends on the bandgap of the absorber material. As mentioned above, incident photons require photon energy equal to or larger than the bandgap to be absorbed. All photons with lower energy are transmitted and lost. Furthermore, photons with energies exceeding the bandgap produce electrons and holes that will thermalize to the conduction and valence band edges, dissipating their excess energy. Both transmission and thermalization limit the power conversion efficiency of solar cells. While narrow-bandgap semiconductors reduce transmission losses and increase J_{SC} , they result in higher thermalization losses and a lower V_{OC} . Wide-bandgap semiconductors provide opposite effects, a reduction of J_{SC} and an increase in V_{OC} . For a solar cell based on a single absorber layer, the maximum theoretical efficiency in AM1.5G light is further limited by the cell temperature and in the detailed-balance limit is 33.7 % at a bandgap of about 1.3 eV.

A way around this problem is to build a solar cell with different absorber layers, each with a different bandgap and split the solar spectrum over these cells accordingly. This class of photovoltaic cells is referred to as multijunction solar cells. Multijunction solar cells can break the thermodynamic limit of 33.7 % for a single-junction cell [30]. The typical multijunction configuration consists of a cell in which the semiconductor with the widest bandgap is placed on top, and stacked underneath are semiconductors with progressively narrower bandgaps. This results in high-energy photons being absorbed in the top cell and low-energy photons transmitted to the next cell. In this way, a simultaneous reduction of thermalization and transmission losses can be achieved. The theoretical power conversion limit for two junctions (tandem) is ~46 %, for three junctions ~50 %, and so on up to ~65 % for a potentially infinite number of junctions. Next to different bandgap absorbers, a monolithic multijunction cell also comprises recombination layers or tunnel junctions placed between the different sub-cells needed to connect the sub-cells electrically. In a monolithically-stacked series-connected

multijunction cell, the open-circuit voltage equals the sum of open-circuit voltages of the sub-cells. At the same time, the short-circuit current density is governed by the sub-cell that produces the lowest photocurrent. Hence, multijunction solar cells are often designed to provide photocurrent matching, such that each sub-cell generates the same amount of photocurrent when the total device is illuminated with AM1.5G light. Current matching can be achieved by distributing the light absorbed over the sub-cells, *e.g.*, by adjusting the bandgap, layer thickness, optical interference, or a combination thereof.

Multijunction solar cells are particularly interesting for the development of water-splitting devices. Two or more sub-cells connected in series can provide an operational voltage that exceeds the thermodynamic potential of 1.229 V for the overall water splitting, plus eventual overpotential losses. Interestingly, the optimal solar cell for a chemical reaction is not necessarily the most efficient for producing electrical energy. The best solar cell is the one that has the highest photocurrent at the operating voltage needed to drive the chemical reaction. Any higher voltage than the cell can produce is not required.

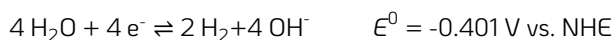
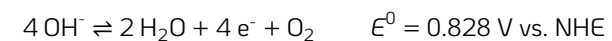
2.4 PV-EC DESIGN AND CHARACTERIZATION

We have now described the main elements for a photo-electrochemical water splitting system, from the photovoltaic (PV) conversion of sunlight to the evolution of the products at the catalytic centers in an electrochemical cell (EC). In this section, we will consider thermodynamic aspects of hydrogen production and the different configuration for a working device. For water splitting, the following equation applies:

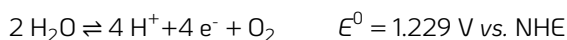


2.4.1 H₂ conversion thermodynamics

As mentioned in the previous chapter, hydrogen has an energy density of 120 MJ kg⁻¹ [31], which outcompetes any other chemical fuel. The electrochemical water splitting reaction can be divided into two half-reactions. Depending on the operational pH, we can distinguish between the hydrogen evolution reaction (HER) and the oxygen evolution reaction (OER) in alkaline conditions (pH 14):



and in acidic media (pH 0):



Hence, theoretically, photons having an energy equal to or higher than 1.229 eV have the potential to drive the reaction in light-driven systems. In practice, additional photon energy is required because potential losses occur in the photovoltaic conversion (η_{PV}), in the transport (η_{trans}), and in the overpotentials related to the catalytic processes (η_{cat}) in each of the half-reactions depending on the choice of the catalysts at the cathode and the anode ($\eta_{\text{cat}} = \eta_{\text{HER}} + \eta_{\text{OER}}$). As a consequence, the required photon energy must satisfy:

$$h\nu \geq E_g > q(\Delta E^0 + \eta_{\text{PV}} + \eta_{\text{trans}} + \eta_{\text{cat}})$$

For photo-electrochemical reactions where the electrochemical process is driven by a photovoltaic cell, either a wide-bandgap single junction, multijunction, or a combination of series-connected single-junction cells, the operating voltage of the photovoltaic cell, V_{op} , must satisfy:

$$V_{\text{op}} > \Delta E^0 + \eta_{\text{trans}} + \eta_{\text{cat}}$$

One of the main performance parameters for light-driven hydrogen conversion devices is the solar-to-hydrogen (STH) energy conversion efficiency, defined as the ratio of the hydrogen energy produced and the light energy input [32,33].

$$\eta_{\text{STH}} = \frac{\phi_{\text{H}_2} \Delta G}{P_{\text{in}}}$$

Where ϕ_{H_2} is the molar flow rate of hydrogen produced per illuminated area in [$\text{mol s}^{-1} \text{m}^{-2}$], ΔG is the Gibbs free energy of formation of hydrogen (237 kJ mol^{-1}), and P_{in} is the solar irradiance (assumed to correspond to AM 1.5G at 1 kW m^{-2}). Alternatively, the enthalpy change ($\Delta H = 286 \text{ kJ mol}^{-1}$) can be used, which corresponds to a thermoneutral potential of $V_{\text{TN}} = 1.48 \text{ V}$ for water splitting and is relevant when the H_2 produced is combusted instead of being converted into electricity in a fuel cell. The Gibbs free energy gives a more conservative estimate. Since the gas flow at the outlet of the electrochemical cell contains a fraction of water vapor, and the measurement itself would require very sensitive flowmeters for lab-scale devices, most results in the literature are reported as a function of the operating current (I_{op}) through the electrodes:

$$\phi_{\text{H}_2} = \frac{I_{\text{op}} \eta_{\text{F}}}{2FA_{\text{PV}}}$$

where η_F is the Faradaic efficiency of the electrochemical cell, which accounts for undesired reactions or possible degradation processes, and A_{PV} is the area of the photovoltaic cell. The STH efficiency can therefore be summarized as follows:

$$\eta_{STH} = \frac{I_{op} \eta_F \Delta G}{2FA_{PV} P_{in}} = 1.23 \times \frac{\eta_F J_{PV}}{P_{in}}$$

Where J_{PV} is the current density at which the solar cell operates.

2.5 REFERENCES

- [1] A. J. Bard, L. R. Faulkner, *Electrochemical Methods: Fundamentals and Applications*, John Wiley & Sons, Inc., **2001**.
- [2] J.-M. Savéant, *Elements of Molecular and Biomolecular Electrochemistry*, John Wiley & Sons, Inc., **2006**.
- [3] R. G. Compton, C. E. Banks, *Understanding Voltammetry*, World Scientific **2018**.
- [4] J. O. Bockris, A. K. N. Reddy, M. Gamboa-Aldeco, *Modern Electrochemistry second edition: Fundamentals of Electrodics*, Springer publishing company, **2000**.
- [5] P. Connor, J. Schuch, B. Kaiser, W. Jaegermann, *Z. Phys. Chem.* **2020**, 234, 5, 979–994.
- [6] S. Trasatti, O. A. Petrii, *Pure Appl. Chem.* **1991**, 63, 711–734.
- [7] J. M. Savéant, K. B. Su, *J. Electroanal. Chem. Interfacial. Electrochem.* **1984**, 171, 341–349.
- [8] J.M. Savéant, *Chem. Rev.* **2008**, 108, 7, 2348–2378.
- [9] D. J. Martin, B. D. McCarthy, E. S. Rountree, J. L. Dempsey, *J. Chem. Soc. Dalton Trans.* **2016**, 45, 9970–9976.
- [10] S. Kozuch, J. M. L. Martin, *ACS Catal.* **2012**, 2, 12, 2787–2794.
- [11] C. Costentin, S. Drouet, M. Robert, J. M. Savéant, *J. Am. Chem. Soc.* **2012**, 134, 27, 11235–11242.
- [12] C. Costentin, J.-M. Savéant, *ChemElectroChem* **2014**, 1, 7, 1226–1236.
- [13] R. Matheu, S. Neudeck, F. Meyer, X. Sala, A. Llobet, *ChemSusChem* **2016**, 9, 23, 3361–3369.
- [14] V. C. C. Wang, B. A. Johnson, *ACS Catal.* **2019**, 9, 8, 7109–7123.
- [15] B. Chance, *J. Franklin Inst.* **1940**, 229, 737–766.
- [16] G. Porter, *Science*, **1968**, 160, 3834, 1299–1307.
- [17] E. P. Farr, J. C. Quintana, V. Reynoso, J. D. Ruberry, W. R. Shin, K. R. Swartz, *J. Chem. Educ.* **2018**, 95, 5, 864–871.
- [18] K. Ishii, Y. Hirose, H. Fujitsuka, O. Ito, N. Kobayashi, *J. Am. Chem. Soc.* **2001**, 123, 4, 702–708.
- [19] M. Zhang, M. de Respinis, H. Frei, *Nat. Chem.* **2014**, 6, 4, 362–367.
- [20] S.-C. Lin, C.-C. Chang, S.-Y. Chiu, H.-T. Pai, T.-Y. Liao, C.-S. Hsu, W.-H. Chiang, M.-K. Tsai, H. M. Chen, *Nat. Commun.* **2020**, 11, 3525.
- [21] R. Berera, R. van Grondelle, J. T. M. Kennis, *Photosynth. Res.* **2009**, 101, 105–118.
- [22] J. H. Espenson, *Chemical Kinetics and Reaction Mechanism*, McGraw-Hill Education **1981**.
- [23] T. Turányi, A. S. Tomlin, *Analysis of Kinetic Reaction Mechanisms*, Springer publishing company, **2014**.

- [24] S. M. Sze, K. K. Ng, in *Physics of Semiconductor Devices*, John Wiley & Sons, Inc., **2006**, pp. 5–75.
- [25] M. A. Green, K. Emery, D. L. King, S. Igari, W. Warta, *Pro. Photovolt.: Res. Appl.* **2003**, *11*, 347–352.
- [26] H. Spanggaard, F. C. Krebs, *Sol. Energy Mater. Sol. Cells* **2004**, *83*, 125–146.
- [27] B. O'Regan, M. Grätzel, *Nature* **1991**, *353*, 737–740.
- [28] N.G. Park, *Mater. Today* **2015**, *18*, 2, 65–72.
- [29] A. Kitai, *Principles of Solar Cells, LEDs and Diodes: The Role of the PN Junction*, John Wiley & Sons, Inc., **2011**.
- [30] W. Shockley, H. J. Queisser, *J. Appl. Phys.* **1961**, *32*, 3, 510–519.
- [31] K. T. Møller, T. R. Jensen, E. Akiba, H. Li, *Prog. Nat. Sci.: Mater. Int.* **2017**, *27*, 1, 34–40.
- [32] S. Tembhurne, F. Nandjou, S. Haussener, *Nat. Energy* **2019**, *4*, 399–407.
- [33] M. T. Winkler, C. R. Cox, D. G. Nocera, T. Buonassisi, *Proc. Natl. Acad. Sci.* **2013**, *110*, 12, 1076–1082.

3

TETRA-AMIDATE MACROCYCLIC LIGAND COPPER-BASED WATER OXIDATION CATALYSTS

3.1 INTRODUCTION

In the last decades, research on catalysts has been pushed towards the use of first-row transition metals to find viable alternatives to replace noble metal-based catalysts. In this regard, alternatives to molecular iridium- and ruthenium-based water oxidation catalysts (WOCs) are also being explored. The first example of a molecular copper-based WOC was reported by Mayer *et al.* ^[1], where a bipyridyl system and two hydroxy ions complexed the copper center, $[\text{Cu}(\text{bpy})(\text{OH})_2]$ (Figure 3.1a), which showed activity in aqueous media at $\text{pH} > 12$. Even though they proved the homogeneous nature of the active species, this is not always the case when first-row transition metal complexes are considered ^[2].

Llobet *et al.* have reported a tetra-anionic ligand system based on an acyclic tetra-amidate scaffold ^[3] (Figure 3.1b). Besides having a multi-dentate structure and a strong anionic character, they showed that this family of catalysts owes their activity to the redox non-innocent character of the ligand orbitals, accommodating oxidative equivalents during the catalytic cycle. Furthermore, extending the π -conjugation led to an improvement in catalytic activity, as well as in the overpotential for water oxidation ^[4]. The latter effect can be rationalized by the fact that the positively charged intermediates are delocalized over a larger ligand framework, stabilizing these states and facilitating their formation. A limitation of this copper-based catalyst category is the operational pH, as the catalysts do not show appreciable activity when the pH is brought below 11. Protonation of the amides seems to be detrimental for the coordination of the copper ion. Similarly, changes in the local pH following the liberation of four protons in each catalytic cycle might also play a role in the long-term stability of the complexes.

The lability issue was solved by introducing a macrocyclic ligand. The first example of a tetra-amidate macrocycle ligand-based complex for water oxidation was described by Collin *et al.* [5,6] and it was then adapted for a copper ion center by Llobet *et al.* The new macrocyclic copper complex ($[\text{CuMac}]^{2-}$; Figure 3.1c) displays a broader pH range in which it is stable and active, reaching pH=7 as a lower operational limit [7]. It demonstrates that introducing a macrocyclic ligand enhances the stability against amide protonation and increases the ruggedness for metal displacement.

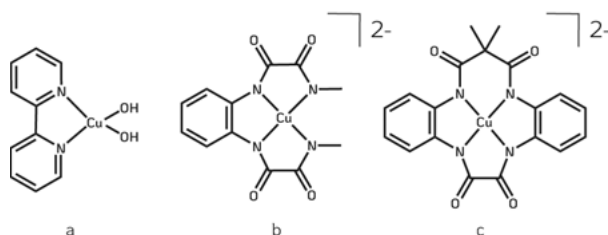


Figure 3.1. State-of-the-art copper-based WOC. a) $[\text{Cu}(\text{bpy})(\text{OH})_2]$ from Mayer *et al.* [1] b) Acyclic tetra-amidate copper catalyst from Llobet *et al.* [8]. c) Macrocyclic tetra-amidate copper catalyst from Llobet *et al.* [8] [7].

This family of catalysts was found to follow a water nucleophilic attack (WNA) type of mechanism [9,10]. In this reaction mechanism scenario, the activated and high valence copper-ligand system interacts with a water source (as H_2O or OH^-) in the formation of the O-O bond. The reaction step yields a hydroperoxide species ($-\text{OOH}$), and it is subsequently oxidized to release molecular oxygen and restore the catalyst in its reduced form. Often transition metal catalysts produce the hydroperoxide bond via WNA mechanisms, reported as concerted two-electron transfers [11–13]. However, recently, a consecutive two single-electron transfer reaction (SET-WNA) has been proposed for tetra-amidates copper complexes [8–10]. The rational elucidation for such a mechanism resides in the inaptitude of first-row transition metals to reach high oxidation states, able to extract enough charge from the hydroxo group at once upon water attack. Thus, two discrete electron transfers are necessary to allow the charge re-organization within the non-innocent ligand and metal center.

Our work aims to explore derivatives of the tetra-amidate macrocyclic ligand (TAML) motif (15,15-dimethyl-8,13-dihydro-5*H*-dibenzo[*b,h*][1,4,7,10] tetra-azacyclotridecine-6,7,14,16(15*H*,17*H*)-tetraone) (**4**) (Scheme 3.1) to enhance their activity by modifying the electronic distribution of the ligand system. Simultaneously, we want to introduce specific moieties that can be exploited in immobilizing the WOC onto a heterogeneous support/electrode. For the acyclic tetra-amidate copper complex, it was described that the introduction of progressively more electron-donating groups on the backbone of the ligand reduces the potential required for the metal oxidations

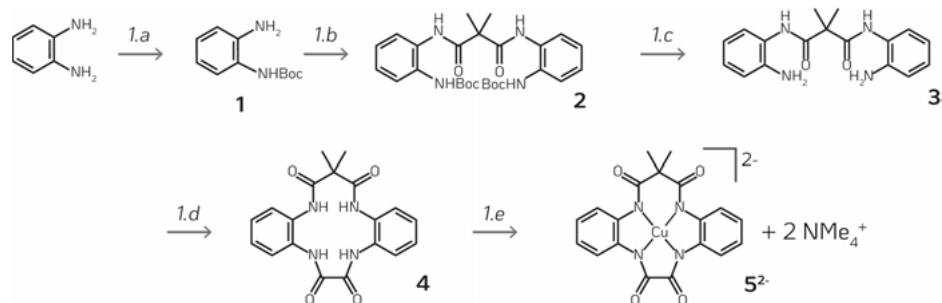
and the overpotential for catalysis^[3]. However, reducing the overpotential comes at a price in terms of its catalytic activity, while it may preserve its stability due to lower oxidative strength toward water^[3,14]. On the other hand, the inclusion of electron-withdrawing groups improves the catalytic activity, as they increase the reactivity of cationic intermediates^[15–17]. A drawback of this design approach is the higher potential required to carry out the oxidation of the complexes and, therefore to oxidize water.

This chapter describes the synthesis of two TAML-based copper complex derivatives with electron-withdrawing substituents that are investigated by electrochemical methods for their ability to be catalytically active in water oxidation. The rational design behind the introduction of carboxylate moieties is the later use of such catalyst for heterogenized anode material by electrostatic interaction with metallic and/or graphitic surfaces, as well as the fabrication of metallic organic frameworks (MOFs). Despite the expected increment in overpotential that the functionalities bring, the introduced groups will be found to compromise the kinetics of the water oxidation reaction.

3.2 RESULTS AND DISCUSSION

3.2.1 Material synthesis and characterization

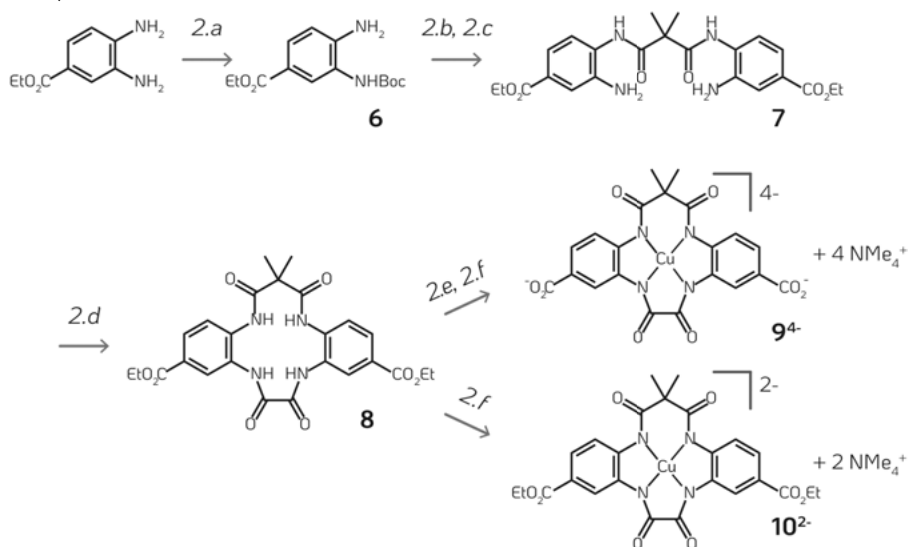
The parent TAML ligand (**4**) was prepared according to a literature strategy (Scheme 3.1) and converted into the $[\text{CuMac}]^{2-}$ catalyst (**5²⁻**)^[6,7]



Scheme 3.1. Synthetic route for TAML (**4**) and $[\text{CuMac}]^{2-}$ preparation. 1.a) Di-tert-butyl dicarbonate (1 eq), Et_3N , THF. Inert atmosphere, 0 °C to room temperature overnight, 76%. 1.b) Dimethylmalonyl dichloride (0.5 eq), pyridine, THF, inert atmosphere, overnight. 1.c) EtOAc/HCl , 2 hours, 92% (step *b* and *c*). 1.d) Oxalyl chloride, Et_3N , THF, inert atmosphere, 88%. 1.e) $\text{Cu}(\text{ClO}_4)_2$, NMe_4OH , MeOH , 98%.

Similarly, a derivative of **5**²⁻ was synthesized, bearing a carboxylate moiety on both aromatic rings of the macrocycle (Scheme 3.2). The synthetic strategy remained the same, except for using 3,4-diaminobenzoate as the starting material. Two complexes, **9**⁴⁻ and **10**²⁻, were prepared. In the case of **9**⁴⁻, the ethyl esters were hydrolyzed before the metal insertion, while for **10**²⁻, the esters were maintained on the ligand system.

The anionic copper complexes were synthesized successfully, and their (distorted) square planar geometry was confirmed by single-crystal X-ray diffraction (Figure 3.2). The ester and carboxylate substituent groups do not influence the Cu-N averaged distances (1.902, 1.905, and 1.904 Å for **5**²⁻, **9**⁴⁻, and **10**²⁻ respectively) nor the N-Cu-N bond angles (85.5° and 103.5° for **5**²⁻; 85.5° and 103.1° for **9**⁴⁻; 85.3° and 103.9° for **10**²⁻ respectively for the 5-membered rings and the 6-membered ring around the metal center).



Scheme 3.2. Synthetic route for preparation of [CuMac(COO)₂]⁴⁻ and [CuMac(COOEt)₂]²⁻. 2.a) Di-ter-butyl dicarbonate (1 eq), Et₃N, THF. Inert atmosphere, 0 °C to room temperature overnight, 73 %. 2.b) Dimethylmalonyl dichloride (0.5 eq), pyridine, THF, inert atmosphere, overnight, 2.c) EtOAc/HCl, 2 hours, 92 %. 2.d) Oxalyl chloride, Et₃N, THF, inert atmosphere, 86 %. 2.e) NaOH, EtOH, 80 %. 2.f) Cu(ClO₄)₂, NMe₄OH, MeOH, 76 %.

The planar geometry along the two phenyl amidate rings reveals that the π -system is delocalized over the entire ligand framework. In the case of **9**⁴⁻ and **10**²⁻, the C=O units of the carboxyl groups also lay in the same plane as the π -system, suggesting that the electron-withdrawing character of the substituents affects the electronic properties of the metal center. Single crystals were obtained from methanolic solutions, and no solvent molecules were found to occupy the axial position in the solid-state samples of

any of the analyzed complexes. Other techniques such as NMR spectroscopy, mass spectrometry, and elemental analysis were employed to characterize and confirm the identity and purity of the target complexes (see experimental details).

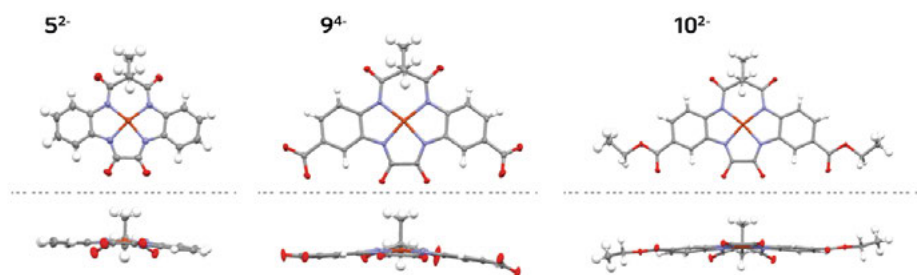


Figure 3.2. Ellipsoid structural representation of the copper complexes investigated, obtained by X-ray structure analysis. Color code: carbon grey, hydrogen white, oxygen red, nitrogen blue, copper orange. Solvent molecules and counter-ions are omitted for clarity.

3.2.2 Electrochemical and optical properties

The electrochemical properties of 10^{2-} were determined by cyclic voltammetry (CV) in acetonitrile (MeCN) solution containing tetrabutylammonium hexafluorophosphate (TBAPF₆). Figure 3.3a shows two chemically reversible redox couples that are assigned to the oxidations of 10^{2-} to 10^{-} at $E_{1/2} = -1.00$ V (vs. Fc⁺/Fc) and 10^{-} to 10 at $E_{1/2} = 0.23$ V (vs. Fc⁺/Fc). The peak-to-peak separations (ΔE_p) are 80 mV and 72 mV, respectively. These waves are assigned to a Cu^{II} to Cu^{III} oxidation and oxidation of the ligand, respectively, in analogy with results reported for [CuMac]²⁻ (5^{2-})^[3]. The homogeneous nature of the redox process was checked by varying the potential scan rate (v), showing that the current is proportional to the square root of the scan rate (Figure 3.3b) as expected for a freely diffusing electroactive species by the Randles-Ševčík equation. When the potential is scanned more positively, a new irreversible oxidation wave arises at 0.63 V (vs. Fc⁺/Fc), which involves a multi-electron process, as is clear from the magnitude of the current intensity. At the same time, this causes a loss in the reversibility of the electron transfer at 0.23 V (vs. Fc⁺/Fc), consistent with some degradation process of the ligand at high oxidative potential.

The cyclic voltammogram of 9^{4-} in acetonitrile shows a stable and chemically reversible one-electron process at $E_{1/2} = -1.14$ V (vs. Fc⁺/Fc) associated with a 9^{4-} to 9^{3-} oxidation. This wave was stable and completely reversible over 50 scans (Figure 3.4a). When the electrochemical behavior of complex 9^{4-} was evaluated at higher anodic

3.

potentials, an irreversible wave appeared at -0.01 V (vs. Fc^+/Fc), which features a peak intensity of a multi-electron process.

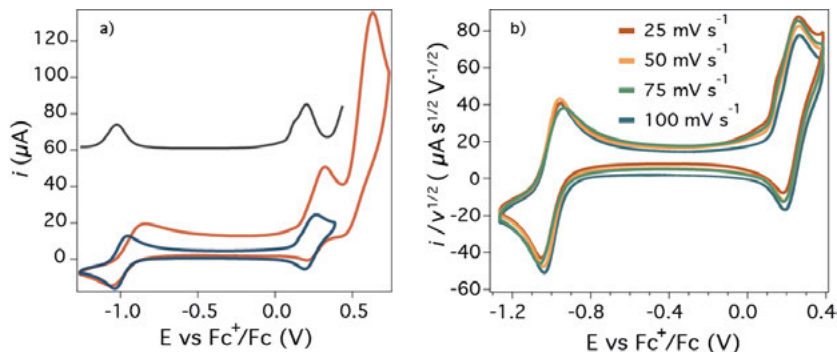


Figure 3.3. a) Cyclic voltammogram at 100 mV s^{-1} and differential pulse voltammogram (DPV, black) of 1 mM of 10^{2-} in MeCN containing 0.1 M TBAPF₆. b) Cyclic voltammograms of 10^{2-} at different scan rates (right).

In the reverse scan the peak associated with chemically reversible reduction of 9^{3-} to 9^{4-} has disappeared and is replaced by a broad wave at somewhat more positive potential (Figure 3.4b). In the second scan, the first reversible wave shifted to -0.94 V (vs. Fc^+/Fc) and the peak-to-peak separation broadened to 150 mV , while the second wave shifted to 0.11 V (vs. Fc^+/Fc) and its intensity is further increased. Concomitantly, the first redox process loses its proportionality of the current to $v^{1/2}$ within the scan rate range studied. This behavior suggests that the electron transfer occurs not exclusively from a freely diffusive species but possibly from a similar species that is adsorbed on the electrode surface (Figure 3.4c).

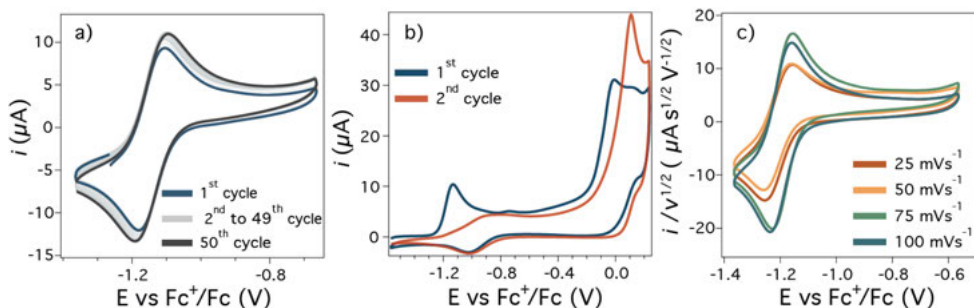


Figure 3.4. Voltammograms of 1 mM of a) 9 in MeCN containing 0.1 M TABPF₆. 50 consecutive scans of the first redox event. b) First two cycles when the potential window is extended to higher potentials. c) Different scan rates reported as $i/v^{1/2}$ vs. E .

It was noted that different batches of **10**²⁻ gave different CV responses in acetonitrile (Figure 3.5a). It shows that **10**²⁻ is easily hydrolyzed, either in the synthesis and workup or in preparing the electrochemical experiment. In such a case, the first scan waves at -1.19 and -1.00 V (vs. Fc⁺/Fc) correspond to one-electron oxidations of **9**⁴⁻ and **10**²⁻. When the **9**⁴⁻/**10**²⁻ mixture is scanned to higher potentials, a second irreversible wave at $E_p = 0.03$ V (vs. Fc⁺/Fc) is found. In subsequent scans, the $E_{1/2} = -1.19$ V (vs. Fc⁺/Fc) wave of **9**⁴⁻ is lost, as seen for pure **9**⁴⁻ (Figure 3.4b).

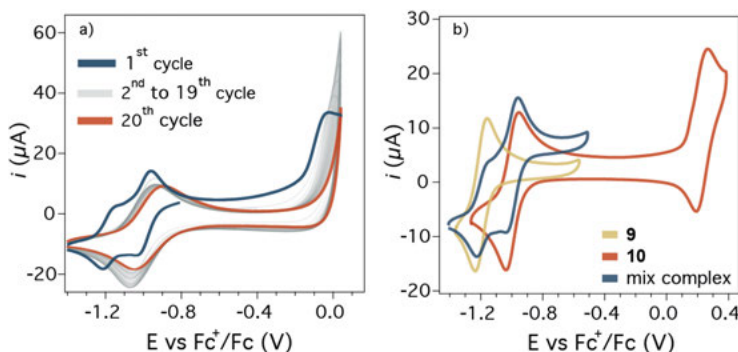


Figure 3.5. a) Voltammograms of 1 mM of a different batch of **10** during 20 scans, 0.1 M TABPF₆ in MeCN. b) Comparison of the CV of **9**, **10** and **9/10** mixture.

Given the high sensitivity of **10**²⁻ to hydrolysis, we rationalized that studying this complex for water oxidation at different pH would be hampered by the partial and possibly changing degree of conversion to **9**⁴⁻ during the experiments. Hence, investigations on water oxidation were focused on the behavior of **9**⁴⁻.

CV analysis of aqueous solutions of **9**⁴⁻ reveals a reversible Cu^{II/III} oxidation wave with $E_{1/2} = 0.38$ V (vs. NHE) and an irreversible wave with $E_p = 1.18$ V (vs. NHE) in a pH 7.5 phosphate buffer electrolyte. The latter process was assigned to the catalytic water oxidation reaction (Figure 3.6a). We compared the electrochemical response of **9**⁴⁻ with that of **5**²⁻ under the same conditions and observed that **5**²⁻ displays the Cu^{II/III} couple at $E_{1/2} = 0.29$ V (vs. NHE) and thus at milder potential by 90 mV. The top of the catalytic wave in the CV of **5**²⁻ can be observed at the same potential at $E_p = 1.26$ V (vs. NHE). Remarkably, the onset of the electrocatalytic water oxidation by **5**²⁻ emerges at approximately 150 mV lower potential than that of **9**⁴⁻, consistent with the introduction of electron-withdrawing groups in the ligand framework of the latter complex. The copper-based redox processes of **5**²⁻ and **9**⁴⁻ take place at 270 mV and 180 mV lower potential, respectively, than the previously studied acyclic tetra-amidate copper catalyst^[8]. This previous catalyst presented a tetra-anionic coordination sphere based

on a $N_1N_1'-(1,2\text{-phenylene})\text{bis}(N_2\text{-methyloxalamide})$ but lacked the macrocyclic effect, which can stabilize energetically and structurally, the Cu^{III} species more effectively as for the case of 5^{2-} and 9^{4-} . The macrocycle is again responsible for enhanced thermodynamic stability even in the presence of electron-withdrawing groups as carboxylates.

The redox properties of 9^{4-} were evaluated in the pH range between 6.5 to 11.5 (Figure 3.6b). Qualitatively, it can be observed that the catalytic peak current progressively increases with pH, as expected by an increase in the substrate concentration (OH^-). The metal-based redox reaction maintains its chemical reversibility along with the pH range, but the more it moves away from pH 8.5, the broader and more electrochemically irreversible it gets, partially explained by the slow electron transfer of the boron-doped diamond (BDD) electrode employed (but not the pH relationship). Differential pulse voltammetry (DPV) analysis was used to assess any variations in the thermodynamic potentials of 9^{4-} (Figure 3.6c). Both the $\text{Cu}^{\text{III/II}}$ redox wave and the catalytic process potentials are not significantly affected by the pH; instead, we found that just below neutral pH at 6.5, a new signal arises at $E_{1/2} = 0.13\text{ V}$ (vs. NHE).

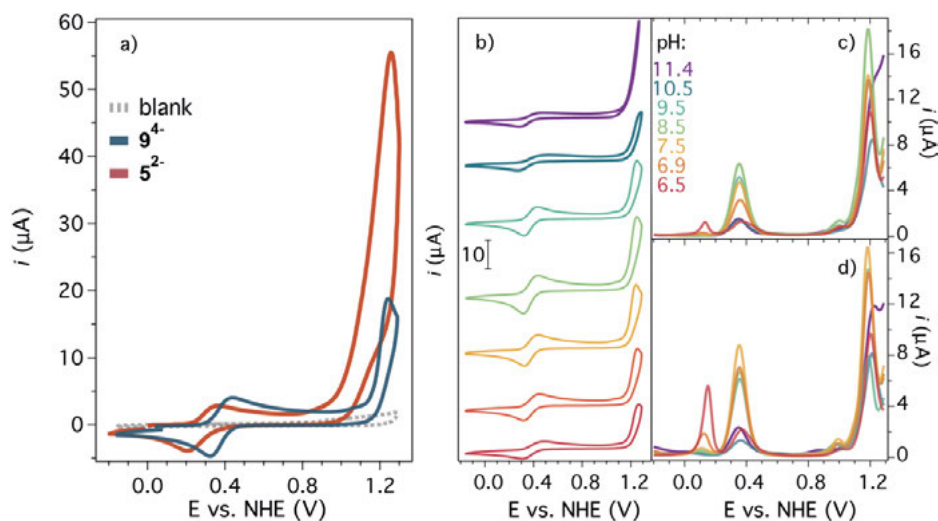


Figure 3.6. a) Voltammogram of 1 mM of 9^{4-} and 5^{2-} in buffer phosphate, pH 7.5, $I = 0.1\text{ M}$, $\nu = 100\text{ mV s}^{-1}$; boron-doped diamond (BDD) working electrode. b) pH-dependent electrochemical evaluation of 1 mM 9^{4-} in buffer phosphate, $I = 0.1\text{ M}$ by CV, $\nu = 100\text{ mV s}^{-1}$, and c) by DPV using a BDD working electrode or d) a GC working electrode. Buffer phosphate, $I = 0.1\text{ M}$, Pt disk counter electrode, and Hg/HgSO_4 reference electrode.

When we study the same system but employ a glassy carbon (GC) electrode (Figure 3.6d), the emerging wave is noticeable already at higher pH, and its intensity is increased. The magnitude of the peak was constantly growing with the number of scans in a CV experiment.

Thus, we assigned this process to the oxidation of the absorbed molecular catalyst onto the electrode surface. The lower degree of adsorption by the BDD material was also reported for **5**²⁻ elsewhere^[7]. The fact that the signal is higher for the CG electrode than for the BDD electrode indicates that binding is more robust to the graphitic material, which glassy carbon is made of than to diamond.

The UV-vis spectra of aqueous solutions of **9**⁴⁺ at different pH are illustrated in Figure 3.7a. Given the molar extinction coefficients, we ascribe the 339 and 385 nm bands to be ligand to metal charge transfer (LMCT) and *d-d* transitions, and the peak at 292 nm to a $\pi \rightarrow \pi^*$ transition of the conjugated ligand framework. Since these optical features are suppressed by the decrease in pH, it is possible that the observed acid-base equilibrium is not caused by the carboxylate groups but by the amidates that coordinate the copper center. The LMCT would be affected by amidate protonation, and the conjugation between the two phenyl amidate would be disrupted. The pK_a of the proton transfer is extracted from the most substantial changes in OD over the pH units. A sigmoid model is used to fit the data, and its inflection point reveals an averaged $pK_a = 6.28$ (Figure 3.7b).

Surprisingly, the entire absorption spectrum was fully recovered when the pH was raised from the lowest value of 4.1 back to 10.6 (Figure 3.7; left; red dotted line). This behavior demonstrates remarkable pH stability of the complex towards de-coordination of the ligand from the Cu center upon protonation. This finding further supports the effectiveness of the macrocyclic ligand framework in **9**⁴⁺, which contrasts the situation in the corresponding acyclic copper complex that undergoes demetallation upon exposure to pH below 10.5^[3,4].

The one-electron oxidation of **9**⁴⁺ ($E_{1/2} = 0.38$ V vs. NHE) and its catalytic behavior were analyzed at neutral pH by spectro-electrochemical measurements to gain insight into the nature and chemical stability of the formed species (Figure 3.8). We used an optically transparent thin-layer electrochemical (OTTLE) cell with a high surface area working electrode to ensure that the whole catalyst is transformed during a slow potential sweep. Firstly, the spectroscopic features were examined by scanning the potential between -0.2 V and 0.8 V (vs. pseudo-Ag) (Figure 3.8a). When oxidized to **9**³⁺, the LMCT band at 339 nm fades away, leaving a gradual onset for the $\pi \rightarrow \pi^*$ transition, slightly blue-shifting to 282 nm. Simultaneously, a new band arises at 253 nm. These two observations suggest that the ligand orbital might partially lower its π -donor character, but the majority of the oxidative charge is accommodated at the metal site.

The ^1H -NMR spectrum of the chemically generated $\mathbf{9}^{3-}$, in both D_2O and $\text{MeOH-}d_4$ (Figure 3.9b), visibly shows the diamagnetic nature of the oxidized complex, proving the first oxidation process to exhibit a metal character. On the contrary, $\mathbf{5}^-$ (Figure 3.9a) exhibits unusual behavior, as it produces a silent ^1H -NMR signal in D_2O , while in $\text{MeOH-}d_4$, it shows the expected proton signals. The atypical response of $\mathbf{5}^-$ was reported previously and supported by computational method [7]. The correct clarification for this behavior is not entirely clear to us; however, we can conclude that this family of copper tetra-anionic amidate complexes seems to have metal and ligand frontier orbitals that are energetically similar or even similarly degenerated. Thus, changes in the electronic structure or different solvation may impact the ligand and/or metal spin state upon oxidation.

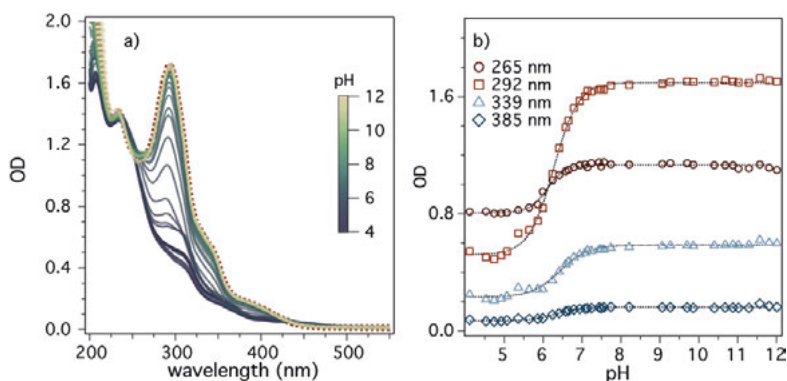


Figure 3.7 a) UV-vis spectra of $\mathbf{9}^{4-}$ during titration from pH 12.01 to 4.11. The characteristic spectrum is wholly recovered when the pH is returned to 10.6 (red dotted line) from pH 4.11. b) Sigmoids and related fitted curves of absorbance versus pH at 265, 292, 339, and 385 nm, respectively.

Another important observation for the spectro-electrochemical analysis is clear isosbestic points in the UV-vis spectral changes upon transformation of $\mathbf{9}^{4-}$ to $\mathbf{9}^{3-}$. These features indicate that only two species are involved in the transformation, and no side reactions or decomposition occurs within the time scale of the experiment. Further evidence for the stability of the redox couple is the complete spectral recovery when $\mathbf{9}^{3-}$ is reduced back to the initial species (Figure 3.8a).

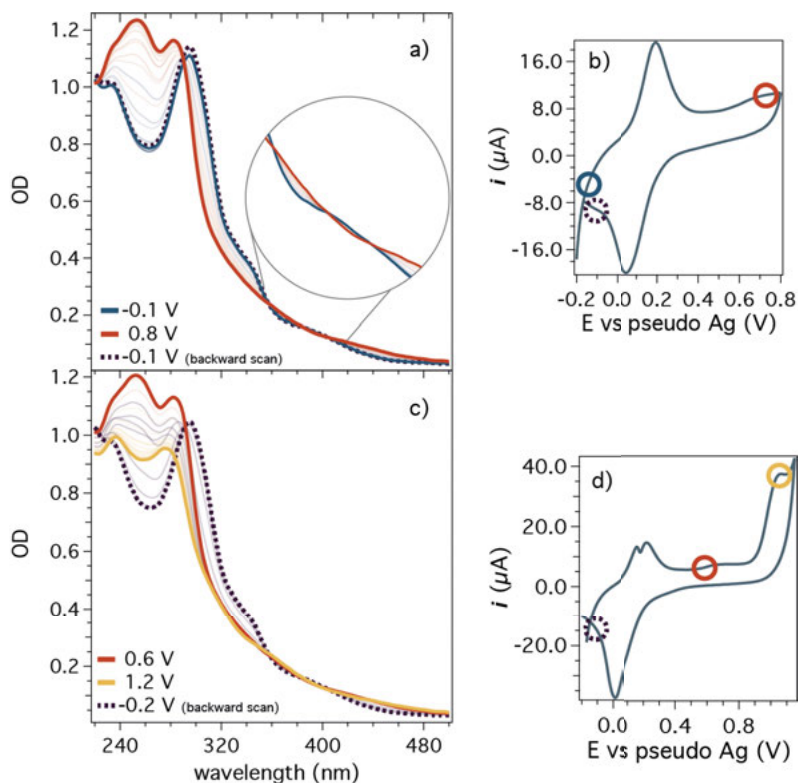


Figure 3.8. Spectro-electrochemical measurement of 2 mM solution of 9^{4-} at pH 7.5 using an OTTLE cell. a) UV-vis spectra during the b) cyclic voltammetry between -0.2 to 0.8 V. c) UV-vis spectra during the d) cyclic voltammetry between -0.2 to 1.2 V. CVs recorded at 2.5 mV s^{-1} , Pt mesh as working electrode, Pt wire as counter, and silver pseudo reference electrode.

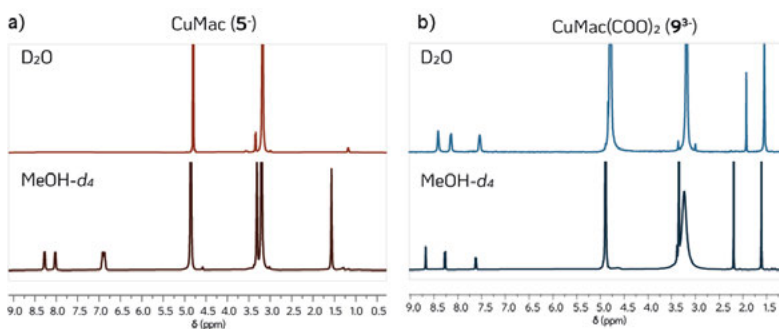


Figure 3.9. ^1H -NMR spectra of a chemically produced a) 5^- and b) 9^{3-} (right) in deuterated water and methanol. Oxidation is achieved by I_2 (0.55 eq.) in methanolic solution.

When the potential was increased to the region where catalysis occurs, the UV-vis features experienced a decrease in intensity with a slight blue shift, but overall, they retain the bands already observed for $\mathbf{9}^{3-}$ (Figure 3.8c). Thus, during the catalytic cycle, it is reasonable to assume that the vast majority of the molar fraction is represented by $\mathbf{9}^{3-}$. For this reason, we propose that the electron transfer from $\mathbf{9}^{3-}$ to $\mathbf{9}^{2-}$ be the rate-determining step of the catalytic cycle. Once again, the absorption spectrum of $\mathbf{9}^{4-}$ is completely recovered during the reverse scan, supporting the system's structural integrity and chemical stability.

3.2.3 Catalyst stability and evaluation of water oxidation reaction

The stability of $\mathbf{9}^{4-}$ under catalytic operational conditions was assessed by controlled potential electrolysis (CPE). CPE was conducted in an H-cell, with one compartment containing a 1 mM solution of $\mathbf{9}^{4-}$, while the other contained electrolyte solution. To ensure that the bulk of the solution was involved in the redox processes, a large surface area BDD plate was used as the working electrode in the anode compartment, with a Pt mesh as the cathode. In addition, both compartments were continuously stirred to guarantee a high mass transport and replenishing of the active species at the electrode-electrolyte interface (Figure 3.10a). 1.22 V (vs. NHE) was applied for the electrolysis duration. The recorded current undergoes a steep decay for the initial four hours, after which it stabilizes at about 6 μA . The current decline can be rationalized by the catalyst adsorption onto the electrode, forming a mono- or multi-layer, thus creating a non-conductive surface that provokes the isolation of the electrode's surface from the electrolyte. Therefore, the catalysis is inhibited. To evaluate the integrity of $\mathbf{9}^{4-}$, a CV of the anolyte solution was taken before the CPE and compared to a CV recorded after 12 hours of electrolysis (Figure 3.10b). The CVs show that an identical amount of complex is present in the solution before and after CPE, highlighting that negligible catalyst decomposition occurred. It is noted that the decrease in catalytic current response during CPE is not connected to the decomposition of $\mathbf{9}^{4-}$, but indeed to the electrode passivation. When a high surface area GC electrode was used in the electrolysis experiment instead, the CV after the experiment showed reduced peak intensities for all the redox processes, pointing out that $\mathbf{9}^{4-}$ is lost from the anolyte solution due to graphitic adsorption, as discussed earlier. However, the charge transferred throughout the CPE is low relative to the amount of catalyst employed, leading to low performance.

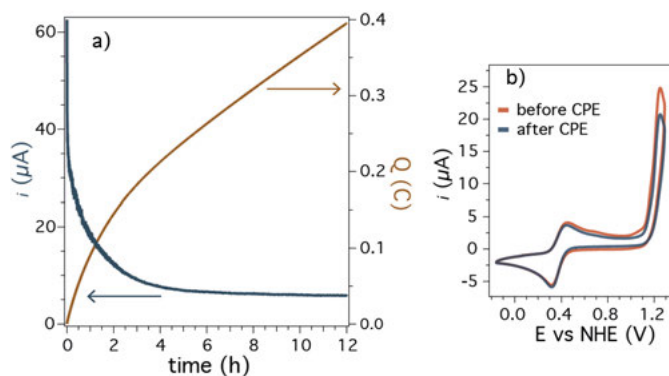


Figure 3.10. a) CPE of 9^{4-} conducted at 1.22 V for 12 h. BDD plate as working electrode, Pt mesh as counter electrode, and Hg/HgSO₄ reference. b) CVs of 9^{4-} before and after 12 h electrolysis, scan rate 100 mV s⁻¹. BDD disk as working electrode, Pt disk as counter electrode, and Hg/HgSO₄ reference. Buffer phosphate / = 0.1 M pH 7.5.

To extract kinetic information, the foot of the wave analysis (FOWA) was performed on 9^{4-} and then compared to that of 5^{2-} (Figure 3.11a, b). Linear sweep voltammetry of equimolar solutions of 9^{4-} and 5^{2-} were recorded at pH 7.5, and a portion of the potential window around the onset of the catalytic waves was used for the analysis (Figure 3.11; insets). The mathematical model, firstly introduced by Savéant *et al.* [18], was then extended to the multi-electronic water oxidation process for transition metal complexes by Llobet *et al.* [19]. The equation model refers to the water nucleophilic attack (WNA) mechanism as the rate-determining step is first order in WOC, which was demonstrated for 5^{2-} [7]. The obtained rate constants for the comprehensive catalytic cycle are $k_{\text{obs}} = 131 \text{ s}^{-1}$ for 5^{2-} and $k_{\text{obs}} = 0.6 \text{ s}^{-1}$ for 9^{4-} .

The oxygen evolution reaction (OER) was also evaluated in a light-driven assay, using a standard [Ru(bpy)₃]²⁺ photosensitizer in the presence of the sacrificial oxidant Na₂S₂O₈. A Clark-type electrode measured the oxygen in the liquid phase within the photo-reactor (Figure 3.11c). Unfortunately, for both 5^{2-} and 9^{4-} , the detected amount of oxygen was only marginally different from that of the control experiment without any catalyst. However, by comparing OER in the same conditions, it is possible to observe how 5^{2-} is a superior catalyst and more active towards oxygen generation if compared to 9^{4-} . Clearly, the carboxylate functionalities play a fundamental role in deactivating the water oxidation activity. They most likely withdraw electron density from the phenyl-amidates, which is detrimental to the four-electron process involved in water oxidation.

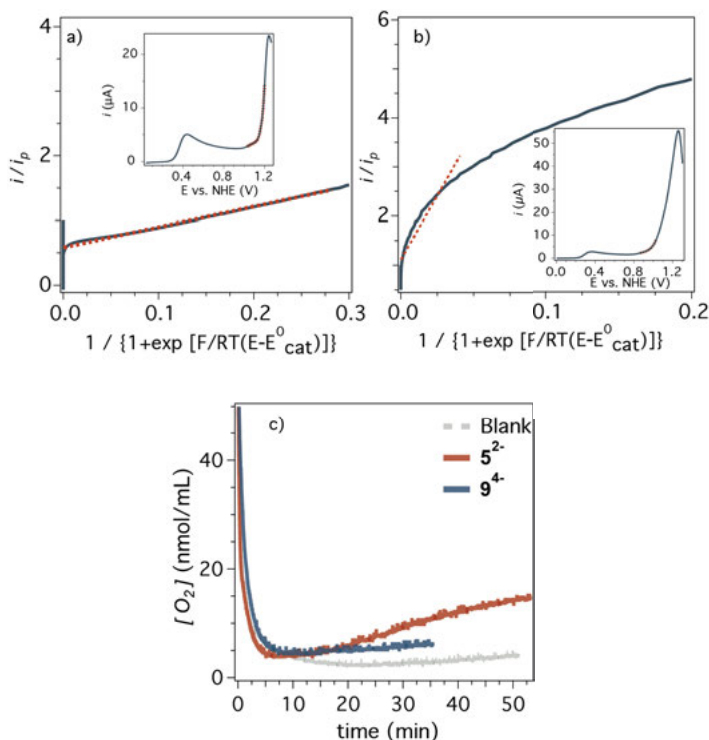


Figure 3.11. Foot of the wave analysis (FOWA) of 1 mM solutions of a) 9^{4-} and b) 5^{2-} . Insets show the linear sweep voltammetry of the corresponding catalyst, recorded at 100 mV s^{-1} and pH 7.5 using a BDD working electrode. In red is represented the linear fit related to the potential window displayed in the insets. c) Photoinduced oxygen measurements of $50 \text{ }\mu\text{M}$ of both 9^{4-} and 5^{2-} in the liquid phase by Clark electrode employing the photo-catalytic sacrificial system $[\text{Ru}(\text{bpy})_3]^{2+}/\text{Na}_2\text{S}_2\text{O}_8$. Borate buffer pH 9, $0.2 \text{ mM } [\text{Ru}(\text{bpy})_3]^{2+}$, $2 \text{ mM Na}_2\text{S}_2\text{O}_8$, $h\nu > 400 \text{ nm}$, 1 sun .

3.3 CONCLUSION

In this chapter, we explored the possibility of functionalizing the previously reported Cu-based WOC, 5^{2-} , with carboxylic acid groups, 9^{4-} . The modification was motivated by prospects to heterogenize the complex onto solid-state electrodes or metal-organic frameworks (MOFs). A first electrochemical analysis revealed an increase in the potential for the $\text{Cu}^{\text{III/II}}$ couple and the overpotential required for catalysis. Both effects are consistent with the electron-withdrawing character of the ligand scaffold with $-\text{COO}$ groups.

However, spectroscopic analysis proved the modified catalyst's robustness during the redox reactions, suggesting that oxidations are entirely reversible and that the complexes remain structurally intact. The pH stability was assessed in detail for **9⁴⁻**, establishing once again the ability of the macrocyclic ligand to stabilize the metal center. The macrocyclic nature of the ligand prevents ligand displacement even when the amidates are being protonated. This feature makes the TAML ideal ligand frameworks for first-row metal complex catalysts, as they are known to be more labile than the respective second-row complexes.

Despite the catalyst's ruggedness, the introduction of carboxylic moieties was found to be kinetically detrimental to the activity towards water oxidation, making the new material an inferior catalyst compared to **5²⁻**, where no functional groups are connected to the ligand backbone.

3.4 EXPERIMENTAL DETAILS

Materials: Solvents and chemicals were purchased by Sigma-Aldrich or Abcr GmbH and used without further purification. Aqueous basic buffer solutions at several pH values were prepared using specific concentrations of monobasic, dibasic, and tribasic phosphate salts such that the final ionic strength was 0.1 M. High-purity deionized water was obtained by filtering distilled water through a nanopore Milli-Q water purification system.

Characterization techniques: Elemental analysis of the samples was conducted in a Thermo Finnigan elemental analyzer Flash 1112 model.

Mass spectrometry was measured in electrospray mode with an LCT Premier mass spectrometer (TOF analyzer, Micromass-Waters) in methanol by direct injection.

A 400 MHz Bruker Advance II and a 500 MHz Bruker Advance were used to measure ¹H and ¹³C NMR spectra. All measurements were done at room temperature in deuterated DMSO-*d*₆, D₂O and MeOH-*d*₄.

UV-vis spectra were obtained using a Cary 50 (Varian) UV-vis spectrophotometer with 10 mm and 2 mm quartz cuvettes in buffer solution (pH 11.5 or 7.5, phosphate buffer 0.1 M of ionic strength).

Electrochemical characterization: Buffer solutions were prepared as follows: pH = 7.5 buffered solution (*I* = 0.1 M): NaH₂PO₄ (0.0073 mol) and Na₂HPO₄ (0.0306 mol) were dissolved in milliQ H₂O to make up 1 L of solution. pH = 11.5 buffered solution (*I* = 0.1 M): Na₂HPO₄ (0.0186 mol) and Na₃PO₄ (0.0073 mol) were dissolved in 1 L milliQ H₂O.

Cyclic voltammetry and differential pulse voltammetry experiments were measured by JJ-Cambria CHI-660 potentiostat. Solutions of the complexes were placed in one-compartment three-electrode cells. Glassy carbon (GC) or boron-doped diamond (BDD) disk electrodes (3 mm of diameter in both cases) were used as working electrodes, Hg/HgSO₄ (K₂SO₄ sat) or Ag/AgCl (KCl 3M) as reference electrode and Pt disk as a counter electrode. For analysis in organic media,

Ag/AgNO₃ (10 mM) reference electrode was employed and referred to the ferrocene/ferrocenium (Fc/Fc⁺) couple.

Working electrode pre-treatment before each measurement consisted of polishing with 0.05 μ m alumina paste, rinsing with water and acetone, and blow-dried. All redox potentials in aqueous media are reported versus NHE by adding 0.64 V or 0.21 V to the measured potential, respectively, for Hg/HgSO₄ and Ag/AgCl (KCl 3M) reference electrode.

DPV were obtained with the following parameters: amplitude= 50 mV, step height=4 mV, pulse width= 0.05 s, pulse period= 0.5 s and sampling width= 0.0167 s. $E_{1/2}$ values for the redox processes studied in this work are estimated according to the potential at the I_{\max} in DPV measurements. Both measurements were done by applying IR compensation when organic solvent was used, as acetonitrile, of 0.1 M as supporting electrolyte.

Spectroelectrochemical study was carried out in an optically transparent thin-layer electrochemical (OTTLE) cell (OMNI-CELL SPECAC, by Prof. Frantisek Hartl's group, University of Reading). This cell contains two Pt grid electrodes (working and counter) and a silver wire pseudo reference electrode (-0.2 V vs. NHE). This cell is filled with less than 0.3 mL of a 2 mM catalyst solution in phosphate buffer at pH 7.5 (0.1 M of ionic strength), avoiding gas bubbles formation within the thin layer. The optical path length is about 0.2 mm.

The OTTLE cell was placed in a Cary 50 (Varian) UV-vis spectrophotometer, and the electrodes were connected to an IJ-Cambria CHI-660 potentiostat. Then, cyclic voltammetry was performed at 2.5 mV s⁻¹ and UV-vis spectra were recorded continuously to monitor the changes in the electronic structure.

Controlled potential electrolysis (CPE) experiments were performed at different potentials to catalyze the water oxidation by the reported catalysts using a two-compartment cell, separated by a sintered glass filter disk (aceglass®, Porosity D) and closed with a septum. As working electrodes, large surface glassy carbon rod and BDD plate (2.5 cm² surface) electrodes were used with an Ag/AgCl (KCl sat) as reference electrode. These were placed in one of the compartments filled with a 1 mM, 0.5 mM, or 0.1 mM solution of the catalyst (pH 7.5/10.2 phosphate buffer 0.1 M of ionic strength). A mesh platinum counter electrode was used in the other compartment containing only the buffer solution.

The photoinduced water oxidation experiments were performed in a DW2/2 chamber (Hansatech Instruments, Inc) with an integrated Clark-type polarographic oxygen electrode (Hansatech Instruments, Inc) that could measure the produced oxygen in the liquid phase (no headspace is left in this kind of experiment). Before each experiment, the oxygen sensor was calibrated with the whole air- and nitrogen-saturated solution. In a typical experiment, 2 mL of a mixture containing Na₂S₂O₈ (2 mM), [Ru(bpy)₃]²⁺ (200 μ M), and copper complex in pH = 9 solution was introduced into the dark chamber, thermostated at 25 °C. The solution was stirred and degassed, and the chamber was finally closed with a screw cap equipped with a septum. After the calibration and baseline collection, the solution was irradiated by opening the chamber's windows. The illumination was provided by a 150 W Xenon Arc Lamp (LS-150, ABET technology), equipped with a 400 nm cut-off filter, and calibrated to 1 sun (100 mW cm⁻²) by using a calibrated silicon photodiode.

*Synthetic details***1**

A dry two-neck round bottom flask was charged with *o*-phenylene diamine (3000.0 mg, 27.70 mmol) and trimethylamine (2.50 mL, 27.60 mmol) under N₂. Dry THF (150 mL) was added to the flask. Di-*tert*-butyl dicarbonate 2 M in THF (13.8 mL, 27.60 mmol) was added dropwise to the reaction by a syringe pump at 0 °C at a flow rate of 0.46 mL min⁻¹. The reaction mixture was stirred at room temperature for 6 h while maintaining an inert atmosphere. The solvent was evaporated, and the solid was purified by flash column chromatography. Silica was employed as the stationary phase, and a mixture of hexane: ethyl acetate as the mobile phase (95:5 with a gradient to 8:2).

Yield: 4380.2 mg; 21.05 mmol; 76 % (69 ± 7)

¹H NMR (400 MHz, DMSO-*d*₆) δ: 8.24 (s, 1H), 7.13 (d, *J* = 7.9 Hz, 1H), 6.79 (t, *J* = 7.6 Hz, 1H), 6.64 (d, *J* = 7.9 Hz, 1H), 6.48 (t, *J* = 7.6 Hz, 1H), 4.77 (s, 2H), 1.42 (s, 9H).

3

A flask was charged with *tert*-butyl (2-aminophenyl)carbamate (**1**) under N₂. Anhydrous THF (150 mL) and pyridine (3.73 mL, 46.31 mmol) were added. Dimethylmalonyl dichloride (1.39 mL, 10.52 mmol) in anhydrous THF (10 mL) was added by syringe pump to the reaction flask at a rate of ca. 1 drop s⁻¹, and the mixture was stirred overnight. A white precipitate of pyridinium chloride formed. The reaction mixture was evaporated, and the crude product (**2**) was used without further purification.

Di-*tert*-butyl (((2,2-dimethylmalonyl)bis(azanediyl))bis(2,1-phenylene))dicarbamate (**2**) was dissolved in rapidly stirred EtOAc (140 mL) and conc. HCl (13 mL) was added dropwise to give a biphasic reaction mixture (ca. 2.5 M HCl in the volume of the biphasic mixture). After 2 h of stirring, distilled water was added, and the acid was neutralized with an excess of K₂CO₃ until pH 8 was reached. The suspension formed upon neutralization was filtered off, washed with abundant H₂O, and rinsed sparingly with Et₂O. The white solid is collected and made well-dried.

Yield (two steps): 3029.7 mg; 9.70 mmol; 92 % (85 ± 5 %)

¹H NMR (400 MHz, DMSO-*d*₆) δ: 8.96 (d, *J* = 2.1 Hz, 2H), 6.92 (dd, *J* = 7.6, 2.1 Hz, 4H), 6.72 – 6.63 (m, 2H), 6.50 (d, *J* = 1.2 Hz, 2H), 4.84 (s, 4H), 1.52 (d, *J* = 2.1 Hz, 6H).

4

*N*¹,*N*³-bis(2-aminophenyl)-2,2-dimethylmalonamide (**3**) (800.3 mg; 2.56 mmol) was added to anhydrous THF (320 mL) with trimethylamine (0.75 mL; 5.38 mmol) in a dried two-neck round bottom flask under nitrogen. Oxalyl dichloride 2 M in THF (1.41 mL, 2.82 mmol) was added slowly by syringe pump to the reaction vessel at a rate of 10 mL h⁻¹. A white precipitate formed. The reaction was stirred for 48 h. The solid was filtered off, the remaining mixture was evaporated, resulting in a wet, white-yellowish solid, and the latter was sonicated in Et₂O filtered and washed with H₂O affording a white chalky solid.

Yield: 827.5 mg; 2.25 mmol; 88 % (68 ± 20 %)

3.

^1H NMR (400 MHz, DMSO- d_6) δ : 9.65 (s, 2H), 9.55 (s, 2H), 7.62 (dd, J = 7.7, 1.9 Hz, 2H), 7.42 – 7.23 (m, 6H), 1.55 (s, 6H).

^{13}C NMR (101 MHz, DMSO- d_6) δ 173.00, 162.33, 132.13, 131.24, 127.68, 126.98, 126.55, 125.94, 51.67, 23.77.

(NMe₄)₂[CuMac]

The macrocyclic ligand precursor (**4**) (408.3 mg, 1.114 mmol) was dispersed in 2 mL of MeOH using a sonicator for 5 min. Afterward, a tetramethylammonium hydroxide (25% in MeOH, 1.87 mL, 4.458 mmol) was added, and the dispersion was solubilized. At that moment, a copper perchlorate hexahydrate (412.8 mg, 1.114 mmol) solution in MeOH (15 mL) was prepared and added to the mixture via a syringe pump overnight. After ca. 12 hours, the solvent was evaporated, and the least amount of dry EtOH (over 4A molecular sieves) was added to the mixture. The solid formed was removed by filtration through 0.2 μm PTFE filters, and the solvent was concentrated. Crystallization from dry MeOH/Et₂O by slow diffusion afforded the desired brown/red (NMe₄)₂[CuMac] complex.

Yield: 632.5 mg; 1.101 mmol; 99 % (88 ± 11 %)

MALDI/TOF MS (negative mode) m/z : exp. 425.1 (CuMac+H)⁻; ([C₁₉H₁₄CuN₄O]) cal. m/z : 425.0).

6

Ethyl 3,4-diaminobenzoate (1181.7 mg, 10.45 mmol) and trimethylamine (0.93 mL, 10.45 mmol) were poured into a dry two neck-round bottom flask under N₂ and were dissolved in dry THF (150 mL). Di-*tert*-butyl dicarbonate 2M in THF (5.2 mL, 10.45 mmol) was added to the reaction mixture slowly and dropwise by a syringe pump at 0°C at a rate of 2.5 mL h⁻¹. Once the addition was completed, the mixture was left stirring at room temperature for 6 h. Then the solvent was evaporated, and the solid was purified by flash column chromatography. Silica was employed as a stationary phase, and a mixture of hexane: ethyl acetate as the mobile phase (95:5 with a gradient to 8:2).

Yield: 2131.2 mg; 7.60 mmol; 73 % (66 ± 4 %)

^1H NMR (400 MHz, DMSO- d_6) δ : 8.34 (s, 2H), 7.87 (d, J = 2.0 Hz, 2H), 7.47 (dd, J = 8.4, 2.0 Hz, 2H), 6.70 (d, J = 8.4 Hz, 2H), 5.70 (s, 4H), 4.22 (q, J = 7.1 Hz, 4H), 1.47 (s, 19H), 1.28 (t, J = 7.1 Hz, 6H).

Intermediate to **7**

Ethyl 4-amino-3-((*tert*-butoxycarbonyl)amino)benzoate (**6**) (3265 mg, 11.65 mmol) was placed into a two-neck round bottom flask under N₂. Anhydrous THF (140 mL) and pyridine (1.15 mL, 14.57 mmol) were added. Dimethylmalonyl dichloride (770 μL , 5.83 mmol) in anhydrous THF (10 mL) was added by syringe pump to the reaction flask at a rate of ca. 1 drop s⁻¹, and the mixture was stirred overnight. A white precipitate of pyridinium chloride formed. The product was obtained by evaporating the filtrate after filtration of the white pyridinium salt.

Yield: 3824.9 mg; 5.82 mmol; 99 % (94 ± 4 %)

^1H NMR (400 MHz, $\text{DMSO}-d_6$) δ : 9.53 (s, 2H), 8.08 (d, $J = 1.9$ Hz, 2H), 7.76 (d, $J = 8.5$ Hz, 2H), 7.72 (dd, $J = 8.5, 1.9$ Hz, 2H), 4.31 (q, $J = 7.1$ Hz, 4H), 1.59 (s, 6H), 1.44 (s, 18H), 1.32 (t, $J = 7.1$ Hz, 6H).

7

Diethyl 4,4'-((2,2-dimethylmalonyl)bis(azanediyl))bis(3-((*tert*-butoxycarbonyl)amino)benzoate) (2493 mg, 3.8 mmol) was dissolved in rapidly stirred EtOAc (80 mL) and conc. HCl (20 mL) was added slowly to give a biphasic reaction mixture (*ca.* 2.5 M HCl in the volume of the biphasic mixture). After 2.5 h of stirring, distilled water was added, and the acid was neutralized with an excess of K_2CO_3 . The suspension formed upon neutralization was filtered off and washed with a small amount of Et_2O . The white solid is collected and made well dried.

Yield: 1496.8; 3.28 mmol; 86 % (77 ± 10 %)

^1H NMR (400 MHz, $\text{DMSO}-d_6$) δ : 9.21 (s, 2H), 7.39 (d, $J = 1.7$ Hz, 2H), 7.23 – 7.13 (m, 4H), 5.19 (s, 4H), 4.27 (q, $J = 7.1$ Hz, 4H), 1.59 (s, 6H), 1.31 (t, $J = 7.1$ Hz, 6H).

8

Diethyl 4,4'-((2,2-dimethylmalonyl)bis(azanediyl))bis(3-aminobenzoate) (**7**) (1486.8 mg, 3.2 mmol) was added to anhydrous THF (130 mL) with trimethylamine (642 μL , 7.2 mmol) in a dried two-neck round bottom flask under nitrogen. Oxalyl dichloride 2 M in THF (1.6 mL, 3.2 mmol) was added slowly by syringe pump to the reaction vessel at a rate of 10 mL h^{-1} . A white precipitate formed. The reaction was stirred over 60 h. The solid was filtered off, the remaining mixture was evaporated, resulting in a wet, white-yellowish solid, and the latter was sonicated in Et_2O filtered and washed with MeOH affording **8** ($\text{Mac}(\text{COOEt})_2$), as a white chalky solid.

Yield: 1241 mg; 2.43 mmol; 76% (58 ± 12 %)

^1H NMR (500 MHz, $\text{DMSO}-d_6$) δ : 10.04 (s, 2H), 9.97 (s, 2H), 8.10 (d, $J = 2.0$ Hz, 2H), 7.86 (dd, $J = 8.3, 2.0$ Hz, 2H), 7.53 (d, $J = 8.3$ Hz, 2H), 4.31 (q, $J = 7.1$ Hz, 4H), 1.54 (s, 6H), 1.31 (t, $J = 7.1$ Hz, 6H).

^{13}C NMR (500 MHz, $\text{DMSO}-d_6$) δ 173.25, 165.77, 162.75, 136.57, 132.28, 128.34, 127.88, 127.69, 127.36, 61.83, 52.13, 24.27, 15.00.

Elementary analysis: $\text{Mac}(\text{COOEt})_2 \cdot \text{H}_2\text{O} \cdot \text{MeOH}$ [$\text{C}_{26}\text{H}_{32}\text{N}_4\text{O}_{10}$] cal. C 55.71%; H 5.75%; N 10.00%; exp. C 55.44%; H 5.41; N 10.37%.

ESI-MS (MeOH, DEA) (negative mode) m/z : exp. 509.1 ($\text{Mac}(\text{COOEt})_2\text{-H}$); 1019.1 ($2 \text{ Mac}(\text{COOEt})_2\text{-H}$); (positive mode) m/z : exp. 584.1 ($\text{Mac}(\text{COOEt})_2\text{+DEA+H}^+$); 1094.2 ($2 \text{ Mac}(\text{COOEt})_2\text{+DEA+H}^+$); [$\text{C}_{25}\text{H}_{26}\text{N}_4\text{O}_8$] m/z : cal. 510.1).

Ligand precursor of **9**⁴⁻

Diethyl 15,15-dimethyl-6,7,14,16-tetraoxo-6,7,8,13,14,15,16,17-octahydro-5H-dibenzo[b,h][1,4,7,10]tetraazacyclotridecine-3,10-dicarboxylate (625.8 mg, 1.23 mmol) and NaOH (600 mg, 15 mmol) in EtOH (25 mL) was stirred for 1 days at room temperature. HCl 2 M was added until $\text{pH} \approx 1$. Then EtOH was evaporated, and the mixture was filtered and washed with H_2O and Et_2O , and the solid recovered as a white powder.

Yield 445.1 mg; 0.98 mmol; 80 % (81 ± 6 %)

^1H NMR (500 MHz, $\text{DMSO}-d_6$) δ 9.92 (s, 2H), 9.82 (s, 2H), 8.05 (d, $J = 2.0$ Hz, 2H), 7.84 (dd, $J = 8.3, 2.0$ Hz, 2H), 7.51 (d, $J = 8.3$ Hz, 2H), 1.52 (s, 6H).

^{13}C NMR (126 MHz, $\text{DMSO}-d_6$) δ 173.09, 167.31, 162.89, 136.42, 132.04, 129.27, 128.19, 127.81, 127.40, 51.94, 24.39.

Elemental analysis: $\text{Mac}(\text{COOH})_2 \cdot \text{H}_2\text{O} \cdot \text{MeOH} \cdot 2\text{NaCl}$ [$\text{C}_{22}\text{H}_{24}\text{Cl}_2\text{N}_4\text{O}_{10}$] cal. C 42.53%; H 3.89%; N 9.02% exp. C 42.40% H 3.70%; N 9.05%.

ESI-MS (MeOH) (negative mode) m/z : exp. 453 ($\text{Mac}(\text{COOH})_2\text{-H}$) $^-$ and 907 (2 $\text{Mac}(\text{COOH})_2\text{-H}$) $^-$; (positive mode) m/z : exp. 455 ($\text{Mac}(\text{COOH})_2\text{+H}$) $^+$, 477 ($\text{Mac}(\text{COOH})\text{+Na}$) $^+$, 931 (2 $\text{Mac}(\text{COOH})_2\text{+Na}$) $^+$. ($[\text{C}_{21}\text{H}_{18}\text{N}_4\text{O}_8]$ m/z : cal. 454.1)

(NMe₄)₄[CuMac(COO)]₂

The precursor ligand (100.2 mg, 0.22 mmol) was dispersed in MeOH (8 mL). The suspension was brought to 50 °C, and a tetramethylammonium hydroxide 10 % in MeOH (1.39 mL, 1.32 mmol) was added dropwise. Later a fresh copper perchlorate hexahydrate (81.5 mg, 0.22 mmol) solution in MeOH (4 mL) was prepared and added to the mixture slowly by a syringe pump (1 h), and the latter was left stirring overnight at room temperature. After that, MeOH was evaporated, and absolute EtOH (ca. 1 mL) was added. Then the solution was filtered to remove the inorganic salt formed during the complexation step. The remaining solution was treated with abundant ether, which caused a brown-reddish solid to precipitate. The product is highly hygroscopic, and the water that quickly is absorbed was removed at the oil pump, heating the sample at 45 °C.

Yield: 139.6 mg; 0.1724mmol; 78 % (58 ± 20 %)

Elemental analysis: $(\text{NMe}_4)_4[\text{CuMac}(\text{COO})_2] \cdot \text{H}_2\text{O} \cdot \text{EtOH} \cdot 2(\text{NMe}_4\text{ClO}_4)$ [$\text{C}_{47}\text{H}_{92}\text{Cl}_2\text{CuN}_{10}\text{O}_{18}$] cal. C 45.93%; N 11.76%; H 7.71%; exp. C 46.26%, N 11.78%, H 8.34%. Small impurities or the deliquescent nature of the compound might affect the result of the analysis.

ESI-MS (MeOH) (negative mode) m/z : exp. 512.8; 587 ($\text{CuMac}(\text{COO})_2\text{+H}_2$) $^{2-}$ (NMe_4) $^+$; ($[\text{C}_{21}\text{H}_{12}\text{CuN}_4\text{O}_8]$ m/z : cal. 510.8)

(NMe₄)₂[CuMac(COOEt)]₂

The ligand precursor **8** (50.5 mg, 0.098 mmol) was dispersed in MeOH (2 mL) using a sonicator for 15 min. The mixture was brought to 70 °C, tetramethylammonium hydroxide (10 % in MeOH, 413 μL , 0.39 mmol) was added, and the dispersion was solubilized. At that moment, a copper perchlorate hexahydrate (36.3 mg, 0.098 mmol) solution in MeOH (4 mL) is prepared and added to the mixture dropwise and slowly. After 1 h, a solid was formed, removed by filtration, and the solvent was concentrated to about 1 mL solution. The remaining solution was treated with abundant ether, which caused a brown-reddish solid to precipitate, the solvent was removed, and the remaining oil was dried over vacuum and heated at 50 °C.

Yield: 25.9 mg; 0.036 mmol; 37%

Elemental analysis: $(\text{NMe}_4)_2[\text{CuMac}(\text{COOEt})_2] \cdot 9 \text{H}_2\text{O}$ [$\text{C}_{33}\text{H}_{64}\text{CuN}_6\text{O}_{17}$] cal. C 45.02 %; N 9.55%; H 7.33% exp. C 44.57 %; N 9.71%; H 6.51%.

ESI-MS (MeOH) (negative mode) m/z : exp. 284.6 ($\text{CuMac}(\text{COOEt})_2$) $^{2-}$; 570.0 ($\text{CuMac}(\text{COOEt})_2\text{+H}$) $^-$ 643.0 ($\text{CuMac}(\text{COOEt})_2$) $^{2-}$ (NMe_4) $^+$; ($[\text{C}_{25}\text{H}_{22}\text{CuN}_4\text{O}_8]$ m/z : cal. 569.0)

3.5 REFERENCES

- [1] S. M. Barnett, K. I. Goldberg, J. M. Mayer, *Nat. Chem.* **2012**, 4, 6, 498–502.
- [2] N. D. Schley, J. D. Blakemore, N. K. Subbaiyan, C. D. Incarvito, F. Dsouza, R. H. Crabtree, G. W. Brudvig, *J. Am. Chem. Soc.* **2011**, 133, 27, 10473–10481.
- [3] P. Garrido-Barros, I. Funes-Ardoiz, S. Drouet, J. Benet-Buchholz, F. Maseras, A. Llobet, *J. Am. Chem. Soc.* **2015**, 137, 6758–6761.
- [4] P. Garrido-Barros, C. Gimbert-Surinifach, D. Moonshiram, A. Picón, P. Monge, V. S. Batista, A. Llobet, *J. Am. Chem. Soc.* **2017**, 139, 37, 12907–12910.
- [5] W. C. Ellis, N. D. McDaniel, S. Bernhard, T. J. Collins, *J. Am. Chem. Soc.* **2010**, 132, 32, 10990–10991.
- [6] W. C. Ellis, C. T. Tran, R. Roy, M. Rusten, A. Fischer, A. D. Ryabov, B. Blumberg, T. J. Collins, *J. Am. Chem. Soc.* **2010**, 132, 28, 9774–9781.
- [7] P. Garrido-Barros, D. Moonshiram, M. Gil-Sepulcre, P. Pelosin, C. Gimbert-Suriñach, J. Benet-Buchholz, A. Llobet, *J. Am. Chem. Soc.* **2020**, 142, 41, 17434–17446.
- [8] P. Garrido-Barros, I. Funes-Ardoiz, S. Drouet, J. Benet-Buchholz, F. Maseras, A. Llobet, *J. Am. Chem. Soc.* **2015**, 137, 21, 6758–6761.
- [9] I. Funes-Ardoiz, P. Garrido-Barros, A. Llobet, F. Maseras, *ACS Catal.* **2017**, 7, 3, 1712–1719.
- [10] P. Garrido-Barros, R. Matheu, C. Gimbert-Suriñach, A. Llobet, *Curr. Opin. Electrochem.* **2019**, 15, 140–147.
- [11] J. J. Concepcion, M.-K. Tsai, J. T. Muckerman, T. J. Meyer, *J. Am. Chem. Soc.* **2010**, 132, 5, 1545–1557.
- [12] X. P. Zhang, H. Y. Wang, H. Zheng, W. Zhang, R. Cao, *Chinese J. Catal.* **2021**, 42, 8, 1253–1268.
- [13] X. Sala, S. Maji, R. Bofill, J. García-Antón, L. Escriche, A. Llobet, *Acc. Chem. Res.* **2014**, 47, 2, 504–516.
- [14] A. de Aguirre, P. Garrido-Barros, I. Funes-Ardoiz, F. Maseras, *Eur. J. Inorg. Chem.* **2019**, 2019, 15, 2109–2114.
- [15] Z. Codolà, I. Garcia-Bosch, F. Acuña-Parés, I. Prat, J. M. Luis, M. Costas, J. Lloret-Fillol, *Chem. Eur. J.* **2013**, 19, 25, 8042–8047.
- [16] Y. Sato, S. Y. Takizawa, S. Murata, *Eur. J. Inorg. Chem.* **2015**, 2015, 33, 5495–5502.
- [17] D. K. Dogutan, R. McGuire, D. G. Nocera, *J. Am. Chem. Soc.* **2011**, 133, 24, 9178–9180.
- [18] C. Costentin, S. Drouet, M. Robert, J. M. Savéant, *J. Am. Chem. Soc.* **2012**, 134, 27, 11235–11242.
- [19] R. Matheu, S. Neudeck, F. Meyer, X. Sala, A. Llobet, *Chem. Sus. Chem.* **2016**, 9, 23, 3361–3369.

4

MECHANISTIC INVESTIGATION OF THE PHOTO-OXIDATION OF $[\text{CuMac}]^{2-}$

4.1 INTRODUCTION

Photoredox catalysis is a branch of chemistry that employs the intrinsic ability of photosensitizers to undergo redox reactions in the excited state to drive redox processes. Photoredox catalysts catalyze chemical reactions through single electron transfer (SET) reactions after light absorption. In its photo-excited state, the open-shell nature of the sensitizer makes it able to act as a reducing or oxidizing agent in the presence of a suitable sacrificial electron acceptor or donor molecule, respectively. The electron transfer process produces the photosensitizer in the oxidized or reduced state, which is the reactive species ^[1]. Subsequently, a reaction between the substrate and the oxidized or reduced photocatalyst oxidizes or reduces the substrate and restores the photocatalyst in the ground state. In contrast to conventional redox chemistry approaches, photocatalysts enable mild operational conditions, use low-energy UV-visible light sources at room temperature, and often avoid toxic redox reagents ^[2]. Firstly employed for organic synthesis, photoredox catalysts have widely emerged in mechanistic investigations and solar fuels conversion ^[3–7] following the seminal works of MacMillan ^[8] and Stephenson ^[9], introducing transition metal complexes as photo-absorber materials.

Tris(bipyridine)ruthenium(II) $[\text{Ru}(\text{bpy})_3]^{2+}$ has been widely studied and explored as a redox photocatalyst, and its photophysical properties are well established ^[10]. The UV-visible absorption spectrum of $[\text{Ru}(\text{bpy})_3]^{2+}$ in water shows the characteristic absorption bands at 290 nm of a ligand-based $\pi \rightarrow \pi^*$ transition and at 454 nm of a charge-transfer transition of an electron from a metal-centered d -orbital to a ligand-centered π^* -orbital to form a singlet metal-to-ligand charge transfer (¹MLCT) state (Figure 4.1). After excitation, a fast intersystem crossing (ISC) converts the ¹MLCT state with near unit quantum yield into a long-lived triplet state (³MLCT) that can participate

in bimolecular reactions. When not engaged in reactions, the $^3\text{MLCT}$ state decays radiatively ($\phi = 2\text{--}4\%$) via phosphorescence to the singlet ground state, giving rise to emission at 610 nm (Figure 4.1) [11]. The $^3\text{MLCT}$ state has a lifetime of $\sim 0.60\ \mu\text{s}$ in an oxygen-free sample. The value may be affected by the solution's ionic strength, the complex's counter anion, or by quenching by $^3\text{O}_2$ [12–14].

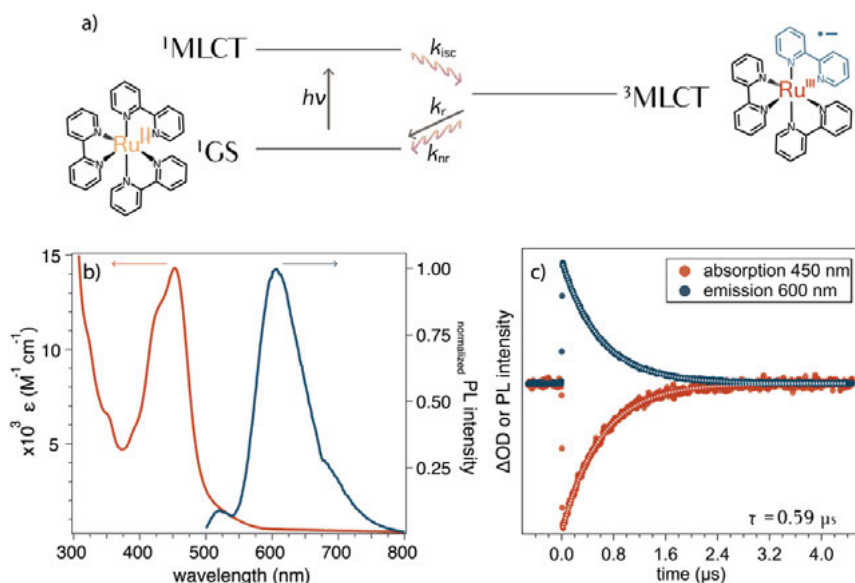


Figure 4.1. Photophysics of $[\text{Ru}(\text{bpy})_3]\text{Cl}_2$. a) Jablonski diagram showing the excitation and ISC to the $^3\text{MLCT}$ state. b) Absorption and photoluminescence spectra of $[\text{Ru}(\text{bpy})_3]\text{Cl}_2$ in deionized water. c) Decay of the $^3\text{MLCT}$ state of $[\text{Ru}(\text{bpy})_3]\text{Cl}_2$ in an aqueous solution of phosphate buffer (25 mM), measured with transient absorption and time-resolved photoluminescence.

The $^3\text{MLCT}$ state makes this chromophore a versatile tool in spectroscopy. In the presence of an electron donor quencher, the $^3\text{MLCT}$ excited state of $[\text{Ru}(\text{bpy})_3]^{2+}$ can be reduced to $[\text{Ru}(\text{bpy})_3]^+$, in which one of the bipyridine ligands takes up the electron. This reductive quenching can be made irreversible using a sacrificial donor that chemically degrades after transferring the electron, such that back-electron transfer cannot occur. The thereby produced $[\text{Ru}(\text{bpy})_3]^+$ has a long lifetime and can drive reductive redox processes ($E_{1/2} = -1.30\ \text{V}$ vs. NHE). If instead, a sacrificial electron acceptor is introduced, the $^3\text{MLCT}$ state can be oxidatively quenched, producing $[\text{Ru}(\text{bpy})_3]^{3+}$ ($E_{1/2} = 1.26\ \text{V}$ vs. NHE) and the reduced electron acceptor. In this case, $[\text{Ru}(\text{bpy})_3]^{3+}$ can be an oxidizing agent.

Here, we aim to elucidate the mechanism of the water oxidation reaction of copper complex, $[\text{CuMac}]^{2-}$, consisting of a Cu^{2+} ion and a fourfold negatively charged

tetradentate amidate macrocyclic ligand, 15,15-dimethyl-8,13-dihydro-5*H*-dibenzo[*b,h*] [1,4,7,10]tetraazacyclotridecine-6,7,14,16(15*H*,17*H*)-tetraone^[15,16] abbreviated as Mac (see Chapter 3 where $[\text{CuMac}]^{2-} = \mathbf{5}^{2-}$). Using a photoredox catalyst in combination with nanosecond pulsed excitation and time-resolved spectroscopy should allow the investigation of the water oxidation reaction. Flash-quench methods utilizing $[\text{Ru}(\text{bpy})_3]\text{Cl}_2$ and sodium persulfate ($\text{Na}_2\text{S}_2\text{O}_8$), as photosensitizer and sacrificial electron acceptor, respectively, produce $[\text{Ru}(\text{bpy})_3]^{3+}$ that can subsequently oxidize $[\text{CuMac}]^{2-}$ to $[\text{CuMac}]^\cdot$, *i.e.*, Cu^{2+} to Cu^{3+} . Using the spectral features of these complexes, the temporal resolution of catalytic intermediates can be directly observed, and rate constants of electron transfer (ET) and proton-coupled electron transfer (PCET) processes can be determined. Previous density functional theory (DFT) calculations suggested two different pathways later in the cycle, in which $[\text{CuMac}]^{2-}$ can engage, depending on the operational pH. Both mechanisms involve a single electron transfer water nucleophilic attack (SET-WNA), but they diverge in the intermediate generated between the SETs responsible for O-O bond^[15].

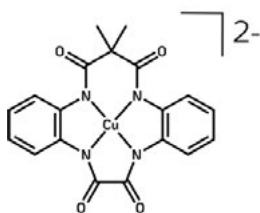


Figure 4.2. Water oxidation electrocatalyst $[\text{CuMac}]^{2-}$ structure.

Here we wish to address the early stage of the catalytic mechanism using single pulse transient absorption (TA) photolysis. Reported data suggest ambiguity in the nature of the one-electron oxidized Cu-complex $[\text{CuMac}]^\cdot$. Supported by X-ray absorption spectroscopy (XAS), electron paramagnetic resonance (EPR), and nuclear magnetic resonance (NMR) it was found that in organic solvents, such as methanol, oxidation of $[\text{CuMac}]^{2-}$ to $[\text{CuMac}]^\cdot$ occurs at the metallic center, generating a d^8 , diamagnetic Cu^{3+} . In contrast, in water, the attempt to identify such species failed, and $[\text{CuMac}]^\cdot$ shows the typical features of a d^9 paramagnetic species Cu^{2+} , leading to the idea that ligand-centered oxidation occurred^[16].

4.2 RESULTS

4.2.1 $[\text{Ru}(\text{bpy})_3]^{2+}/\text{Na}_2\text{S}_2\text{O}_8$ photoluminescence quenching

Although the $[\text{Ru}(\text{bpy})_3]^{2+}/\text{S}_2\text{O}_8^{2-}$ system has been studied extensively in the past ^[17,18], we performed photoluminescence (PL) quenching experiments to gain a better understanding of the effects and interactions taking place between the photosensitizer and the electron acceptor. We combined time-resolved (TR) and steady-state (SS) PL quenching experiments to differentiate between dynamic and static mechanisms through a Stern-Volmer analysis ^[19].

Dynamic quenching involves the electron transfer from the excited state photosensitizer to the quencher through a bimolecular collision. The bimolecular quenching reduces the PL intensity (I) and the photosensitizer's PL lifetime (τ) because it bypasses the intrinsic, radiative, and non-radiative decay. The Stern-Volmer relationship describes this process in terms of the relative PL quantum yield of the photosensitizer in the presence (ϕ_Q) and absence of the oxidizing quencher (ϕ_0) at concentration $[Q]$ as a function of the rate constants:

$$\phi_Q = \frac{\text{emitted photons}}{\text{absorbed photons}} = \frac{k_r}{k_r + k_{nr} + k_Q[Q]}$$

$$\frac{\phi_0}{\phi_Q} = \frac{k_r + k_{nr} + k_Q[Q]}{k_r + k_{nr}} = 1 + \tau_0 k_Q[Q] = 1 + K_D[Q]$$

$$\frac{\tau_0}{\tau} = 1 + \tau_0 k_Q[Q] = 1 + K_D[Q]$$

Where k_r and k_{nr} are the photosensitizer's radiative and non-radiative rate constants in the absence of the quencher, respectively, and $\tau_0 = (k_r + k_{nr})^{-1}$ is the resulting intrinsic lifetime. The quenching is described by a bimolecular quenching rate constant k_Q . In these expressions, K_D is the dynamic Stern-Volmer quenching constant. PL intensity (I_0/I_Q) and PL lifetime (τ_0/τ) measurements can be used to determine K_D . If the K_D s of both experiments are identical, the quenching mechanism is purely dynamic in nature.

However, quenching can also occur statically ^[18,20,21]. Static quenching appears when the photosensitizer and the quencher interact to form a non-luminescent ground-state complex or ion pair. The static quenching depends on the association constant of the complex:

$$K_S = \frac{[\text{P-Q}]}{[\text{P}][\text{Q}]}$$

Where [P–Q] is the concentration of the photosensitizer/quencher complex and [P] is the concentration of the free, un-complexed photosensitizer. In this case, the fraction of PL that remains is given by the ratio of [P] and [P]₀, where [P]₀ = [P] + [P–Q] is the total concentration of the photosensitizer present. In that case

$$\frac{\phi_0}{\phi_Q} = \frac{[P]_0}{[P]} = 1 + K_S[Q]$$

Hence, the fractional steady-state luminescence I_0/I_Q scales also linearly with the quencher concentration in systems where static quenching is the only contribution. The slope of the Stern-Volmer equation then yields the equilibrium constant (K_S). Static quenching makes a fraction of the photosensitizers non-luminescent but does not affect the un-complexed photosensitizers. Hence, for pure static quenching, the PL lifetime remains unaffected, or $\tau_0/\tau = 1$. This feature allows differentiating between static and dynamic quenching.

In practice, dynamic and static quenching often co-occur. This leads to the modified Stern-Volmer equation, which includes a term that is quadratic in [Q]:

$$\frac{\phi_0}{\phi_Q} = (1 + K_S[Q])(1 + K_D[Q])$$

We first studied the quenching of photoexcited [Ru(bpy)₃]²⁺ by persulfate in deionized water solutions using PL lifetime (Figure 4.2a) and PL intensity (Figure 4.2b). The corresponding Stern-Volmer plots (Figure 4.2c) show the relative rate constants ($k_{obs}/k_0 = \tau_0/\tau$) and relative intensities I_0/I_Q as a function of the persulfate concentration. It can be seen that $k_{obs}/k_0 < I_0/I_Q$, which indicates that both dynamic and static quenching occur. At high Na₂S₂O₈ concentrations, the Stern-Volmer plot does not show a quadratic relationship in [Na₂S₂O₈] as expected from a mixed dynamic and static quenching mechanism. Instead, a downward curvature is observed (Figure 4.2c), suggesting that the quenching is suppressed when increasing the persulfate concentration. Previous works reported a similar behavior for steady-state analysis of the current system^[17,18]. The phenomenon was ascribed by Polyansky *et al.* due to a low electrolyte concentration. Considering the system in the absence of electrolyte, a progressive increase in [Na₂S₂O₈] increases the ionic strength (μ) of the sample, which ultimately results in a drop of K_S and k_Q .

Therefore, we examine the data points at low [Na₂S₂O₈], where the Stern-Volmer plot shows linearity (Figure 4.2c; inset), to estimate the maximum k_Q^0 and K_S^0 when μ approaches zero. From the TR analysis, we determined a $K_D^0 = 2100 \text{ M}^{-1}$ and, consequently, a $k_Q^0 = 3.6 \times 10^9 \text{ M}^{-1} \text{ s}^{-1}$. Using the SS experiment and considering that in

the range $[Q] < 0.3 \text{ M}$ the quadratic term is negligible, we established a $K_S^0 = 1790 \text{ M}^{-1}$, from the linear dependence $\phi_0/\phi_Q = (K_D + K_S)$. This conclusion opposes Polyansky's result, where a $K_S < 10 \text{ M}^{-1}$ was calculated in the absence of added electrolyte. Other reports also provide estimates for K_S in the absence of electrolytes varying between $10^2 - 10^3 \text{ M}^{-1}$ [17,21]

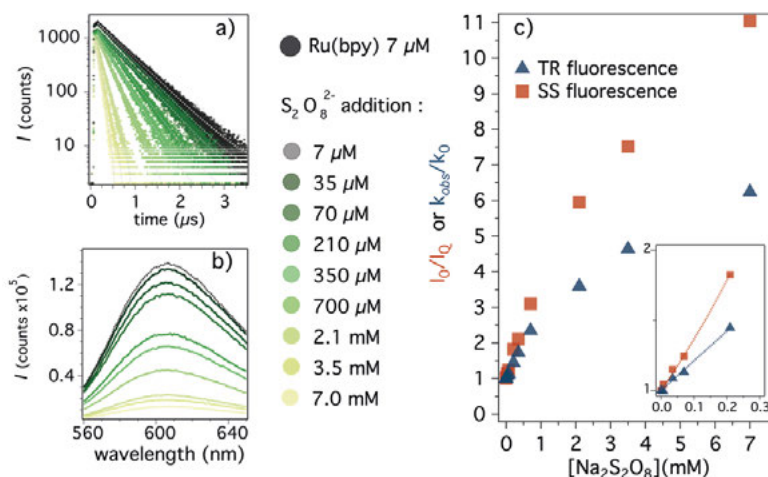


Figure 4.2. Quenching analysis of $[\text{Ru}(\text{bpy})_3]\text{Cl}_2$ ($7 \mu\text{M}$) by $\text{Na}_2\text{S}_2\text{O}_8$ at different concentrations ($7 \mu\text{M}$ to 7 mM) in deionized water solutions. a) Time-resolved (TR) and b) steady-state (SS) PL measurements. c) Stern-Volmer plot analysis. For TR, excitation was at 405 nm , and the PL was probed at 600 nm . For SS, excitation was at 450 nm .

A similar Stern-Volmer analysis was performed to investigate the PL response of $[\text{Ru}(\text{bpy})_3]^{2+}$ in the presence of $(\text{NMe}_4)_2[\text{CuMac}]$. Figure 4.3 clearly shows that $[\text{CuMac}]^{2-}$ also interacts with $[\text{Ru}(\text{bpy})_3]^{2+}$ and quenches its photoluminescence. Single-exponential fits of the PL intensity vs. time (Figure 4.3a) result in a linear variation of the rate constant for decay of the $^3\text{MLCT}$ state of $[\text{Ru}(\text{bpy})_3]^{2+}$ varying from $1.73 \times 10^6 \text{ s}^{-1}$ in the absence of $[\text{CuMac}]^{2-}$, to $2.40 \times 10^6 \text{ s}^{-1}$ in a sample containing $100 \mu\text{M}$ $[\text{CuMac}]^{2-}$. The Stern-Volmer analysis (Figure 4.3d) reveals a dynamic-quenching constant $K_D = 3.7 \times 10^3 \text{ M}^{-1}$ and bimolecular quenching rate constant $k_Q = 6.4 \times 10^9 \text{ M}^{-1}\text{s}^{-1}$, respectively. The latter value approaches the diffusion-controlled rate constant, which was estimated to be $1.8 \times 10^{10} \text{ M}^{-1}\text{s}^{-1}$ by the Smoluchowski equation for charged particles:

$$k_{d0} = \frac{4\pi N}{1000} (R_{\text{Ru}} + R_{\text{q}}) (D_{\text{Ru}} + D_{\text{q}}) f(U)$$

Where N is Avogadro's number (mol^{-1}), R is the radius of the referred species (cm), D is the diffusion coefficient calculated by the Stokes-Einstein equation ($\text{cm}^2 \text{s}^{-1}$), and $f(U)$ is a function of the interactional electrostatic work U (J) calculated as:

$$f(U) = \frac{\frac{U}{k_B T}}{\exp\left(\frac{U}{k_B T}\right) - 1}$$

$$U = \frac{z_{\text{Ru}} e z_{\text{q}} e}{4\pi\epsilon_0\epsilon_r(R_{\text{Ru}} + R_{\text{q}})} = \frac{z_{\text{Ru}} z_{\text{q}}}{\epsilon_r(R_{\text{Ru}} + R_{\text{q}})} \frac{e^2}{4\pi\epsilon_0}$$

Where z is the number of charges, e is the elementary charge (C), ϵ_0 is the vacuum permittivity (F m^{-1}), and ϵ_r is the relative permittivity in water.

The steady-state PL spectra (Figure 4.3b) show a significant quenching with increasing [CuMac]²⁻ concentration. The static component is much larger than the dynamic quenching, as evidenced by considerable upward bending in the Stern-Volmer plot for [CuMac]²⁻ concentrations above 30 μM , which complies with an exponential more than a quadratic model (Figure 4.3d, faded dashed line). This loss in PL intensity cannot be explained by reduced absorption of $[\text{Ru}(\text{bpy})_3]^{2+}$ due to [CuMac]²⁻ attenuating the excitation because the optical density of [CuMac]²⁻ at 100 μM in water is less than 0.15 at the excitation wavelength of 450 nm (Figure 4.3c). The OD = 0.15 would correspond to a $I_0/I_Q = 1.4$ quenching at 100 μM [[CuMac]²⁻], much less than seen experimentally ($I_0/I_Q = 48$). The modified Stern-Volmer equation, quadratic in $[Q]$, would explain a mixed dynamic/static quenching mechanism but does not fit the data in the entire concentration range.

However, I_0/I_Q varies rather linearly up to 35 μM [[CuMac]²⁻], similarly to k_{obs}/k_0 , but the Stern-Volmer constant is much larger than the one found in the TR-PL experiments. A fit of the quadratic Stern-Volmer equation up to 35 μM [CuMac]²⁻, using $K_D = 3.7 \times 10^3 \text{ M}^{-1}$, yields a $K_S = 3.6 \times 10^4 \text{ M}^{-1}$. Hence static quenching prevails. We note that no changes in the absorption spectrum are observed as a consequence of a ground-state ion-pair formation between the [CuMac]²⁻ and $[\text{Ru}(\text{bpy})_3]^{2+}$ complexes (Figure 4.3c).

The tentative explanation for the exponential increase of I_0/I at higher [CuMac]²⁻ concentration, *i.e.*, > 35 μM , is that the association constants of [CuMac²⁻] and $[\text{Ru}(\text{bpy})_3]^{2+}$ may become larger. This effect can, *e.g.*, occur when next to the 1:1 $[\text{Ru}(\text{bpy})_3]^{2+}/[\text{CuMac}]^{2-}$ complex, also 1:2 or higher ratio complexes in Cu^{2+} are formed, which with a joint charge can attract $[\text{Ru}(\text{bpy})_3]^{2+}$ more strongly.

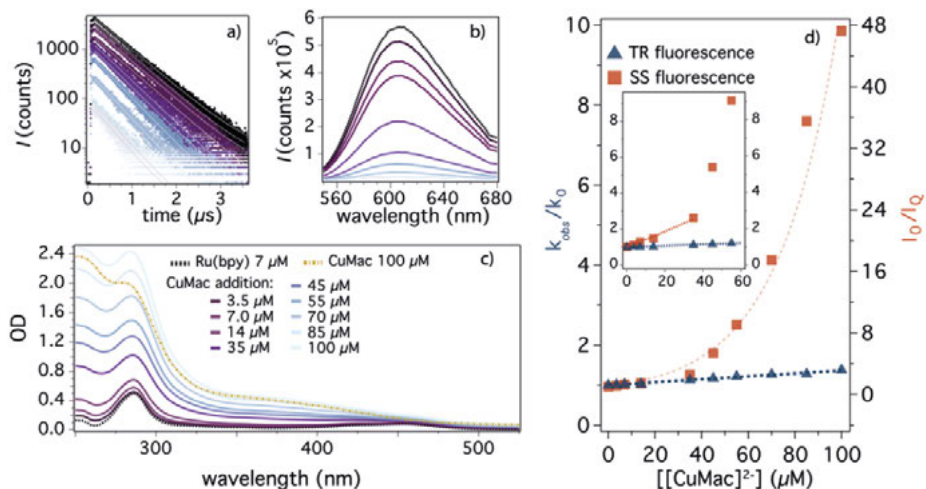
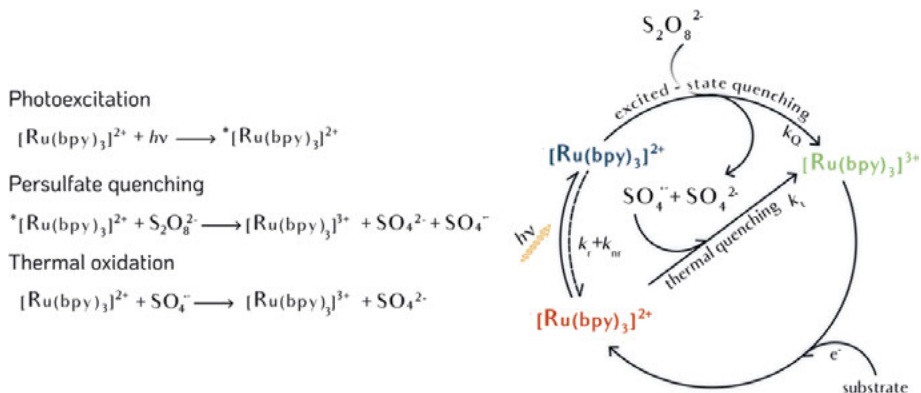


Figure 4.3. Quenching analysis of $[\text{Ru}(\text{bpy})_3]\text{Cl}_2$ ($7\ \mu\text{M}$) by $(\text{NMe}_4)_2[\text{CuMac}]$ ($3.5\ \mu\text{M}$ to $100\ \mu\text{M}$) in deionized water solutions. a) Time-resolved (TR) and b) steady-state (SS) PL measurements of respective mixtures. c) UV-vis spectra $[\text{Ru}(\text{bpy})_3]\text{Cl}_2$ (dotted black trace), $100\ \mu\text{M}$ $(\text{NMe}_4)_2[\text{CuMac}]$ (dotted yellow trace), and mixed system with different $(\text{Me}_4\text{N})_2[\text{CuMac}]$ concentrations. d) Stern-Volmer plot analysis. For TR, excitation was set at $405\ \text{nm}$, and the PL was probed at $600\ \text{nm}$; for SS, excitation was at $450\ \text{nm}$.

The photo-induced processes of the dynamic oxidative quenching of the $^3\text{MLCT}$ state of $[\text{Ru}(\text{bpy})_3]^{2+}$ by $\text{S}_2\text{O}_8^{2-}$ (i.e., not considering the association between $[\text{Ru}(\text{bpy})_3]^{2+}$ and $\text{S}_2\text{O}_8^{2-}$ can be summarized by the reaction scheme 4.1. Electron transfer from $[\text{Ru}(\text{bpy})_3]^{2+}$ to $\text{S}_2\text{O}_8^{2-}$ produces the sulfate dianion (SO_4^{2-}) and radical anion ($\text{SO}_4^{\cdot -}$). The sulfate radical anion $\text{SO}_4^{\cdot -}$ is an oxidizing agent ($E_{1/2} = \sim 2.4\ \text{V}$)^[22] and can oxidize a second equivalent of $[\text{Ru}(\text{bpy})_3]^{2+}$ in the ground state (thermal quenching, k_t). Later in the chapter, we discuss the implications of $[\text{CuMac}]^{2-}$ oxidation in the flash-photolysis experiments by $\text{SO}_4^{\cdot -}$.



Scheme 4.1. Oxidative photocatalytic cycle of $[\text{Ru}(\text{bpy})_3]^{2+}$ in the presence of $\text{S}_2\text{O}_8^{2-}$.

The thermal reaction between $\text{SO}_4^{\cdot -}$ and $[\text{Ru}(\text{bpy})_3]^{2+}$ is investigated by transient absorption (TA). The decreased optical density (OD) at 450 nm is caused by a bleach of $[\text{Ru}(\text{bpy})_3]^{2+}$ in the ground state, which can occur by photo-excitation to the ${}^3\text{MLCT}$ state and thermal oxidation to $[\text{Ru}(\text{bpy})_3]^{3+}$ by $\text{SO}_4^{\cdot -}$. From the traces in Figure 4.4, we can distinguish these two processes. The initial fast bleach in the $[\text{Ru}(\text{bpy})_3]^{2+}$ signal is attributed to the absorption of a photon and the consequent excitation to the ${}^3\text{MLCT}$ state occurring in the femtosecond time-scale, causing the sudden loss in OD. Next, we observed a slower process, further reducing the $[\text{Ru}(\text{bpy})_3]^{2+}$ absorption, which we tentatively assigned to the thermal generation of $[\text{Ru}(\text{bpy})_3]^{3+}$ by oxidation of $[\text{Ru}(\text{bpy})_3]^{2+}$ by $\text{SO}_4^{\cdot -}$. Under the present conditions, the decays fit a single exponential model. This can be expected because the difference in concentration between $[\text{Ru}(\text{bpy})_3]^{2+}$ in the ground state and the transient $\text{SO}_4^{\cdot -}$ radical anion is high enough to treat it as a $[\text{Ru}(\text{bpy})_3]^{3+}$ formation that is pseudo-first-order in $[\text{SO}_4^{\cdot -}]$. The electron transfer rate constants calculated is $6.4 \times 10^9 \text{ M}^{-1} \text{ s}^{-1}$. The fast rate constant close to the diffusion-controlled limit suggests it is prone to react quickly as soon as $\text{SO}_4^{\cdot -}$ is released. A long-lived $[\text{Ru}(\text{bpy})_3]^{3+}$ is generated by both excited-state and thermal quenching. In our TA study, an excess of $\text{Na}_2\text{S}_2\text{O}_8$ (50 mM) is used to buffer the depletion of the sacrificial quencher along the experiment and to maximize the excited-state quenching rate compared to the thermal quenching, as the latter is dependent on the concentration of $\text{SO}_4^{\cdot -}$.

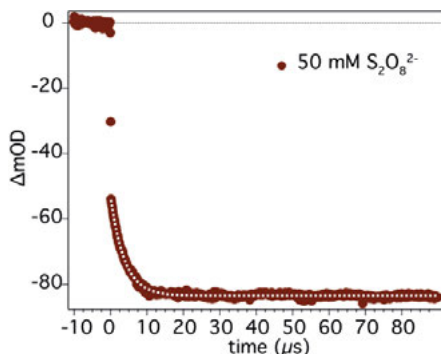


Figure 4.4. Transient absorption probed at 450 nm of 40 μM $[\text{Ru}(\text{bpy})_3]\text{Cl}_2$ containing 50 mM $\text{Na}_2\text{S}_2\text{O}_8$ in an aqueous phosphate buffer solution (0.025 M) at pH = 7.3.

4.2.2 Flash-photolysis: $[\text{CuMac}]^{2-}$ oxidation

Flash-quenched photolysis was used to examine the processes involving $[\text{CuMac}]^{2-}$ in a phosphate buffer solution (PBS) at neutral pH. Transient absorption (TA) spectra in the UV-vis region of a ternary system consisting of $[\text{Ru}(\text{bpy})_3]\text{Cl}_2$ (40 μM), $\text{Na}_2\text{S}_2\text{O}_8$ (50 mM), and $(\text{NMe}_4)_2[\text{CuMac}]$ (500 μM) in its initial oxidation state are shown in Figure 4.5a. Following the laser pulse at 532 nm, which likely directly excites the $^3\text{MLCT}$ state, the bleaching of the $[\text{Ru}(\text{bpy})_3]^{2+}$ absorption is observed at 452 nm, confirming that $[\text{Ru}(\text{bpy})_3]^{2+}$ is no longer in the ground state, but either in the excited $^3\text{MLCT}$ state or it has been oxidized to $[\text{Ru}(\text{bpy})_3]^{3+}$. The $[\text{Ru}(\text{bpy})_3]^{2+}$ ground state recovers quickly in the first microseconds, and after 50 μs , the spectrum's shape does not change significantly. Because in the absence of $[\text{CuMac}]^{2-}$, the photobleaching is much longer lived (Figure 4.4), these results are consistent with the oxidative quenching of the $[\text{Ru}(\text{bpy})_3]^{2+}$ $^3\text{MLCT}$ state by persulfate to $[\text{Ru}(\text{bpy})_3]^{3+}$ and subsequent reduction of the formed $[\text{Ru}(\text{bpy})_3]^{3+}$ by $[\text{CuMac}]^{2-}$ that regenerates $[\text{Ru}(\text{bpy})_3]^{2+}$ in the ground state. After 5 μs , a broad photo-induced absorption band ($\Delta\text{OD} > 0$) arises in the investigated spectral window, which grows and reaches a maximum intensity between 100–500 μs , to decay after that slowly. Control transient absorption measurements of $(\text{NMe}_4)_2[\text{CuMac}]$ (Figure 4.5b) and $(\text{NMe}_4)_2[\text{CuMac}]/\text{Na}_2\text{S}_2\text{O}_8$ solutions (Figure 4.5c) show no change in the optical density following the laser pulse in the 0.1–2 μs time range, indicating that $[\text{CuMac}]^{2-}$ does not undergo any photophysical nor photochemical process under these conditions. Thus, we attribute the positive change in OD in Figure 4.5a to $[\text{CuMac}]^{2-}$ generated by one-electron oxidation of $[\text{CuMac}]^{2-}$ via a single electron transfer to $[\text{Ru}(\text{bpy})_3]^{3+}$.

To study the kinetics of this bimolecular electron transfer reaction, TA was recorded for samples containing different concentrations of [CuMac]²⁻ while monitoring the recovery of the photobleaching signal of [Ru(bpy)₃]²⁺ at 450 nm (Figure 4.5d). As expected from a pseudo-first-order reaction, the resulting kinetic traces fit with a single exponential model (dashed line, Figure 4.5d), and the bimolecular electron transfer rate constant (k_{ET}) was calculated to be $3.45 \times 10^8 \text{ M}^{-1} \text{ s}^{-1}$ from the linear regression in Figure 4.5e.

$$\frac{d[[\text{Ru}(\text{bpy})_3]^{2+}]}{dt} = k_{ET}[[\text{CuMac}]^{2-}] [[\text{Ru}(\text{bpy})_3]^{3+}] = k_{1\text{obs}}[[\text{Ru}(\text{bpy})_3]^{3+}]$$

and

$$[[\text{Ru}(\text{bpy})_3]^{2+}](t) = A \exp(-k_{1\text{obs}} t)$$

Because the reduction of [Ru(bpy)₃]³⁺ by [CuMac]²⁻ produces [Ru(bpy)₃]²⁺, the recovery the [Ru(bpy)₃]²⁺ bleaching signal has the same rate constant ($k_{1\text{obs}}$) as the loss of [Ru(bpy)₃]³⁺. As can be seen in Figure 4.5e, only the initial points were fit, as a deviation from linearity in $k_{1\text{obs}}$ is observed for [CuMac]²⁻ concentrations above 300 μM . We do know that in concentrated solution (> 1 mM), [CuMac]²⁻ adsorbs on electrodes upon electrochemical experiments and that higher concentration (10 mM) in water it tends to form very viscous solutions. Aggregation might be responsible for changes in the diffusion coefficient, slowing down the bimolecular reaction with the photosensitizer.

TA traces were also recorded at 570 nm, a wavelength far enough from the [Ru(bpy)₃]²⁺ absorption band, where we can still observe a signal growth of the newly generated copper species. Using a long-pass optical filter (550 nm) for the probe light, prolonged exposure of the sample to 450 nm light is avoided to exclude that the photosensitizer is excited throughout the experiment and prevent uncontrollable redox processes. This would deplete the local concentration of [CuMac]²⁻ with enough time, especially when the initial concentration is relatively low.

Figure 4.6a shows these traces as a function of [CuMac]²⁻ concentration. The curves show that the signal takes much longer to stabilize than Figure 4.5d. We fit a double exponential model, constraining one set of rate constants ($k_{1\text{obs}} \pm 10\%$) to the ones obtained from the analysis in Figure 4.5e, leaving $k_{2\text{obs}}$ free.

$$\text{OD}(t) = A \exp(-k_{1\text{obs}} t) + B \exp(-k_{2\text{obs}} t)$$

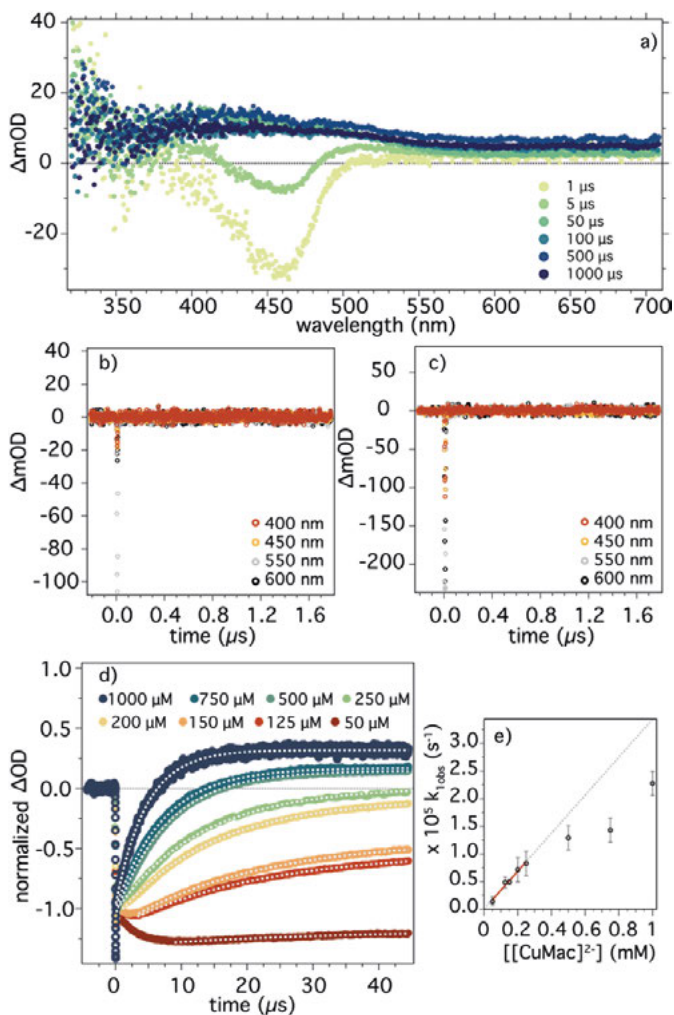


Figure 4.5. Transient spectra of a) $(\text{NM}_4)_2[\text{CuMac}]$ (500 μM) with $\text{Na}_2\text{S}_2\text{O}_8$ (50 mM), and $[\text{Ru}(\text{bpy})_3]\text{Cl}_2$ (40 μM) between 0 and 1 ms, pump at 532 nm. b, c) Control kinetic traces at different wavelengths of b) $(\text{NMe}_4)_2[\text{CuMac}]$ (500 μM), and c) $(\text{NMe}_4)_2[\text{CuMac}]$ (500 μM) with $\text{Na}_2\text{S}_2\text{O}_8$ (50 mM). d) Transient absorption of 40 μM $[\text{Ru}(\text{bpy})_3]\text{Cl}_2$ with $\text{Na}_2\text{S}_2\text{O}_8$ (50 mM) and different concentrations of $[\text{CuMac}]^{2-}$ and pseudo-first order exponential fits (dashed lines). Pump at 460 nm, probe at 450 nm. e) Observed rate constants as a function of $[\text{CuMac}]^{2-}$. All experiments were performed in PBS (0.025 M) and pH 7.3.

Interestingly, the $k_{2\text{obs}}$ values do not change with the $[\text{CuMac}]^{2-}$ concentration gradient, revealing that the second process is unrelated to any process involving the initial $[\text{CuMac}]^{2-}$ species (e.g., thermal oxidation by $\text{SO}_4^{\cdot -}$). We also noted that the pre-factors ratio, A/B, maintains the same value (~ 2.5), confirming the validity of the bi-

exponential model for the process studied. We conclude that after one-electron oxidation of $[\text{CuMac}]^{2-}$, the formed $[\text{CuMac}]^{\cdot -}$ undergoes a subsequent process, resulting in an intermediate that is stable in the millisecond time scale. pH-dependent measurements (Figure 4.6c) revealed that the second process is accelerated from a $k_{2\text{obs}} = 9.4 \times 10^3 \text{ s}^{-1}$ at pH 7.1 to $k_{2\text{obs}} = 1.1 \times 10^5 \text{ s}^{-1}$ at pH 11. The $k_{2\text{obs}}$ being independent of changes in $[\text{CuMac}]^{2-}$ concentration and its positive trend in a more basic environment suggests that the second process follows the initial bimolecular reaction and most likely involves the interaction with a hydroxo species. It is also noted that at pH above 10, a third kinetic component appears, which reduces the ΔOD over time. A triple exponential model returns a $k_{3\text{obs}} 9.1 \times 10^2 \text{ s}^{-1}$ and $1.3 \times 10^3 \text{ s}^{-1}$ at pH 10 and 11.2, respectively. Independently from the operational pH, all the traces end with a positive ΔOD , indicative of a long-lived intermediate.

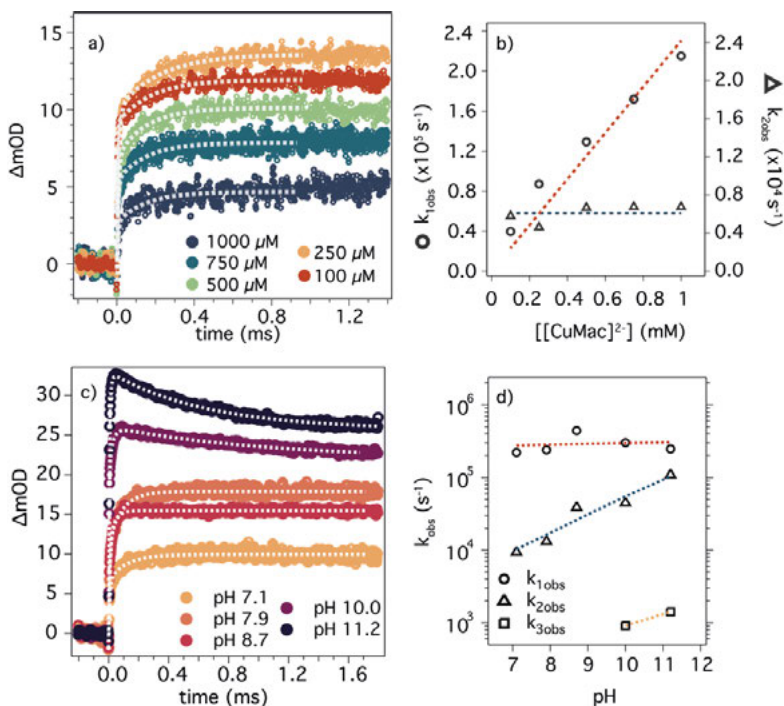


Figure 4.6. a) Kinetic traces probed at 570 nm at different concentrations of $(\text{NMe}_4)_2[\text{CuMac}]$, b) Rate constants observed versus concentration $[\text{CuMac}]^{2-}$, pH 7 (PBS 0.025 M). $k_{1\text{obs}}$ are constrained to the values obtained from the bimolecular electron transfer with $[\text{Ru}(\text{bpy})_3]^{3+}$ (450 nm traces). c, d) pH-dependent kinetic traces probed at 570 nm of 500 μM $(\text{NMe}_4)_2[\text{CuMac}]$ within c) 1.6 ms and d) 1.6 s. In all experiments $\text{Na}_2\text{S}_2\text{O}_8$ (50 mM), and $[\text{Ru}(\text{bpy})_3]\text{Cl}_2$ (40 μM), and PBS 0.025 M were used.

One-electron oxidized $[\text{CuMac}]^{\cdot-}$ was also produced chemically by I_2 ($E_{1/2} = 0.54$ V vs. NHE), and its absorption spectrum is compared to that of $[\text{CuMac}]^{2-}$ in Figure 4.7a. Only slight differences are noted in the spectral features, with a slight blue shift of the band initially centered at 400 nm, together with a decrease in OD at 570 nm (Figure 4.7a; inset), whereas we observed a positive ΔOD in the TA experiments. Titration of an $(\text{NMe}_4)_2[\text{CuMac}]$ solution with $\text{Na}_2\text{S}_2\text{O}_8$ showed similar optical behavior (Figure 4.7b).

$\text{S}_2\text{O}_8^{2-}$ can undergo a variety of redox reactions ^[22,23], and its known sluggish kinetics prevents it from reacting readily.



However, due to the low oxidation potential of the couple $[\text{CuMac}]^{2-}/[\text{CuMac}]^{\cdot-}$ (0.35 V vs. NHE) and the significant excess of $\text{Na}_2\text{S}_2\text{O}_8$, the oxidation may occur in the dark (k_d) without the contribution of $[\text{Ru}(\text{bpy})_3]^{3+}$, as the UV-vis spectra demonstrate. Therefore, single-pulsed flash-photolysis experiments likely show the second oxidation of the $[\text{CuMac}]^{2-}$, i.e., from $[\text{CuMac}]^{\cdot-}$ to $[\text{CuMac}]$.

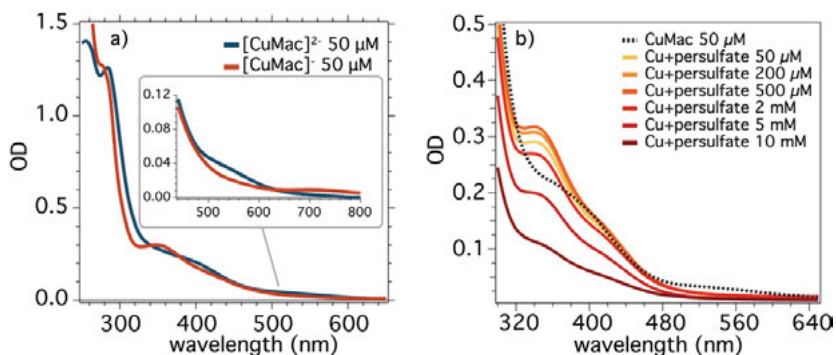
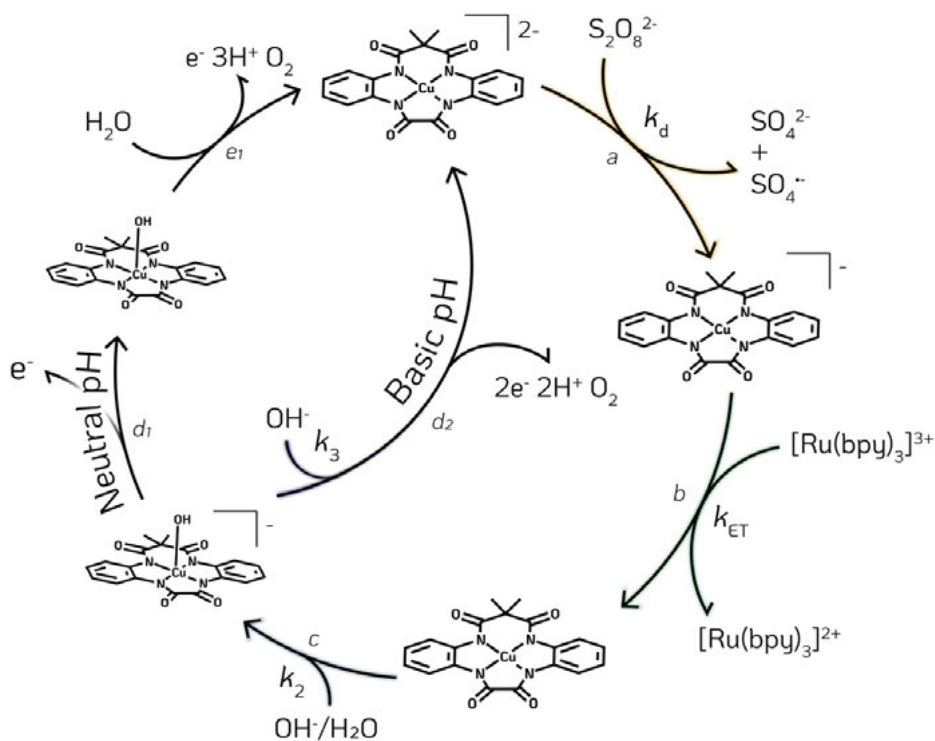


Figure 4.7. UV-vis absorption spectra of a) $[\text{CuMac}]^{2-}$ and chemically oxidized $[\text{CuMac}]^{\cdot-}$ by I_2 . b) Persulfate titration in $[\text{CuMac}]^{2-}$ solution.

We can identify the following processes according to the previously proposed cycle (Scheme 4.2) ^[16]. The first electron transfer, *a*, is driven by persulfate producing $[\text{CuMac}]^{\cdot-}$. The second electron transfer *b*, by a bimolecular reaction with $[\text{Ru}(\text{bpy})_3]^{3+}$ (k_{ET}) producing $[\text{CuMac}]$. The subsequent reaction, *c*, is proposed to involve an aqua or hydroxy species, coordinating axially with the Cu site. From TA spectroscopy at 570 nm, we found a second process, following the electron transfer *b*, which increases its rate ($k_{2\text{obs}}$) as the pH is raised (Figures 4.6d), and therefore we ascribed it to the OH⁻

coordination to $[\text{CuMac}]$, c. At this point of the catalytic cycle, two different paths are expected. At neutral pH, the O-O bond formation requires a further electron transfer (d_1) before generating a more electrophilic oxygen (Cu-OH), which can accommodate the nucleophilic attack from H_2O (WNA). We cannot probe this process as of our single-pulsed flash-photolysis experimental set-up. Alternatively, at high pH (> 10), the more nucleophilic OH^- can react readily, beginning the O-O bond formation, and the following two-single electron transfers (SET-WNA). We detect the initial OH^- coordination of step d_2 as a slow decay in ΔOD ($k_{3\text{obs}}$) when the pH > 10 (Figure 4.6c, d).



Scheme 4.2. $[\text{CuMac}]^{2-}$ water oxidation proposed catalytic cycle. The highlighted reaction arrows show the processes investigated in the study in the presence of $\text{Na}_2\text{S}_2\text{O}_8$ and $[\text{Ru}(\text{bpy})_3]^{3+}$.

4.3 CONCLUSIONS

We addressed the initial steps of the water oxidation reaction catalytic cycle by $[\text{CuMac}]^{2-}$, using flash-quench photolysis ($[\text{Ru}(\text{bpy})_3]^{2+}/\text{S}_2\text{O}_8^{2-}$) to induce $[\text{CuMac}]^{2-}$ oxidation and probe the spectroscopic changes to gain insight into the reaction

mechanism. PL quenching analysis has shown the intricate interactions between the photosensitizer, the quencher, and $[\text{CuMac}]^{2-}$. Firstly, we confirmed the $([\text{Ru}(\text{bpy})_3]^{2+})$ quenching by $\text{S}_2\text{O}_8^{2-}$, and its typical down-bended Stern-Volmer plot in the absence of electrolyte, caused by the decrease of rate constants (k_Q , K_D , K_S) as a function of the ionic strength (μ). SS and TR analysis showed that both static and dynamic quenching occur and are affected by μ . We estimated their rate constants at $\mu = 0$ to be $K_S^0 = 1200 \text{ M}^{-1}$ and $K_D^0 = 2100 \text{ M}^{-1}$ ($k_Q^0 = 3.6 \times 10^9 \text{ M}^{-1} \text{ s}^{-1}$), pointing up the major dynamic contribution to the quenching.

$[\text{CuMac}]^{2-}$ has also revealed to quench the $[\text{Ru}(\text{bpy})_3]^{2+}$ PL, with a bimolecular rate constant $k_Q = 6.4 \times 10^9 \text{ M}^{-1} \text{ s}^{-1}$. On the other hand, SS PL features a massive static quenching, which grows exponentially with $[\text{CuMac}]^{2-}$ concentration. We excluded that light absorbed by $[\text{CuMac}]^{2-}$ could be responsible for the reduced PL signal, as $[\text{CuMac}]^{2-}$ absorption features (0.15 OD at 450 nm) would not justify the suppression of PL by 48 times. Instead, we claim that an aggregation between $[\text{CuMac}]^{2-}$ and $[\text{Ru}(\text{bpy})_3]^{2+}$ occurs, which can yield a cluster of multiple copper complexes interacting with one equivalent of the photosensitizer. However, TA experiments have shown reasonable initial bleaching in OD, demonstrating the successful excitation of $[\text{Ru}(\text{bpy})_3]^{2+}$, and thus suggesting that in the tertiary system, the static quenching by $[\text{CuMac}]^{2-}$ is inhibited because of $\text{S}_2\text{O}_8^{2-}$ presence.

Although its sluggish kinetics, we propose that $\text{S}_2\text{O}_8^{2-}$ oxidizes $[\text{CuMac}]^{2-}$ in the dark, affording the one-electron oxidized and stable species $[\text{CuMac}]^{\cdot-}$ (Scheme 4.2a). Flash-photolysis experiments at 450 nm indicate the recovery of $[\text{Ru}(\text{bpy})_3]^{2+}$ in the μs time scale with a bimolecular electron transfer rate constant $k_{\text{ET}} = 3.45 \times 10^8 \text{ M}^{-1} \text{ s}^{-1}$, which generated the transient $[\text{CuMac}]^{\cdot-}$ with a $\Delta\text{OD} > 0$ (Scheme 4.2b). Further investigation of kinetic traces at 570 nm, where no $[\text{Ru}(\text{bpy})_3]^{2+}$ contributes to the ΔOD signal, reveals a more complex process. Particularly we observed a bi-exponential behavior of the signal. The first and faster process relates to the electron transfer (k_{ET}) also observed at 450 nm, while the second, independent of the $[\text{CuMac}]^{2-}$ concentration, was ascribed to a consecutive reaction. pH-dependent analysis showed how the second process is affected by it, increasing its rate as the OH^- concentration is raised. This fits the proposed cycle where water coordinates $[\text{CuMac}]$ at this cycle stage (Scheme 4.2c). We calculated a $k_{2\text{obs}} = 9.4 \times 10^3 \text{ s}^{-1}$ at pH = 7 and $k_{2\text{obs}} = 1.1 \times 10^5 \text{ s}^{-1}$ at pH = 11. We detected a third kinetic component, decreasing the ΔOD only when the pH is above 10. This is also coherent with the mechanism, as two different paths were proposed depending on the operational pH. At neutral pH, a further electron transfer is expected to happen before the cycle proceeds (Scheme 4.2d₁), while at basic pH, coordination of a hydroxo species was calculated to be favored (Scheme 4.2d₂).

Overall, we highlighted the complexity of the sacrificial photocatalytic system due to the interaction between the reagents and the oxidation in the dark of the substrate by S₂O₈²⁻. Nevertheless, we were able to rationalize and confirm the early reaction mechanism that was previously proposed based on electrochemical analysis and computational calculations.

4.4 EXPERIMENTAL DETAILS

Materials: Solvents and products were provided by Sigma-Aldrich, Alfa Aesar, or TCI chemicals unless indicated otherwise and used without further purification. HPLC-grade water (18 MΩ cm) was used in all electrochemical experiments. Aqueous buffer solutions at pH 7 and 11 were prepared using specific concentrations of dibasic and tribasic phosphate salts such that the final ionic strength was 0.1 M or 0.025 mM.

Electrochemical characterization: Buffer solutions were prepared as follows: pH = 7.5 buffered solutions (*I* = 0.1 M): powders of NaH₂PO₄ (0.0073 mol) and Na₂HPO₄ (0.0306 mol) were dissolved with sufficient HPLC grade H₂O to make up 1 L of solution. pH = 11.5 buffered solution (*I* = 0.1 M): powders of Na₂HPO₄ (0.0186 mol) and Na₃PO₄ (0.0073 mol) were dissolved with sufficient H₂O to make up 1 L of solution. The correct pH was measured after preparation with a pH meter.

Steady-state PL spectra were obtained using an Edinburgh Instruments FLSP920 fluorescence spectrometer featuring a xenon arc discharge lamp and double monochromators in excitation and emission. The emission detector is positioned horizontally at a 90° angle to the light source. The excitation wavelength was 450 nm.

UV-vis absorption spectra were recorded using a PerkinElmer Lambda 1050 UV-vis-NIR spectrophotometer.

Time-correlated single photon counting photoluminescence studies were performed using an Edinburgh Instruments LifeSpec-PS consisting of a 400-nm picosecond (pulse width ~ 50 ps) laser (PicoQuant PDL 800B) operated at 100 kHz and a Peltier-cooled Hamamatsu microchannel plate photomultiplier (R3809U-50).

Transient absorption spectroscopy: Flash-quench photolysis coupled to transient absorption (TA) spectroscopy was employed for the determination of rates of ET. Sample excitation was provided by a frequency tripled Nd:YAG laser (Quantel, BrilliantB) that delivered pulses of ~7 ns duration, ~30 mJ/pulse at 532 nm, or tuned to provide 460 nm pulses through an optical parametric oscillator (OPO). The analyzing light was supplied by an unpulsed (> 100 μs experiments) or pulsed (≤ 100 μs experiment) 150 W xenon lamp in a flash photolysis spectrometer (Applied Photophysics, LKS.80). The outgoing light source was filtered by an interference optic filter (450 nm) or a long-pass filter (>550 nm). Light passing through the sample was sent through a monochromator set to a bandwidth of 1 nm before reaching the 5-stage P928 photomultiplier tube (Hamamatsu). Samples were degassed for 5 minutes before

each experiment by N₂ purging to avoid the quenching of the ruthenium excited state by molecular oxygen. Samples were contained in cuvettes with dimensions of 10 mm x 10 mm and were shaken before each measurement to re-equilibrate the local concentration. The signals were digitized using an Agilent Technologies Infinium digital oscilloscope (600 MHz). Transient absorption traces were generated within the Applied Photophysics LKS software package. Curve fitting and data analysis were performed in Igor Pro version 8.04.

Preparation of [CuMac]: [CuMac]²⁻ (134.9 mg, 0.235 mmol) was dissolved in methanol (5 mL), then a methanolic solution (5 mL) containing a slight excess of I₂ (32.7 mg, 0.129 mmol) was added to the mixture and heated at 50 °C for 10 min. The appearing precipitate was filtered off, and the solution was evaporated until a dry solid was obtained. The solid was further purified by recrystallization from methanol/diethyl ether.

4.5 REFERENCES

- [1] R. C. McAtee, E. J. McClain, C. R. J. Stephenson, *Trends. Chem.* **2019**, 1, 1, 111–125.
- [2] N. A. Romero, D. A. Nicewicz, *Chem. Rev.* **2016**, 116, 17, 10075–10166.
- [3] A. Lewandowska-Andralojc, D. E. Polyansky, R. Zong, R. P. Thummel, E. Fujita, *Phys. Chem. Chem. Phys.* **2013**, 15, 33, 14058.
- [4] S. C. Marguet, M. J. Stevenson, H. S. Shafaat, *J. Phys. Chem. B* **2019**, 123, 46, 9792–9800.
- [5] M. G. Gatty, S. Pullen, E. Sheibani, H. Tian, S. Ott, L. Hammarström, *Chem. Sci.* **2018**, 9, 22, 4983–4991.
- [6] S. I. Shylin, M. V. Pavliuk, L. D’Amario, I. O. Fritsky, G. Berggren, *Faraday Discuss.* **2019**, 215, 162–174.
- [7] L. Francàs, R. Matheu, E. Pastor, A. Reynal, S. Berardi, X. Sala, A. Llobet, J. R. Durrant, *ACS Catal.* **2017**, 7, 8, 5142–5150.
- [8] D. A. Nicewicz, D. W. C. MacMillan, *Science* **2008**, 322, 5998, 77–80.
- [9] J. M. R. Narayanam, J. W. Tucker, C. R. J. Stephenson, *J. Am. Chem. Soc.* **2009**, 131, 25, 8756–8757.
- [10] A. Juris, V. Balzani, F. Barigelletti, S. Campagna, P. Belser, A. von Zelewsky, *Coord. Chem. Rev.* **1988**, 84, 85–277.
- [11] D. M. Arias-Rotondo, J. K. McCusker, *Chem. Soc. Rev.* **2016**, 45, 21, 5803–5820.
- [12] Y. Kaizu, H. Ohta, K. Kobayashi, H. Kobayashi, K. Takuma, T. Matsuo, *J. Photochem.* **1985**, 30, 1, 93–103.
- [13] K. J. Morris, M. S. Roach, W. Xu, J. N. Demas, B. A. DeGraff, *Anal. Chem.* **2007**, 79, 24, 9310–9314.
- [14] R. Bensasson, C. Salet, V. Balzani, *J. Am. Chem. Soc.* **1976**, 98, 12, 3722–3724.
- [15] P. Garrido-Barros, I. Funes-Ardoiz, S. Drouet, J. Benet-Buchholz, F. Maseras, A. Llobet, *J. Am. Chem. Soc.* **2015**, 137, 21, 6758–6761.
- [16] P. Garrido-Barros, D. Moonshiram, M. Gil-Sepulcre, P. Pelosin, C. Gimbert-Suriñach, J. Benet-Buchholz, A. Llobet, *J. Am. Chem. Soc.* **2020**, 142, 41, 17434–17446.
- [17] H. S. White, W. G. Becker, A. J. Bard, *J. Phys. Chem.* **1984**, 88, 9, 1840–1846.
- [18] A. Lewandowska-Andralojc, D. E. Polyansky, *J. Phys. Chem. A* **2013**, 117, 40, 10311–10319.
- [19] J. R. Lakowicz, *Principles of Fluorescence Spectroscopy*, Springer US, Boston, MA, **1999**.
- [20] L. K. Fraiji, D. M. Hayes, T. C. Werner, *J. Chem. Educ.* **1992**, 69, 5, 424–428.

- [21] A. L. Kaledin, Z. Huang, Y. v. Geletii, T. Lian, C. L. Hill, D. G. Musaev, *J. Phys. Chem. A* **2010**, *114*, 1, 73–80.
- [22] D. A. Armstrong, R. E. Huie, W. H. Koppenol, S. v. Lymar, G. Merényi, P. Neta, B. Ruscic, D. M. Stanbury, S. Steenken, P. Wardman, *Pure Appl. Chem.* **2015**, *87*, 11-12, 1139–1150.
- [23] W. Song, J. Li, Z. Wang, X. Zhang, *Water Sci. Technol.* **2019**, *79*, 3, 573–579.

5

IMMOBILIZATION OF A MOLECULAR CU-BASED WOC ON PRINTED ELECTRODES THROUGH COVALENT INTERACTION

5.1 INTRODUCTION

5.1.1 Heterogenization: Diazonium grafting

Molecular transition metal complex catalysts are investigated for energy conversion from renewable sources, *e.g.*, in artificial photosynthesis. This class of compounds has remarkable advantages compared to oxide-based catalysts. Each metal site has the same coordination environment, making them ideal for mechanistic studies. Furthermore, the intrinsic activity of the catalyst can be adjusted for a given application by modifying electron density and steric demand through synthetic functionalization. With the possibility to monitor the mechanism of action, it is possible to rationally design changes in the organic ligand structure that allow improved performance and stability^[1].

The energy sector (and others) aims to reduce costs while maintaining or increasing conversion efficiency to valuable feedstocks. Nonetheless, the main drawback of molecular catalysts often lies in their instability, causing them to degrade or undergo side reactions detrimental to catalyst activity. On the contrary, heterogeneous catalysts often show excellent durability over time. Hence, research is directed towards developing heterogenized catalysts, hybrid systems of molecular active catalytic centers supported on a solid-state material to improve stability and longevity. Bi-molecular decomposition and/or deactivation pathways can be prevented when the catalysts are anchored onto surfaces, enhancing the overall performance. Other advantages are easier product separation, which reduces costs and favors upscaling in industrial applications. Furthermore, in electrocatalytic systems, only the catalysts diffusing within the double layer contribute to product conversion. Hence

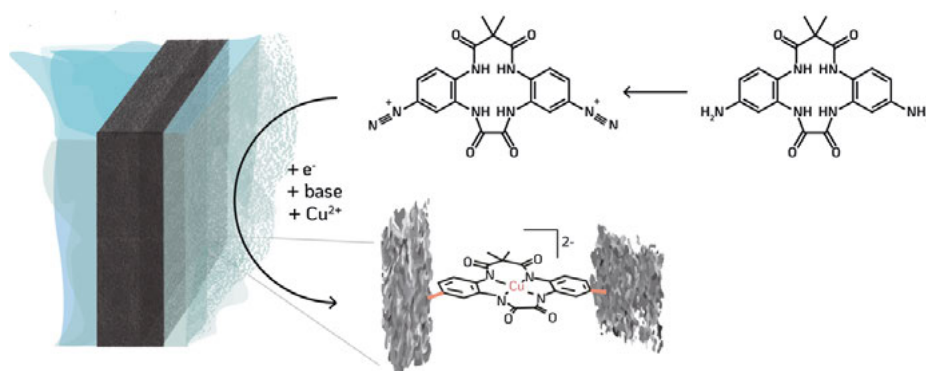
surface immobilization significantly lowers the catalyst loading necessary, resulting in a more affordable reactor design.

As of today, many strategies are viable to modify surfaces with different molecules/functionalities. These strategies can broadly be divided by the type of interaction at the electrode-catalyst interface, namely covalent bonding or physisorption (hydrophobic, π - π interactions, H-bonding, van der Waals). Solid and long-lasting bonds are desirable to ensure the stability of the modified surface, whether for (bio)sensors, protective layers, or other applications^[2-4]. Covalent grafting is one of the most reliable heterogenization methodologies, as it creates strong chemical bonds that can withstand mechanical stress without chemical cleavage or etching. Diazonium salts ($R-N_2^+$) have been employed as precursors for this purpose, as they are highly versatile because of their easy synthesis and the mild conditions required for grafting. These salts can form radical species that engage in covalent bond formation with a variety of substrates, such as carbon-based materials^[5,6], silica^[7], and several metals (*e.g.*, Au, Pd, Pt, Cu, Fe, Zn, Co)^[8-10].

In protic solvents or aqueous acidic media, the diazonium electroreduction can be triggered by applying a negative potential (0 to -0.6 V vs. NHE). Due to the mild potential applied, only a one-electron reduction occurs, concerted with the extrusion of molecular nitrogen. These two processes are key for diazonium surface immobilization^[11]. The carbon-based radical is generated ($E_p = < -0.6$ V) in proximity to the surface and is sufficiently long-lived to react, resulting in a carbon-carbon bond or carbon-metal bond, depending on the electrode material. Diazonium salts are known for their thermal instability even at low temperatures, causing them to decompose violently or, in the worst event, even explode. For this reason, aryl salts are preferred for their enhanced resonance stability. Furthermore, the choice of counterion is also relevant for stability, with hexafluorophosphate, tosylates, disulfonamides, and, particularly, tetrafluoroborates being recognized as the most stable ones^[12]. Once the organic layer covers the electrode, electrochemical techniques can characterize the modified material if any electroactive site is present. Alternatively, surface analysis such as X-ray photoelectron spectroscopy (XPS), atomic force microscopy (AFM), Rutherford backscattering (RBS), and Raman and Auger spectroscopy can be employed^[10].

Optimization of molecular catalyst heterogenization is still needed. A successful immobilization does not necessarily mean that the features of the original material are retained, like activity, selectivity, substrate mass transfer, and surface hydrophobicity (or hydrophilicity). In this work, we aim to fabricate carbon-based electrodes that are functionalized with a water oxidation catalyst $(NMe_4)_2[CuMac]$ using a diazonium electroreduction strategy. We first modified the macrocyclic scaffold to make it suitable for diazonium salt synthesis and its subsequent grafting to a surface. In parallel, we also

prepared a methacrylate-based polymer to be blended in a graphite-based slurry. The latter is used to fabricate simple and low-cost screen-printed electrodes. Finally, the decorated catalyst was immobilized onto the surfaces through covalent interactions to yield a hybrid water oxidation catalyst.



Scheme 5.1. Schematic representation for molecular water oxidation heterogenization using a diazonium grafting strategy.

5.1.2 Nitroxide-mediated radical polymerization

Nowadays, nitroxide-mediated polymerization (NMP) is a vastly used living radical polymerization method ^[13] in polymer science, thanks to nitroxide's ability to engage the radical polymer in reversible activation-deactivation reactions controlling its growth and limit the undesired radical reactivity ^[14]. The real game-changer that enabled the technology was the development of alkoxyamine-based initiators ^[13,15,16] (e.g., MAMA-SG1, Figure 5.1). Only a moderate thermal activation cleaves the C-ON bond, yielding a carbon radical, initiating the polymerization, and the nitroxide species as the controlling agent. The derived nitroxides have a high dissociation rate constant (k_d), which allows the dormant species (MAMA-[M]_n-SG1, Figure 5.1) to thermolyze into the radical (MAMA-[M]_n), expanding the chain upon reaction with a monomer unit ^[17,18]. The propagation step thus proceeds mainly without termination reactions such as recombination or disproportionation reactions. However, some materials can cause problems in reactivity, such as un-conjugated monomers, in which the C-ON bond of the dormant species is so stable to bring the reaction to a halt.

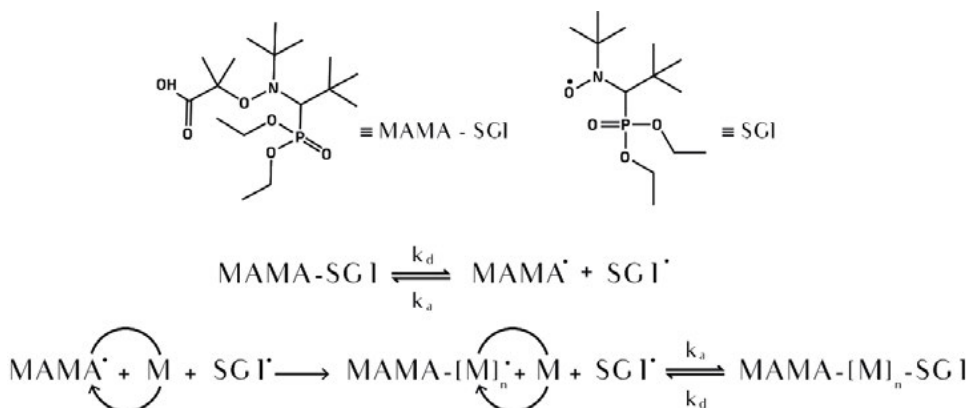


Figure 5.1. (top) Alkoxyamine initiator (MAMA-SG1) and the counter-radical nitroxide (SG1). (bottom) NMP reaction scheme for reversible dissociation/association of alkoxyamine equilibrium and controlled radical polymer propagation with a generic monomer (M).

Another challenging class of compounds to control is conjugated methacrylates (e.g., methyl methacrylate; MMA). In this case, the dormant/radical species equilibrium has a too high equilibrium rate constant ($K = k_d/k_a$), resulting in a large concentration of radical polymers in the solution. Consequently, self-termination and disproportionation (by β -H transfer, rate $\propto [\text{M}^\bullet]^{1/2}$) reactions are likely to occur, reducing the controlled nature of NMP and its overall conversion into the desired polymer chain^[19]. The problem was solved by using co-monomer additives (2-10% mol) to shift the equilibrium constant, thus boosting the controlled/living character of the polymerization. For MMA, suitable additives were found to be styrene or acrylonitrile, which favor the formation of a more stable additive-terminating chain, lowering the average equilibrium constant and, accordingly, the degree of self-termination reactions^[20,21]. The high dissociation rate constant displayed by the nitroxide-derived MAMA-SG1 needs to be counterbalanced by adding styrene, for example, and a slight amount of free radical SG1 (~10% of MAMA-SG1) further suppresses the dissociation rate. With this, it is possible to achieve a controlled/living polymerization of methacrylates. An additional benefit of NMP is its tolerance to water, which does not interfere with the radical reactions, and the low thermal energy required to (re)initiate the polymerization. However, the presence of molecular oxygen is still detrimental, as it acts as a radical scavenger. Hence, care must be taken to remove it beforehand.

In the present work, we used NMP to prepare a polymeric binder to be introduced into a conductive ink. The target compound is a polymethacrylate, and we are mainly interested in developing an amphiphilic copolymer, which ultimately increases the hydrophilicity of the printed-electrode surface, anticipating its application in the water

oxidation reaction. The electrode wettability is an important consideration when designing a water electrolyzer, as generated gaseous products (e.g., H₂ and O₂) must readily desorb from the surface to make the electroactive surface available for further turnover cycles. Hydrophilic materials promote this process due to the non-polar nature of the gases [22–24], other than promoting the diffusion of the aqueous electrolyte to the active sites in case of water oxidation. For this purpose, we synthesized a statistical (s) copolymer based on MMA, (hydroxyethyl)methacrylate (HEMA), and styrene (S), here abbreviated P(MMA-s-HEMA).

5.1.3 Screen-printing technology

Printed electronics can be manufactured mainly in two fashions: in a flatbed or a roll-to-roll process [25–27], with the latter having a higher possibility for up-scaling. Screen-printing techniques have gained greater attention over the last years thanks to the simple processability, the short production time, the possibility of having a flexible substrate, and the affordability of the method, especially for electronics, such as transistors and light-emitting diodes (LEDs), but also for electrodes, sensors, and solar cells [27–31].

Screen-printing is a simple and mature technology to create a thin film of a specific ink onto a substrate surface through a patterned mask (screen), which allows the ink to permeate and be deposited in a defined area. It is categorized as a contact method in printing technologies, meaning that the ink-containing support is brought in direct contact with the substrate [32,33]. In the screen-printing process, the ink transfer through the mask is achieved thanks to the ink thixotropic properties (primarily due to the binder component), which is the ability of a fluid to decrease its viscosity upon shear force application [34–36]. Thus, the ink drops across the fine mesh of the screen in a controlled fashion, exclusively when pressure is applied.

The ink usually contains at least three main components, active materials (conductive for electrodes; semiconductive for optical sensors; dielectric for capacitors), solvents, and polymers with resins. The resin and polymer serve as a binder for the active material in the finished film. The solvent is used to modify the ink viscosity, which is chosen to be compatible with the drying process and the binder's solubility.

Frequently, the thickness of the wet ink layer varies between tens to hundreds of micrometers, which is reduced once the ink is dried, a process achieved through solvent evaporation, UV curing, or oxidation. Such thicknesses have a positive effect on printed electronics, which helps to minimize sheet resistivity. Polymers are ideal candidates to be integrated into the ink composition, as they can have low surface energies [37,38] resulting in a formulation with reduced viscosity, granting the mesh not to be clogged

and leading to a smooth surface of the printed film ^[27,34]. Other parameters affecting the final result are the speed of the printing, angle, and geometry of the squeegee, mesh size, and material ^[27,28].

In the case of electronics, the conductive material, as electrodes, has to be chemically compatible with the solvent, the binder, and the substrate. However, it is also necessary to consider the final rheological parameters of the ink as viscosity, surface tension, and conductivity ^[27]. To date, most conductive inks for printed electronics rely on noble metal dispersed nanoparticles, such as gold, silver, and copper ^[25,32,37], but also graphitic materials have raised interest lately. Despite their extraordinary electrical properties, carbon nanotubes (CNTs) can easily affect the rheology of the ink that must be printed due to their nanocomposite nature ^[27,38]. The electrical resistivity of a material based on CNTs can increase compared to the one of a single CNT due to contact resistivity between adjacent CNTs and percolation-related issues. The conductive paths are parallel to the length of CNT, but random in-plane orientation makes them not perfectly aligned with the direction of the current flow ^[31,39].

Graphene and graphite represent a cheaper solution with fewer health-related risks. While graphene-based inks are more challenging to prepare, they exhibit excellent conductivity, reaching $\sim 881 \text{ S cm}^{-1}$ ^[40]. While graphite is a cheap alternative already used for sensors and electrodes, the conductivity of commercially available carbon inks typically does not exceed 20 S cm^{-1} ^[31,41].

In our work, we developed printed electrodes (PEs) based on graphite since such material has been studied for integration into screen-printing technologies. It is cheap, and the rheological properties of inks derived from it are well-known and more easily handled than CNTs. As the polymeric binder, a methacrylate backbone of P(MMA-*s*-HEMA) was chosen because this displays a strong affinity with perfluorinated membranes. These membranes (*e.g.*, Nafion[®]) are state-of-the-art in electrolyzer applications, especially in proton exchange membrane (PEM) configurations ^[42].

5.2 RESULTS AND DISCUSSION

5.2.1 Polymerization of the binder

The statistical copolymer P(MMA-*s*-HEMA) was synthesized by NMP, similarly to procedures reported elsewhere ^[43], using an initial molar monomer ratio of 7.0 : 2.1 : 0.9 of MMA, HEMA, and styrene, respectively. We aimed for a relatively short polymer length, and the theoretical number-averaged molecular weight (M_n) was targeted at

10000 g mol⁻¹. The moles of the initiator (n_i) were calculated according to the equation [20].

$$M_n = M_i + \left[\frac{m_{\text{mon}}}{n_i} \right] \times \text{conversion}$$

Where m_{mon} is the total mass of the monomers, and M_i and n_i are the molecular weight and number of moles, respectively, of the initiator. We assumed a monomer conversion equal to 50%, a good compromise between the final yield and the ease of product handling. It has been shown that for NMP homo-polymerization of MMA in the presence of 0.1 equivalents of styrene, a one-hour reaction is required to achieve 50% conversion [43].

An initial polymerization to P(MMA-s-HEMA) was conducted in bulk at 90 °C for an hour. The resulting material was purified and analyzed by size exclusion chromatography (SEC) (Figure 5.2, yellow trace). MAMA-SG1 was used as initiator and block builder, with an extra 10% mol excess of the free-radical nitroxide SG1 to control the reaction. Homopolymerization of HEMA was previously demonstrated to possess a non-controlled character [44]. Its enhanced reactivity explains the increased final molecular weight ($M_n = 18800$ g mol⁻¹ and weight-averaged molar mass, $M_w = 26400$ g mol⁻¹), as well as the relatively high dispersity ($\mathcal{D} = 1.40$) of P(MMA-s-HEMA) when compared to a PMMA control sample ($\mathcal{D} = 1.13$, $M_n = 8600$ g mol⁻¹, $M_w = 9800$ g mol⁻¹), obtained in the same conditions. Diluting the reaction mixture in DMF (30% w/w) was sufficient to improve \mathcal{D} of P(MMA-s-HEMA) to 1.24, and to restore the targeted molar mass, approaching the aimed value ($M_n = 12500$ g mol⁻¹, $M_w = 15500$ g mol⁻¹).

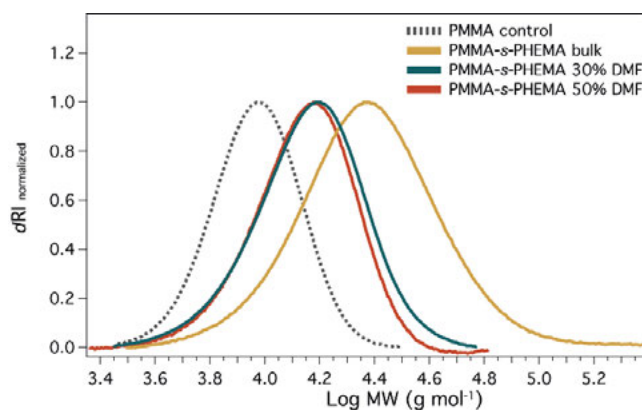


Figure 5.2. Size exclusion chromatography coupled refractive index (RI) detection of PMMA and P(MMA-s-HEMA) polymerized in bulk, and P(MMA-s-HEMA) polymerized in DMF solution. Column 30 °C, THF, standard polystyrene (PS).

Finally, P(MMA-s-HEMA) was analyzed by ^1H -NMR, and its co-monomer ratio was deduced by peak integration of aromatic, methoxy, and methylene ($-\text{CH}_2-\text{O}$) protons, resulting in a molar composition of styrene 15.0%; MMA 60.6%; HEMA 24.4% (Figure 5.3).

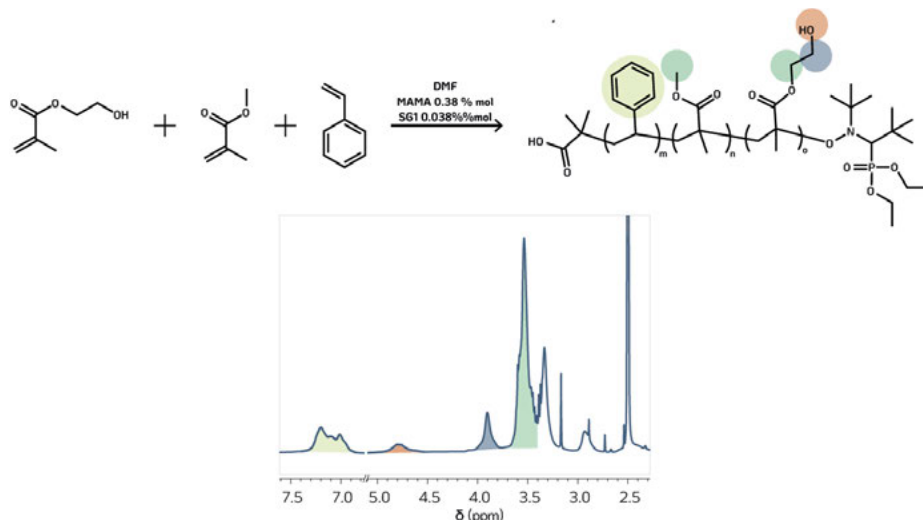
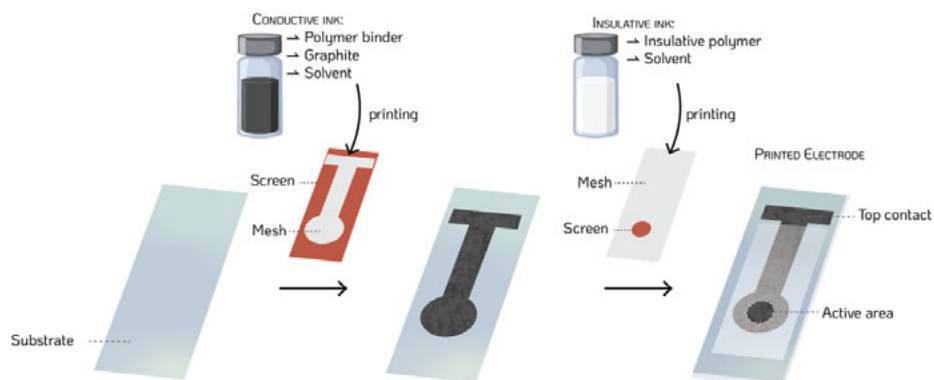


Figure 5.3. a) P(MMA-s-HEMA) synthetic reaction details. b) ^1H -NMR, in DMSO- d_6 , for comonomer composition determination.

5.2.2 Fabrication of printed electrodes (PEs)

The prepared amphiphilic polymer binder was introduced in the ink. The ink formulation consisted of 23% graphite as the conductive material, a blend of 7% P(MMA-s-HEMA) and 3% of commercially available MBM (poly(methyl methacrylate)-*b*-poly(1,4-butadiene)-*b*-poly(methyl methacrylate) triblock copolymer) as binder agents, and 67% of propylene glycol methyl ether acetate (PGMEA) as the binder solvent. The P(MMA-s-HEMA)/MBM blend was selected because of the well-established use of MBM in these applications, aiming to avoid too significant deviations from already observed behavior. An additional insulating layer was printed on top of the conductive film, confining the nominal electroactive area to 0.196 cm^2 ($\varnothing = 0.5\text{ cm}$) and leaving an uncovered area as the top contact. The insulating ink was prepared by mixing 63% high-impact polystyrene (HIPS) and 37% mesitylene (Scheme 5.2).

Immobilization of a molecular Cu-based WOC on printed electrodes through covalent interaction



Scheme 5.2. Schematic of printed electrode fabrication. Firstly, the conductive ink is printed onto the substrate; consequently, the insulative ink is printed on top of the previous layer(s), with a different screen designed to leave an exposed specific area.

The first set of PEs was manually printed (PE-1) in a flatbed screen-printing machine and used to assess whether or not the amphiphilic P(MMA-*s*-HEMA) increased surface wettability. The water contact angle on the electrode surface was measured to evaluate the hydrophilicity of the carbon-based electrode (Table 5.1). To reference the results, we printed similar electrodes, replacing P(MMA-*s*-HEMA) with solely MBM, a completely hydrophobic polymer, similar to what is conventionally used in printed electronics. Both electrodes showed a similar contact angle, around 126°, suggesting that no gain in hydrophilicity was obtained from incorporating the HEMA units in the binder. However, drop-casting of polar solvents onto the surface plays a vital role in revealing the hydrophilic property. A series of solvents were cast over different electrodes, and after their evaporation, water contact angles were determined, summarized in Table 5.1. As the solvent polarity increased, the contact angle of the control electrodes decreased progressively, reaching a value of 108° when DMF was used.

When P(MMA-*s*-HEMA)-based films were analyzed, we observed a substantial deviation from the control trend when methanol was used. The water contact angle drops to 67.5° indicating a significant increase in the surface hydrophilicity. The considerable variation can be explained by the partial dissolution of HEMA co-monomer domains along the polymer chain, which drives their segregation at the surface. Once the solvent is evaporated, the surface morphology remains, leaving the alcohol chains of HEMA towards the top surface, improving the overall wettability.

<i>Electrode</i>	<i>pristine</i>	<i>THF</i>	<i>MeOH</i>	<i>DMF</i>
<i>Control</i>	126.2°	118.9°	112.8°	108.1°
<i>PE – 1*</i>	126.8°	126.2°	67.5°	102.6°

Table 5.1. Water contact angles of MBM-based electrode (control) and P(MMA-s-HEMA)/MBM-based electrodes (PEs-1) upon solvent casting (averaged angles).

* P(MMA-s-HEMA):MBM ratio 7:3.

Besides PEs-1, which were manually printed, we prepared other electrodes consisting of the same ink but processed with a semi-automatic (Digital Electric Flat Screen Printer AT-60PD from ATMA) flatbed machine (PEs-2). By doing so, we could evaluate the electrical properties of the printed electrodes more reproducibly, as the thickness and homogeneity of the films are a result of the applied pressure onto the squeegee and the speed of its motion, which are poorly controlled manually. Finally, we also manufactured printed electrodes using a commercially available ink (SunChemical® C2030519P4; PEs-3) and used it as a comparison for the performance of our ink.

The electrodes were analyzed by scanning electrode microscopy (SEM), inspecting both the top front side and the cross-section of the electrochemically active area (Figure 5.4). The analysis shows that PEs-1 and PEs-2 have similar morphologies, characterized by irregular and rough surfaces, due to the nature of the graphite particles. The inhomogeneity is also reflected between the film layers, where small pockets are observed. On the contrary, PEs-3 have a much smoother surface, and the cross-section is more homogenous and compact. We expect this to influence the electrical properties of the devices, having PEs-3 less resistive elements than PEs-1 and PEs-2.

We tested the conductivity of the sets of PEs by four-point probe measurements with equidistant probes in a linear fashion. A summary of the deduced electrical properties is shown in Table 5.2, reporting the substrates they were printed on, the number of printed layers, and the final thickness of the conductive films. The conductivity was determined according to the equation below, applicable for samples thinner than half the spacing between the probes, in our case ≤ 0.5 cm ^[45]:

$$\sigma = \frac{\ln(2)}{\pi t} \frac{i}{V}$$

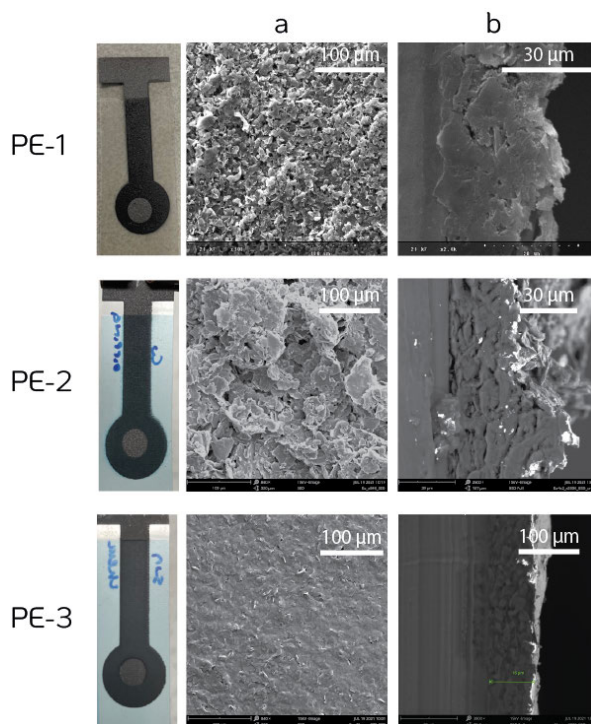


Figure 5.4. SEM images of the three sets of PEs studied. a) top view and b) cross-section of electroactive area.

Here t is the thickness of the layer, i is the applied current over the two outer probes, and V is the recorded potential drop over the two inner probes. Considering the thickness of each PE, the bulk resistivity ($\rho = \sigma^{-1}$) calculated reveals how the PE-3 series displays the lowest resistivity ($\rho_{\text{PE-3}} = 1.4 \text{ m}\Omega \text{ m}$). Thus, the commercial ink combined with the semi-automatic processing method results in the best electrodes in terms of conductivity. Regarding our prepared ink-based electrodes, we observed that PE-2 not only has a lower bulk resistivity compared to PE-1 ($\rho_{\text{PE-1}} = 3.9 \text{ m}\Omega \text{ m}$; $\rho_{\text{PE-2}} = 2.5 \text{ m}\Omega \text{ m}$) but also its fabrication seems more reproducible, as the standard deviations in Table 5.2 show. We concluded that the printing method had the most significant impact on the PEs development and their performances. The controlled and automatized screen printing provides more uniform and less resistive electrodes. However, the ink formulation plays a role, as the commercial ink-based PE-3 displays a higher conductivity than the equally fabricated PE-2.

<i>Property</i>	<i>PE - 1</i>	<i>PE - 2</i>	<i>PE - 3</i>
<i>Substrate</i>	PVC/Nafion	PET	PET
<i>Layers</i>	3 (1 x 3)	8 (4 x 2)	2 (2 x 1)
<i>Thickness (μm)</i>	13.5 ± 1.8	70.8 ± 8.5	17.9 ± 0.5
<i>Resistivity ($\text{m}\Omega\text{ m}$)</i>	3.9 ± 1.1	2.5 ± 0.3	1.4 ± 0.1
<i>Conductivity (S cm^{-1})</i>	2.7 ± 0.6	4.1 ± 0.6	7.2 ± 0.5

Table 5.2. Four-probe conductivity measurements of PEs. The layers entry describes the number of prints for wet film depositions between the drying process (e.g., 4 x 2 is two wet depositions repeated four times after drying). Thickness considers only the conductive film.

The printed electrodes were tested electrochemically by cyclic voltammetry in a 0.3 M KNO_3 solution. Figure 5.5 shows the cyclic voltammograms (CVs) of the respective PEs as working electrodes, employing a platinum disk as the counter electrode and Ag/AgCl as the reference electrode. The electrolyte was purged with N_2 to avoid oxygen reduction at the electrodes. Among the investigated electrodes, we noticed that PEs-1 (Figure 5.5a) had the more unpredictable behavior, changing considerably between different samples. Those are the ones that also show a diagonal-like CV shape, further confirming the high resistivity that manually printed electrodes possess.

Knowing that the double layer capacitance (C_{dl}) (F) can be expressed by:

$$C_{\text{dl}} = \frac{i}{\nu}$$

Where i is the non-Faradaic current (in A), and ν is the scan rate (in V s^{-1}). We can also define the electrochemical active surface area (ECSA) and the roughness factor (Rf) as follows:

$$\text{ECSA} = \frac{C_{\text{dl}}}{C_s}$$

$$Rf = \frac{\text{ECSA}}{A}$$

Where C_s is the specific capacitance of a given material (in F m^{-2}), and A is the nominal electrode area (in m^2).

For PE-1 and PE-2, the capacitive (non-Faradaic) current varies little in the window -0.2 - 0.6 V (vs. Ag/AgCl) compared to PE-3 when the scan rate, ν , changes. This suggests C_{dl} is smaller for the former electrodes, and assuming the same C_s for carbon-based electrodes, PE-1 and PE-2 would result in the smallest Rf compared to PE-3. The

observation diverges from the microscopy images shown above, where PE-1 and PE-2 show an evident greater roughness.

To better understand these contradictory results, we evaluated the ECSA by using the Randles – Ševčík equation through analysis of the Faradaic response of a well-established electroactive species for which we used the ferrocyanide-ferricyanide redox couple ($[\text{Fe}(\text{CN})_6]^{4-/3-}$). We collected CVs at different $[\text{Fe}(\text{CN})_6]^{3-/4-}$ concentrations in 0.3 M KNO_3 using the different sets of printed electrodes (Figure 5.6), and adopting a diffusion coefficient (D_0) of $7.09 \times 10^{-6} \text{ cm}^2 \text{ s}^{-1}$, as was reported in KNO_3 electrolyte solutions^[46].

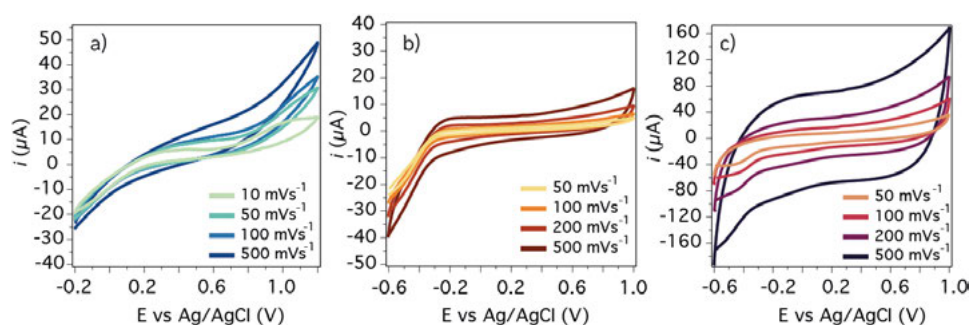


Figure 5.5. CV of a) PE-1 b) PE-2 c) PE-3 in 0.3 M KNO_3 at different scan rates. AgCl: reference | Pt: counter | PEs: working electrode.

The voltammograms of the ferro/ferri-cyanide redox couple show a $E_{1/2} = 260 \text{ mV}$ ($\Delta E_p = 607 \text{ mV}$), $E_{1/2} = 236 \text{ mV}$ ($\Delta E_p = 537 \text{ mV}$), and $E_{1/2} = 239 \text{ mV}$ ($\Delta E_p = 364 \text{ mV}$), respectively for PE-1, PE-2, and PE-3. The peak-to-peak separation (ΔE_p) reduces along the series, indicating a progressive enhancement of the electrode kinetics. Since the mass transport of the electroactive species remains unaltered (same diffusion coefficient, no mesoporous structure), it is ascribed to the standard heterogeneous electron transfer rate constant, which improves from PE-1, via PE-2, to PE-3. The difference between PE-1 and PE-2 can be seen as marginal, but it already shows faster kinetics, which can be due to the higher reproducibility and quality of the semi-automatic fabricated PEs. Finally, if we compare PE-2 with the commercial ink-based PE-3, the peak separation is further reduced, supporting the previous results of overall more conductive electrodes.

The ECSA was determined using the Randles – Ševčík relationship $i_p = 2.69 \times 10^5 A D_0^{1/2} C \nu^{1/2}$, in which, A is the area of the electrode (in cm^2) and C is the concentration (in mol cm^{-3}). By plotting i_p (anodic and cathodic in A) versus the $[\text{Fe}(\text{CN})_6]^{4-/3-}$ concentration (Figure 5.6d), the active area can be determined and was found to be 0.154, 0.162, and 0.180 cm^2 for PE-1, PE-2, and PE-3, respectively.

Considering that the nominal area is 0.196 cm^2 for every electrode, and the SEM images show higher surface roughness for PE-1 and PE-2 than for PE-3, these results initially seem counterintuitive.

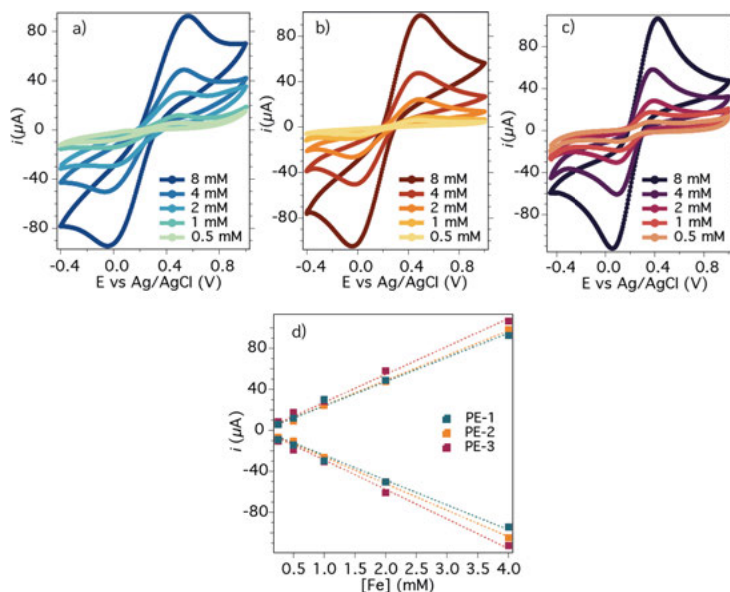


Figure 5.6. CVs of different concentrations of $[\text{Fe}(\text{CN})_6]^{4-}/[\text{Fe}(\text{CN})_6]^{3-}$ in 0.3 M KNO_3 at 50 mV s^{-1} , using a) PE-1; b) PE-2; c) PE-3. ($[\text{Fe}(\text{CN})_6]^{4-}/[\text{Fe}(\text{CN})_6]^{3-}$ ratio 1:1). d) Randles – Ševčík plot for ECSA evaluation.

However, we may rationalize the results with the electrode ink formulation. PE-1 and PE-2 have a solid content of insulating binder of around 30%, which will not contribute to the passage of any electrical charge, eventually resulting in a reduced ECSA. However, it remains a hypothesis, as we do not know the composition of the commercial ink, but we assume a reduced binder content gives better conductivity in favor of a higher load of conductive material. In the literature, some procedures are present to enhance the electrochemical performances of screen-printed PEs. Soaking the electrodes in DMF for chemical etching has been shown to remove polymer binders blocking the electrode surface, possibly increasing the graphite exposure ^[47]. Electrochemical pre-treatment of the electrodes with short anodization (3 min $1.5\text{--}2 \text{ V}$) has been described to increase the surface functionalities and roughness or to remove surface contaminants too ^[48].

On the contrary, given the much smoother surface of PE-3, its ECSA approaches the nominal area but not entirely, indicating that the binder might cause the reduced

value, but in a smaller magnitude. This would also explain the higher capacitive current obtained as a function of ν in the case of PE-3.

Overall, we formulated and fabricated PEs displaying conductivity values similar to the electrodes printed from a commercial ink source. Additionally, we incorporated an amphiphilic polymer (P(MMA-*s*-HEMA)) in the ink blend, which allows us to control the wettability of the electrode surface by simply solvent casting. This might increase the anode performance since the delivery of substrate (water) and its mass transport will be favored by the hydrophilic environment, and so will the desorption of the oxygen produced by the catalyst. Having prepared the solid electrodes, the following stages are dedicated to preparing a suitable macrocycle ligand to be anchored on the PEs and the consequent activation towards water oxidation exploiting copper as the metal center.

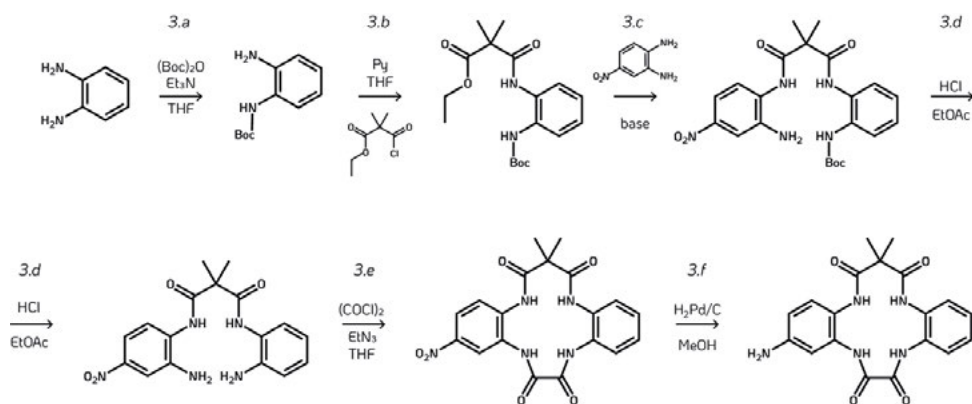
5.2.3 dNH₂Mac synthesis and covalent grafting

To accomplish the goal of surface grafting the molecular copper-based water oxidation catalyst (NMe₄)₂[CuMac], we first designed a synthesis route to the macrocycle ligand bearing a single amino functional group (mNH₂Mac, Scheme 5.3). The mono functionality could, in principle, be introduced by an asymmetric malonyl bridging ligand (Step 3.b), which would allow, in a step-wise fashion, the introduction of a second 1,2-phenylenediamine bearing a nitro group in the para position (Step 3.c). After completing the macrocycle, the nitro group would be converted into the amine (Step 3.f). This group would serve as an anchoring group to graft the catalyst onto the PEs by transforming it into a diazonium salt and then electro-grafting in situ onto the carbon-based PEs.

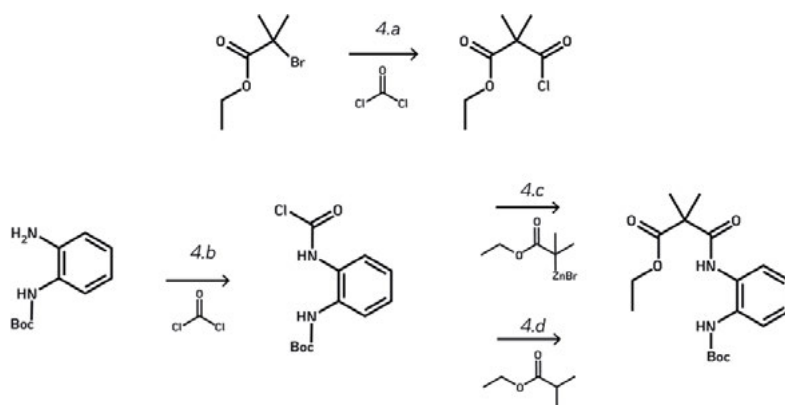
Several attempts have been made to synthesize the asymmetric macrocycle by synthesizing ethyl 3-chloro-2,2-dimethyl-3-oxopropanoate starting from ethyl 2-bromoisobutyrate (Scheme 5.4, Step 3.a) or by extending the bridge step-wise, first with one carbon and second with a carbanion source (Steps 4.b, 4.c, and 4.d). Unfortunately, neither of these attempts was successful, and the proposed sequence in Scheme 5.3 failed at step 3.b.

To simplify the synthesis, the target ligand was changed to bear two amino groups (dNH₂Mac), which removes the necessity to build the macrocycle asymmetrically. The molecule was obtained following a similar synthetic pathway previously reported ^[49], adopting a change in the starting material and hydrogenating the compound to yield the dNH₂Mac, **5** (Scheme 5.5)

5.

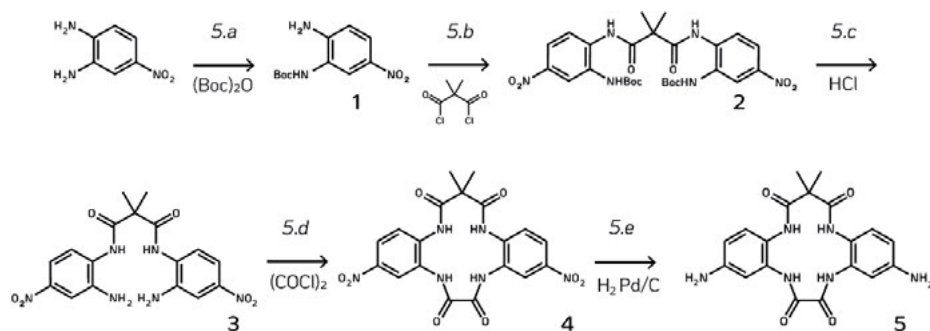


Scheme 5.3. Proposed synthesis of an asymmetric mono-amino functionalized macrocycle ligand (mNH₂Mac).



Scheme 5.4. Attempted reactions for asymmetric dimethyl malonyl bridging ligand. 4.a) COCl₂ 1.5 eq, Zn, MeOAc. 4.b) COCl₂ 1.5 eq, Et₃N 2 eq, toluene 30 min. 4.c) THF, LDA, -78 °C, 30 min. 4.d) KtBuO, 0 °C, 30 min.

Immobilization of a molecular Cu-based WOC on printed electrodes through covalent interaction



Scheme 5.5. Synthetic route for dNH₂Mac ligand. 5.a) Di-*tert*-butyl dicarbonate ((Boc)₂O, 1 eq), Et₃N, THF. Inert atmosphere, 0 °C to room temperature, overnight, 64%. 5.b) Dimethylmalonyl dichloride (0.5 eq), pyridine, THF, inert atmosphere, overnight, 96%. 5.c) EtOAc/HCl, 2 h, 56%. 5.d) Oxalyl chloride, Et₃N, THF, inert atmosphere, 38%. 5.e) H₂ 40 bar, Pd/C 10% w/w, MeOH 70 °C, 24 h, 69%.

5.2.4 Novel anode material stability and activity

The immobilization was first studied on glassy carbon (GC) electrodes. For this purpose, dNH₂Mac was dissolved in the minimum amount of trifluoroethanol (TFE) and mixed with an aqueous HCl (0.5 M) solution (TFE:HCl 1:10). To generate the diazonium salt of dNH₂Mac, 2.5 eq. of NaNO₂ were added, and the mixture was stirred at 0 °C for 30 min, after which an excess of NaBF₄ was also introduced to exchange the cation with the more stable tetrafluoroborate. The diazotization was repeated in the respective deuterated solvents (TFE-*d*₃ and DCl/D₂O), and ¹H-NMR analysis (Figure 5.7) confirmed the conversion of both amino groups due to the absence of Ar-NH₂ ($\delta \sim 5.2$ ppm). Then, cyclic voltammetry was used to induce the diazonium reduction and to graft it onto the electrode.

In the CV, an irreversible broad reductive peak was observed at around 0 V vs. AgCl/Ag (Figure 5.8), which progressively decreased in intensity as the potential was swept back and forth until no trace of the signal was detectable. This behavior is consistent with diazonium electroreduction reported in the literature ^[2,50]. The calculated surface coverage (Γ) estimated by the peak integration, assuming a one-electron process, results in $\Gamma = 547.9 \text{ nmol cm}^{-2}$, which is considerably higher than what would be expected for a monolayer coverage, which usually displays $\Gamma = 1\text{--}2 \text{ nmol cm}^{-2}$ for GC surfaces ^[9,51]. Possibly, a multilayer is grown, facilitated by the presence of the second amino group on the macrocyclic ligand, giving the possibility for C-C bond formation.

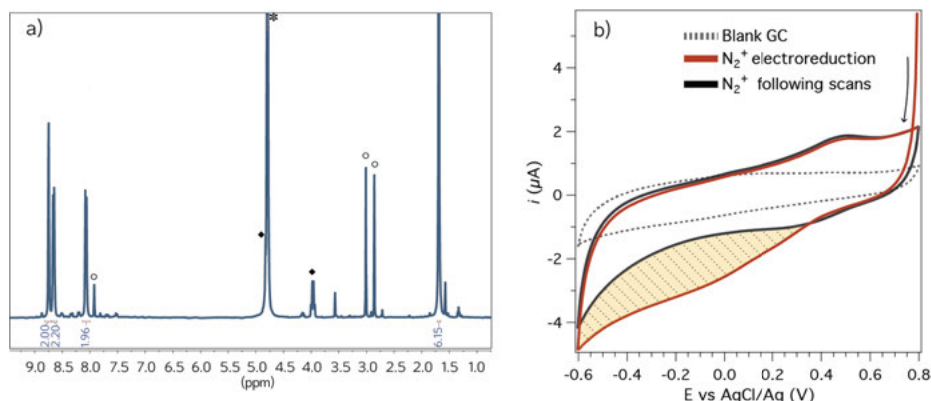


Figure 5.7. a) ^1H -NMR of the diazotization reaction mixture in ($\text{TFE}-d_3:\text{D}_2\text{O}/\text{DCI}$ 1:10). dNH_2Mac 1 eq., NaNO_2 2.5 eq., NaBF_4 5.0 eq. Residual solvent peaks: * H_2O , ♦ TFE, and ○ DMF. b) CV of dNH_2Mac 1 mM in $\text{TFE}:\text{HCl}$ 0.5 M (1:10), NaNO_2 2.5 eq., NaBF_4 5 eq. ν 50 mV/s. Reference Ag/AgCl ; counter electrode Pt disk; working electrode GC disk.

We then proceeded to the metal complexation of the anchored ligand system. The modified electrodes were first rinsed with TFE and water and then placed in a 40 mM aqueous solution of Me_4NOH for 10 min under stirring. This initial step is to deprotonate the amide groups responsible for coordinating the metal center. Subsequently, the electrodes were soaked in an aqueous solution of $\text{Cu}(\text{ClO}_4)_2$ (10 mM) for 10 min. The modified electrodes were then rinsed with more water.

CV analysis revealed the presence of two redox processes (Figure 5.9) with $E'_{1/2} = -0.01$ V and $E''_{1/2} = 0.31$ V vs. Ag/AgCl . Technically, only one molecular redox process is expected due to the $\text{Cu}^{\text{III}}/\text{Cu}^{\text{II}}$ redox couple, similar to the behavior of the homogeneous $(\text{NMe}_4)_2[\text{CuMac}]$. The two distinctive waves might arise from a different coordination environment of some of the complexes. Upon diazonium reduction, if the newly generated radical does not react with the surface, it will likely react with water, yielding the respective phenol. A hydroxyl group on the ligand system will affect the electron density of the complex, with consequences on the oxidation potential. Alternatively, the presence of adsorbed inorganic copper, not coordinated within the complex, can explain the additional redox process.

During the first sweep, a catalytic wave was observed at $E_p = 1.07$ V vs. Ag/AgCl . However, the catalytic wave fades during the second scan, producing a current negligible higher than the signal of a clean GC electrode (Figure 5.9a). Figure 5.9b, shows CVs in which the potential window was progressively increased, trying to assess the cause of the poor activity as a consequence of decomposition/deactivation at high

anodic potentials. We did not find any significant drop in the current as the potential was increased stepwise, but in every subsequent scan, the current reached over the potential range that was already covered in the previous scan and was reduced. This points to a deactivation process that depends on the applied potential.

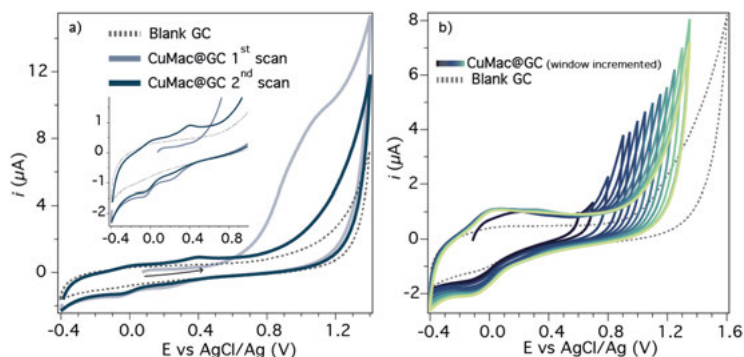


Figure 5.9. CV of modified electrode CuMac@GC in phosphate buffer solution 0.1 M, pH 7.1. a) first two scans of a freshly prepared electrode. b) CV of the first reversible wave. In each subsequent cycle, the potential window is anodically increased. Reference Ag/AgCl; counter electrode Pt disk; working electrode modified CuMac@GC disk.

A control CV run in 2 mM $\text{Cu}(\text{ClO}_4)_2$ exhibits a redox event at $E_{1/2} = -0.09$ V vs. Ag/AgCl, relatively close to the potential of one of the processes experienced in the modified CuMac@GC electrode (Figure 5.10). We also performed the so-called "rinse test," in which the electrode, after CV in $\text{Cu}(\text{ClO}_4)_2$ solution, was placed in a fresh electrolyte, after abundant rinsing with water, and analyzed. The features previously observed were retained, confirming that inorganic copper species can be adsorbed on the GC surface for both controls. However, the peaks are sharper than those shown in Figure 3.9, consistent with an oxidation/reduction of a species adsorbed on a surface.

Carbon-based PEs were fabricated by screen printing. The inks were made using graphite and an amphiphilic polymer to control the surface wettability of the electrodes. The electrochemical and electrical proprieties of the PEs were successfully characterized and compared with commercial ink, revealing that the latter has slightly better electrical performance and provides a slightly higher electroactive area. The customized inks also show good characteristics, which all fall within the specifications for their use in electrolyzers.

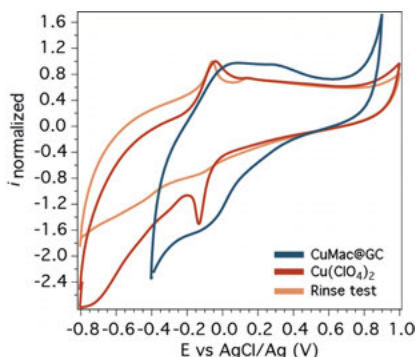


Figure 5.10. CV in 2 mM of $\text{Cu}(\text{ClO}_4)_2$ and the relative "rinse test" in phosphate buffer 0.1 M pH 7.0, compared to the CV obtained from CuMac@GC. Reference Ag/AgCl; counter electrode Pt disk; working electrode GC disk.

5.3 CONCLUSIONS

After unsuccessful attempts to synthesize the mono-functionalized mNH_2Mac ligand for grafting the PEs with a molecular catalyst, the initial design was modified to a symmetric, bi-functionalized macrocycle ($\text{dNH}_2\text{-Mac}$). dNH_2Mac was successfully synthesized in a five-step reaction sequence. The grafting of $\text{dNH}_2\text{-Mac}$ by diazonium electro-reduction was performed on a GC electrode. Upon copper complexation, the water oxidation of the new anode material was evaluated by CV. The activity, however, only marginally increased compared to a blank GC electrode.

5.4 EXPERIMENTAL METHODS

Materials: Commercial chemicals were purchased by Sigma-Aldrich, TCI, or Alfa Aesar and used without further purification. Dry and oxygen-free solvents were provided by a MBRAUN SPS-800 solvent purification system. Aqueous basic buffer solutions at several pH values were prepared using specific concentrations of monobasic and dibasic phosphate salts such that the final buffer concentration was 0.1 M. Arkema kindly provided MAMA.

Materials characterization: ^1H and ^{13}C NMR spectra were obtained on a 400 MHz Bruker Avance III spectrometer. All the measurements were performed at room temperature in

Immobilization of a molecular Cu-based WOC on printed electrodes through covalent interaction

deuterated DMSO if not stated otherwise. Chemical shifts (δ) are reported in part per million (ppm).

Mass spectrometry was measured on a matrix-assisted laser desorption ionization-time of flight (MALDI-TOF) Bruker Autoflex Speed spectrometer.

Size exclusion chromatography (SEC) Size exclusion chromatography (SEC) was performed to determine the molar mass and molar mass distribution of the polymers using THF as eluent with a flow rate of 1.0 mL min^{-1} at 30°C . The SEC is equipped with a Viscotek VE 5200 automatic injector, a pre-column and two columns (Styragels HR 5E and 4E (7.8 ft, 300 mm)), and four detectors: a UV–visible spectrophotometer (Viscotek VE 3210), a Multiangle Light Scattering detector (Wyatt Heleos II), a viscometer (Wyatt Viscostar II), and a refractive index detector (Viscotek VE 3580). To determine the molecular weight (M_w) and dispersity of the polymers, a refractive index detector and polystyrene standards were used.

Thermal gravimetric analysis (TGA) was performed on a TGA Q50, TA Instruments at a heating rate of $10^\circ\text{C min}^{-1}$ under nitrogen.

Screen-printed electrodes fabrication: PEs-1 were manufactured on a CPL Fabbrika manual Screen Printer press mod Susa 220 V. PEs-2 and PEs-3 were fabricated on a semi-automatic digital electric flat screen printer AT-60PD from ATMA. The electrodes ink for PEs-1 and PEs-2 consisted of graphite (microcrystal grade 14736, Alfa Aesar), P(MMA-s-HEMA), MBM (Kurarity P(MMA-*b*-nBuA-*b*-MMA), $M_n = 114000 \text{ g mol}^{-1}$ $\bar{D} = 1.068$) and PGMEA as solvent. For PEs-3, a commercial ink SunChemical® C2030519P4 was used.

Screen-printed electrodes characterization: Water contact angle measurements were recorded on a contact angle meter (GBX) equipped with a video camera and Windrop++ software. For prior solvent treatment, $15 \mu\text{L}$ of different solvents were cast onto the PEs, and upon evaporation, $5 \mu\text{L}$ of water was placed on the electrode's surface. Images were then taken with the camera, and the angles were calculated by Windrop++.

SEM analyses of gold-coated electrodes were carried out on a Phenom ProX, applying an acceleration voltage of 10 kV .

Electrochemical experiments (CVs and DPs) were measured on a Metrohm Autolab PGSTA30 potentiostat. Ag/AgCl (KCl 3M) electrode was used as a reference, while the Pt disk was used as a counter electrode. The PEs, with a nominal exposed area of 0.196 cm^2 , were used as working electrodes; alternatively, GC disk of 0.126 cm^2 was employed when expressly stated.

Synthetic Details

P(MMA-s-HEMA)

The alkoxyamine block-builder (MAMA-SG1; 0.00715 eq. , 1372 mg , 3.60 mmol) and the nitroxide free-radical (SG1; 0.000715 eq. , 125.3 mg , 0.42 mmol) were weighed and placed in a round bottom flask. Consequently, methyl methacrylate (MMA; 1 eq. , 50.0 g , 0.50 mol), hydroxyethyl methacrylate (HEMA; 0.3 eq. , 19.61 g , 0.15 mol), and styrene (S; 0.13 eq. , 6.96 g , 0.07 mol) were also introduced and dissolved in DMF (30 mL). The mixture was then sealed and purged with N_2 for 20 min . The sealed flask was then transferred to an oil bath pre-heated at 90°C , and the reaction mixture was stirred for 1 h . The resulting polymer was precipitated in abundant Et_2O with vigorous stirring. The polymer was then collected and redissolved in THF overnight, and the precipitation process was repeated two more times to remove traces of

unreacted monomers and possible remaining solvent. P(MMA-*s*-HEMA) was filtered over a Büchner funnel and dried in a vacuum oven at 40 °C overnight.

Yield 47 %

GPC: RI detector $M_n = 12500 \text{ g mol}^{-1}$, $M_w = 15500 \text{ g mol}^{-1}$, $\bar{D} = 1.24$. Multiangle laser scattering (MALS) $M = 17850 \text{ g mol}^{-1}$.

T_g : 96.2 °C

1

A dry two-necked-round bottom flask was charged with *p*-nitro-*o*-phenylene diamine (2500.0 mg, 19.59 mmol) and triethylamine (1.75 mL, 19.59 mmol) under N₂. Dry THF (250 mL) was added to the flask. Di-*tert*-butyl dicarbonate (3562.9 mg, 19.59 mmol) was solubilized in THF (9.8 mL) to give 2 M solution, which was added dropwise to the reaction mixture at 0 °C. The reaction mixture was then stirred at room temperature overnight while maintaining an inert atmosphere. Afterward, an excess of di-*tert*-butyl dicarbonate (2137.8 mg, 9.80 mmol) was first dissolved in THF (5 mL) and introduced to the mixture, stirring at 50 °C for 24 h. The solvent was evaporated, and the crude product was purified by two recrystallizations from ethanol/heptane.

Yield: 3191.7 mg; 12.61 mmol; 64 % (70 ± 6 %)

¹H NMR (400 MHz, DMSO-*d*₆) δ : 8.56 (s, 1H), 8.35 – 8.22 (m, 1H), 7.79 (dd, $J = 9.0, 2.7$ Hz, 1H), 6.73 (d, $J = 9.1$ Hz, 1H), 6.46 (s, 2H), 1.49 (s, 9H).

¹³C NMR (101 MHz, DMSO-*d*₆) δ : 153.36, 147.79, 135.68, 122.27, 121.65, 119.17, 113.45, 79.59, 28.09.

2

A three-necked flask was charged with **1** (2068.3 mg, 8.17 mmol) under N₂ and dissolved in dry THF (120 mL). Pyridine (0.694 mL, 8.58 mmol) was added to the mixture. Then dimethylmalonyl dichloride (0.540 mL, 4.09 mmol) was solubilized in anhydrous THF (10 mL) and added via dropping funnel to the reaction mixture at a rate of ca. 0.5 drops s⁻¹, and the mixture was stirred for 4 h. A white precipitate formed during the reaction was filtered off, and the solvent from the mixture was removed under vacuum. As the product retained a considerable amount of solvent, the compound was dried with an oil pump overnight.

Yield: 2368.2 mg; 3.93 mmol; 96 % (82 ± 11 %)

¹H NMR (399 MHz, DMSO-*d*₆) δ : 9.69 (s, 2H), 9.07 (s, 2H), 8.43 (t, $J = 1.7$ Hz, 2H), 8.00 (dd, $J = 8.0, 2.3$ Hz, 2H), 7.87 (d, $J = 8.9$ Hz, 2H), 1.61 (s, 6H), 1.43 (s, 18H).

¹³C NMR (100 MHz, DMSO-*d*₆) δ : 172.39, 153.28, 144.11, 135.53, 132.09, 125.97, 119.02, 118.13, 80.43, 51.54, 27.90, 23.23.

3

2 (2368.2 mg, 3.93 mmol) was placed in a round bottom flask and dissolved in rapidly stirred EtOAc (200 mL). Then concentrated HCl (60 mL) was added dropwise to give a biphasic reaction mixture (ca. 3.0 M HCl in the volume of the biphasic mixture). After 10 min of stirring, ice-cold NaOH (~ 5 M) was added to neutralize the acid, and the pH was brought to 10. During this process, the mixture turned red, only to slowly turn yellow. The aqueous layer was separated, and the target compound was extracted with a DCM:THF (3:1) mixture in three steps (~ 100 mL

each). Then, the mixture was concentrated under reduced pressure, and **3** was precipitated in MeCN/Et₂O and filtered.

Yield: 897.3 mg; 2.23 mmol; 57 % (74 ± 13 %)

¹H NMR (400 MHz, DMSO-*d*₆) δ : 9.35 (s, 2H), 7.61 (d, *J* = 2.6 Hz, 2H), 7.42 (dd, *J* = 8.6, 2.6 Hz, 2H), 7.34 (d, *J* = 8.6 Hz, 2H), 5.56 (s, 4H), 1.60 (s, 6H).

¹³C NMR (100 MHz, DMSO-*d*₆) δ : 173.21, 146.26, 144.68, 129.38, 127.73, 111.06, 109.75, 51.73, 23.79.

4

The macrocyclic ligand precursor **3** (502.6 mg, 1.24 mmol) was added to anhydrous THF (700 mL) containing triethylamine (0.39 mL; 2.76 mmol) in a dried two-necked round bottom flask under N₂. The mixture was cooled to 0 °C. Oxalyl dichloride 2 M in THF (0.62 mL, 1.24 mmol) was added dropwise to the reaction vessel. A white precipitate was formed. The reaction was stirred overnight, leaving it warm to room temperature. The mixture was then filtered, and the solvent was evaporated under vacuum. The crude was sonicated in Et₂O for 10 min and filtered over a sintered glass filter. The solid was washed with a MeCN/*i*-PrOH mixture (1:1) to obtain a chalky white solid.

Yield: 217.7 mg; 0.477 mmol; 38.5 % (32 ± 6 %)

¹H NMR (399 MHz, DMSO-*d*₆) δ : 10.25 (d, *J* = 69.5 Hz, 4H), 8.29 (d, *J* = 56.1 Hz, 4H), 7.92 – 7.56 (m, 2H), 1.58 (s, 6H).

¹³C NMR (100 MHz, DMSO-*d*₆) δ : 172.66, 162.51, 145.01, 138.68, 132.04, 127.27, 122.29, 121.99, 51.50, 24.12.

5

The hydrogenator reactor was charged with **4** (329.7 mg, 0.72 mmol), 10% Pd/C (33.2 mg), and MeOH (50 mL). The reactor was then assembled, and 40 bars of H₂ were applied, stirring the mixture at 70 °C overnight. The slurry was filtered over celite, washing it thoroughly with MeOH, and the target compound was collected using the minimum amount of DMF. The solvent was evaporated under vacuum at 70 °C, leaving a yellowish powder, which was further dried overnight under vacuum.

Yield: 198.9 mg; 0.502 mmol; 69.7 % (68 ± 8 %)

¹H NMR (400 MHz, DMSO-*d*₆) δ : 9.21 (s, 2H), 9.04 (s, 2H), 6.89 (d, *J* = 8.6 Hz, 4H), 6.41 (dd, *J* = 8.5, 2.5 Hz, 2H), 5.27 (s, 4H), 1.47 (s, 6H).

¹³C NMR (101 MHz, DMSO-*d*₆) δ : 173.48, 161.91, 148.01, 132.89, 128.45, 118.49, 111.46, 109.84, 51.56, 23.52.

MALDI/TOF (positive mode) *m/z*: exp. 396.2 (dNH₂Mac); ([C₁₉H₂₀N₆O₄]) *m/z*: cal. 396.2)

5.5 REFERENCES

- [1] B. Zhang, L. Sun, *Chem. Soc. Rev.* **2019**, 48, 7, 2216–2264.
- [2] D. Hetemi, V. Noël, J. Pinson, *Biosensors* **2020**, 10, 1, 4.
- [3] A. P. Colleville, R. A. J. Horan, N. C. O. Tomkinson, *Org. Process Res. Dev.* **2014**, 18, 9, 1128–1136.
- [4] V. Q. Nguyen, X. Sun, F. Lafolet, J.-F. Audibert, F. Miomandre, G. Lemerrier, F. Loiseau, J.-C. Lacroix, *J. Am. Chem. Soc.* **2016**, 138, 30, 9381–9384.
- [5] P. Allongue, M. Delamar, B. Desbat, O. Fagebaume, R. Hitmi, J. Pinson, J.-M. Savéant, *J. Am. Chem. Soc.* **1997**, 119, 1, 201–207.
- [6] L. Rotundo, J. Filippi, R. Gobetto, H. A. Miller, R. Rocca, C. Nervi, F. Vizza, *Chem. Comm.* **2019**, 55, 6, 775–777.
- [7] C. Henry De Villeneuve, J. Pinson, M. C. Bernard, P. Allongue, *J. Phys. Chem. B* **1997**, 101, 2415–2420.
- [8] M. C. Bernard, A. Chaussé, E. Cabet-Deliry, M. M. Chehimi, J. Pinson, F. Podvorica, C. Vautrin-Ui, *Chem. Mater.* **2003**, 15, 18, 3450–3462.
- [9] A. Adenier, M. C. Bernard, M. M. Chehimi, E. Cabet-Deliry, B. Desbat, O. Fagebaume, J. Pinson, F. Podvorica, *J. Am. Chem. Soc.* **2001**, 123, 4541–4549.
- [10] J. Pinson, F. Podvorica, *Chem. Soc. Rev.* **2005**, 34, 5, 429–439.
- [11] Z. Tavakkoli, H. Goljani, H. Sepehrmansourie, D. Nematollahi, M. A. Zolfigol, *RSC Adv.* **2021**, 11, 42, 25811–25815.
- [12] J. D. Firth, I. J. S. Fairlamb, *Org. Lett.* **2020**, 22, 18, 7057–7059.
- [13] H. R. Lamontagne, B. H. Lessard, *ACS Appl. Polym. Mater.* **2020**, 2, 12, 5327–5344.
- [14] E. G. Bagryanskaya, S. R. A. Marque, *Chem. Rev.* **2014**, 114, 9, 5011–5056.
- [15] Y. Jing, M. Tesch, L. Wang, C. G. Daniliuc, A. Studer, *Tetrahedron* **2016**, 72, 48, 7665–7671.
- [16] J. Nicolas, Y. Guillaneuf, C. Lefay, D. Bertin, D. Gigmes, B. Charleux, *Prog. Polym. Sci.* **2013**, 38, 1, 63–235.
- [17] C. J. Hawker, A. W. Bosman, E. Harth, *Chem. Rev.* **2001**, 101, 12, 3661–3688.
- [18] L. Couvreur, C. Lefay, J. Belleney, B. Charleux, O. Guerret, S. Magnet, *Macromolecules* **2003**, 36, 22, 8260–8267.
- [19] A. Kermagoret, D. Gigmes, *Tetrahedron* **2016**, 72, 48, 7672–7685.
- [20] J. Nicolas, C. Dire, L. Mueller, J. Belleney, B. Charleux, S. R. A. Marque, D. Bertin, S. Magnet, L. Couvreur, *Macromolecules* **2006**, 39, 24, 8274–8282.
- [21] J. Nicolas, S. Brusseau, B. Charleux, *J. Polym. Sci. A Polym. Chem.* **2010**, 48, 1, 34–47.
- [22] R. Sen, S. Das, A. Nath, P. Maharana, P. Kar, F. Verpoort, P. Liang, S. Roy, *Front. Chem.* **2022**, 10, 1–24.
- [23] C. Meng, B. Wang, Z. Gao, Z. Liu, Q. Zhang, J. Zhai, *Sci. Rep.* **2017**, 7, 1, 41825.
- [24] S. Tanaka, S. Takaya, T. Kumeda, N. Hoshi, K. Miyatake, M. Nakamura, *Int. J. Hydrog. Energy* **2021**, 46, 55, 28078–28086.
- [25] J. Suikkola, T. Björninen, M. Mosallaei, T. Kankkunen, P. Iso-Ketola, L. Ukkonen, J. Vanhala, M. Mäntysalo, *Sci. Rep.* **2016**, 6.
- [26] O.-H. Huttunen, T. Happonen, J. Hiitola-Keinänen, P. Korhonen, J. Ollila, J. Hiltunen, *Ind Eng Chem. Res.* **2019**, 58, 43, 19909–19916.
- [27] S. Khan, L. Lorenzelli, R. S. Dahiya, *IEEE Sens. J.* **2015**, 15, 6, 3164–3185.
- [28] G. E. Jabbour, R. Radspinner, N. Peyghambarian, *IEEE J. Sel. Top. Quantum Electron.* **2001**, 7, 5, 769–773.
- [29] F. C. Krebs, *Sol. Energy Mater. Sol. Cells* **2009**, 93, 4, 394–412.

- [30] M. Li, D. W. Li, G. Xiu, Y. T. Long, *Curr. Opin. Electrochem.* **2017**, 3, 1, 137–143.
- [31] D. Tobjörk, R. Österbacka, *Adv. Mater.* **2011**, 23, 17, 1935–1961.
- [32] J. Wiklund, A. Karakoç, T. Palko, H. Yiğitler, K. Ruttik, R. Jäntti, J. Paltakari, *J. Manuf. Mater. Process.* **2021**, 5, 3, 89.
- [33] Q. Huang, Y. Zhu, *Adv. Mater. Technol.* **2019**, 4, 5, 1800546.
- [34] M. Prudenziati, J. Hormadaly, in *Printed Films: Materials Science and Applications in Sensors, Electronics and Photonics*, **2012**, pp. 3–29.
- [35] S. J. Potts, C. Phillips, T. Claypole, E. Jewell, *Coatings* **2020**, 10, 10, 1–17.
- [36] J. W. Phair, M. Lundberg, A. Kaiser, *Rheol. Acta* **2009**, 48, 2, 121–133.
- [37] D. S. Kim, A. Khan, K. Rahman, S. Khan, H. C. Kim, K. H. Choi, *Mater. Manuf. Processes* **2011**, 26, 9, 1196–1201.
- [38] N. Zavanelli, W.-H. Yeo, *ACS Omega* **2021**, 6, 14, 9344–9351.
- [39] L. Hu, D. S. Hecht, G. Grüner, *Chem. Rev.* **2010**, 110, 10, 5790–5844.
- [40] P. He, J. Cao, H. Ding, C. Liu, J. Neilson, Z. Li, I. A. Kinloch, B. Derby, *ACS Appl. Mater. Interfaces* **2019**, 11, 35, 32225–32234.
- [41] S.-J. Potts, T. Korochkina, A. Holder, E. Jewell, C. Phillips, T. Claypole, *J. Mater. Sci.* **2022**, 57, 4, 2650–2666.
- [42] C. Xiang, K. M. Papadantonakis, N. S. Lewis, *Mater. Horiz.* **2016**, 3, 3, 169–173.
- [43] J. Nicolas, L. Mueller, C. Dire, K. Matyjaszewski, B. Charleux, *Macromolecules* **2009**, 42, 13, 4470–4478.
- [44] W. Mei, M. Maric, *Macromol. React. Eng.* **2017**, 11, 3, 1600067.
- [45] R. S. Warembra, P. Betaubun, *E3S Web of Conferences* **2018**, 73, 13019.
- [46] S. J. Konopka, Bruce. McDuffie, *Anal. Chem.* **1970**, 42, 14, 1741–1746.
- [47] A. P. Washe, P. Lozano-Sánchez, D. Bejarano-Nosas, I. Katakis, *Electrochem. Acta* **2013**, 91, 166–172.
- [48] A. Morrin, A. J. Killard, M. R. Smyth, *Anal. Lett.* **2003**, 36, 9, 2021–2039.
- [49] P. Garrido-Barros, D. Moonshiram, M. Gil-Sepulcre, P. Pelosin, C. Gimbert-Suriñach, J. Benet-Buchholz, A. Llobet, *J. Am. Chem. Soc.* **2020**, 142, 141, 17434–17446.
- [50] S. Ve Baranton, D. Bélanger, *J. Phys. Chem. B* **2005**, 109, 51, 24401–24410.
- [51] L. Pichereau, I. López, M. Cesbron, S. Dabos-Seignon, C. Gautier, T. Breton, *Chem. Comm.* **2019**, 55, 4, 455–457.

6

RUTHENIUM COORDINATION OLIGOMER-BASED ANODE FOR PHOTOELECTROCHEMICAL WATER OXIDATION USING A TANDEM SOLAR CELL

6.1 INTRODUCTION

The conversion of solar energy into hydrogen by water splitting is a solution to produce clean hydrogen without fossil fuel-based electrical input. A light harvesting material, such as a photovoltaic cell, provides the electrolyzer with enough energy to carry out the electrocatalytic reactions, which ultimately generate hydrogen, that can be transported and used as needed. Moving from a fossil fuel-based energy grid to a circular hydrogen economy would benefit the environment, as no CO₂ is emitted in either the production or the combustion of hydrogen.

The most mature technology consists of zero-gap electrolyzers, where anode and cathode materials are directly in contact with an ion-conductive solid-state membrane. This configuration allows large operating current densities due to a minimized ohmic resistance between the electrodes. State-of-the-art electrolyzers use platinum and iridium oxide electrocatalysts ^[1–3] in proton-exchange membrane (PEM) electrolysis due to the superior intrinsic activity and higher stability in the acidic environment of platinum group metals (PGMs). However, the scientific community urges to limit the use of critical raw materials ^[4,5], trying to mitigate their scarcity and supply issues with their higher economic value compared to more abundant materials. An alternative is the use of anion exchange membranes (AEM), which enables the use of more abundant metals (e.g., Ni-based catalyst) thanks to their ruggedness in basic conditions ^[6], particularly for the multi-electrons anode half-reaction whose thermodynamic potential is significantly reduced (0.40 V at pH 14).

Few cases in the literature have reported the use of molecular catalysts in electrocatalytic water splitting applications ^[7,8], and few more showed their

performances in zero-gap flow electrolyzers^[9,10]. PMGs and non-PMGs molecular catalysts generally display good stability in acidic conditions and high activity^[11–14]. However, the factor that usually limits their use in electrolyzers is their ineffective heterogenization or integration in modified electrodes. Furthermore, the harsh conditions at the membrane interface (shear stress in flow cells, local pH, oxidative instability) might cause the catalyst to decompose during electrolysis^[15,16].

Here we study water splitting in a photovoltaic-electrolyzer (PV-EC) setup, where the photovoltaic cell is decoupled from the electrolyzer, thus having solar-to-electricity conversion and water splitting into two distinct modules. In particular, we focus our attention on the use of novel anode materials for water oxidation, and we opted for a recently developed ruthenium oligomer {[Ru^{II}(bda)-(4,4'-bpy)]_n(4,4'-bpy)} (where bda represent [2,2'-bipyridine]-6,6'-dicarboxylate and 4,4'-bpy is 4,4'-bipyridine), here called (Rubda)_n, shown high catalytic activity and graphitic affinity as a means for surface immobilization^[17]. Nonetheless, using rare metal-based catalysts remains a conundrum; previous attempts to prepare highly efficient modified electrodes based on more abundant molecular catalysts have failed (see Chapter 5). Integrating a molecular (Rubda)_n oligomer relies on the CH- π interactions with graphitic surfaces providing a solid and long-lasting anchoring strategy. Furthermore, the material reaches a remarkably high current density at neutral pH^[17].

The photovoltaic cell chosen to perform water splitting is a monolithic lead-based perovskite/perovskite tandem solar cell with an open circuit voltage (V_{oc}) of 1.93 V, high enough to drive water splitting (1.23 V) with sufficient overpotential at the solar cell maximum power point^[18]. The PV-EC system combines a molecular-based catalyst in a flow-EC cell, operated under nearly 1 sun illumination for the first time. The PV-EC configuration reduces the device design's complexity and independently grants each module's optimization. The electrochemical cell was operated using ultrapure water with a membrane electrode assembly (MEA) design, which increases the conductivity through a proton-conductive polymer membrane, and ohmic losses are minimized by reducing the distance between the anode and cathode.

6.2 RESULTS

6.2.1 Ru-bda oligomer: Anode preparation and characterization

The oligomer was synthesized as described in the literature (Figure 6.1a) [17,19] and characterized by ^1H -NMR, MALDI-TOF-MS, and electrochemical techniques. ^1H NMR analysis of the bipyridyl protons allows quantification of the number of Ru(bda) units within the oligomer chain (Figure 6.1b) by the equation:

$$n = \frac{H_9}{H_1} + 1 = 6$$

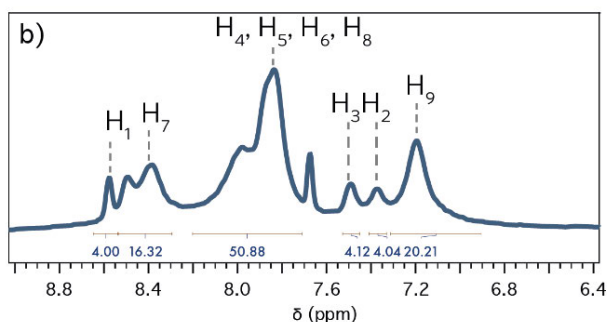
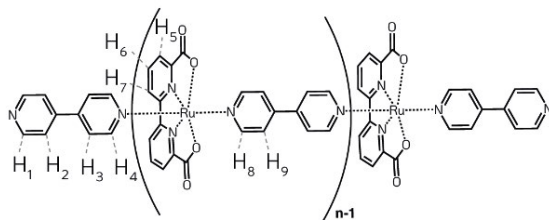
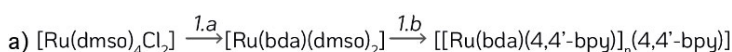


Figure 6.1. a) (Rubda)₆ synthetic route. 1.a) 2,2'-bipyridine-6,6'-dicarboxylic acid (H₂bda; 1 eq.), MeOH, Et₃N, 70°C, 76%. 1.b) 4,4'-bipyridine (bpy; 2 eq.), trifluoroethanol (TFE), 80°C for three days, 50%. b) ^1H -NMR of oligomer (Rubda) in TFE-*d*₃ in aromatic region.

To prepare the anode material, a solution (0.09 mg mL⁻¹) of (Rubda)₆ in TFE is drop-casted (3 x 30 μL) on a gas-diffusion layer (GDL) electrode of 1 cm². From the initial CV and DPV analysis (Figure 6.2a,b; red line), it is possible to observe the molecular redox processes assigned to the ruthenium centers Ru(bda) at $E_{1/2} \text{Ru}^{\text{III/II}} = 0.67 \text{ V}$, $E_{1/2} \text{Ru}^{\text{IV/III}} = 0.82 \text{ V}$ and $E_{1/2} \text{Ru}^{\text{V/IV}} = 1.09 \text{ V}$ vs. NHE. Upon repetitive scanning

at pH 7, the oligomer undergoes a molecular transformation, resulting in the non-catalytic waves appearing at $E_{1/2} \text{ Ru}^{\text{III/II}} = 0.52 \text{ V}$, $E_{1/2} \text{ Ru}^{\text{IV/III}} = 0.67 \text{ V}$, $E_{1/2} \text{ Ru}^{\text{V/IV}} = 0.84 \text{ V}$, and $E_{1/2} \text{ Ru}^{\text{VI/V}} = 1.44 \text{ V}$ (vs. NHE). The transformation to the active species is promoted by graphitic interaction, and it was shown to be assigned to a partial de-coordination of a pyridyl-carboxylate moiety^[17]. At the same time, two water molecules coordinate the ruthenium center, forming the species $(\text{Rubda}(\text{H}_2\text{O})_2)_6$, which experiences current density at the electrocatalytic potential. The free pyridyl group contributes to the surface affinity by π - π interaction.

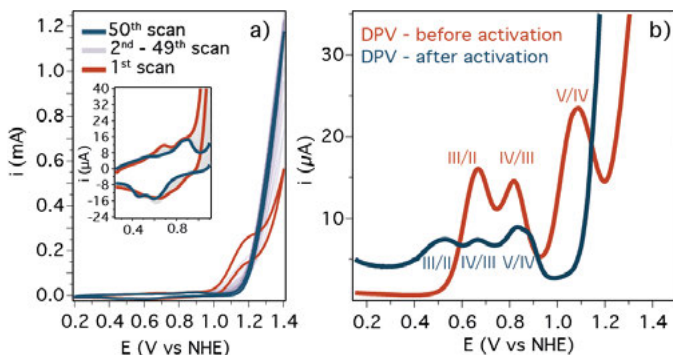


Figure 6.2. a) CV of GDL@Rubda) electrode (1 cm^2) within 50 scans ($v = 50 \text{ mVs}^{-1}$), showing the progressive molecular transformation of the primary coordination sphere, yielding in $(\text{Rubda})(\text{H}_2\text{O})_2$. b) DPV analysis of the catalyst before and after electrochemical activation. PBS 0.1 M, pH 7.1, working electrode GDL@Ru(bda), counter electrode Pt disk, and reference electrode Ag/AgCl.

The electrodes were further modified by introducing multiwall-carbon nanotubes (CNTs) in the catalyst casting solution, to enlarge the electrode surface area and the stability of the immobilized material. The catalyst $(\text{Rubda})_6$ and CNTs were mixed in a ratio of 1:10 in a way that the final concentrations were the following: 0.09 mg mL^{-1} of $(\text{Rubda})_6$ and 0.91 mg mL^{-1} of CNTs in a TFE:THF mixture (1:10). A series of 1 cm^2 electrodes were prepared by depositing several amounts of precursor $\text{CNT} @ (\text{Ru-bda})_6$ mixture. Figure 6.3a shows the CV of the activated WOC electrode GDL@CNT@ $(\text{Rubda}(\text{H}_2\text{O})_2)_6$ and a control electrode, on which only CNTs were cast. The catalyst loading, Γ (in mol cm^{-2}), was calculated from CV experiments by integration of the anodic and cathodic redox processes, as shown in Figure 6.3b, according to the equations:

$$\Gamma = \frac{Q_{\text{av}}}{nAF}$$

$$Q_{\text{av}} = \frac{Q_{\text{anode}} + Q_{\text{cathode}}}{2}$$

Where Q_{av} is the average charge (in C) of the anodic and cathodic redox processes ($Ru^{III/II}$, $Ru^{IV/III}$, $Ru^{V/IV}$), n is the number of electrons (3), A is the nominal surface area of the electrodes (in cm^2), and F is the Faraday constant (in $s\ A\ mol^{-1}$). Figure 6.3c shows the catalytic current (i_{cat}) achieved by the activated WOC in CVs at $50\ mV\ s^{-1}$ for each anode. The i_{cat} increases progressively with Γ ; however, the ratio of the catalytic current to the current of a single electron transfer event drops with greater Γ . This supports that only the first layer of oligomer onto the graphitic surface undergoes the activation. The equatorial pyridine decooordination, necessary for this process, is favored by a newly π - π interaction, which establishes between the decoordinating pyridine and the graphitic material. Furthermore, the dangling carboxylate can stabilize $RuOH_2$ through hydrogen within the activated $(Ru-bda(H_2O)_2)_6$. Therefore, lower loading with extended electrode sizes could achieve good current values to drive water splitting in the electrolyzer.

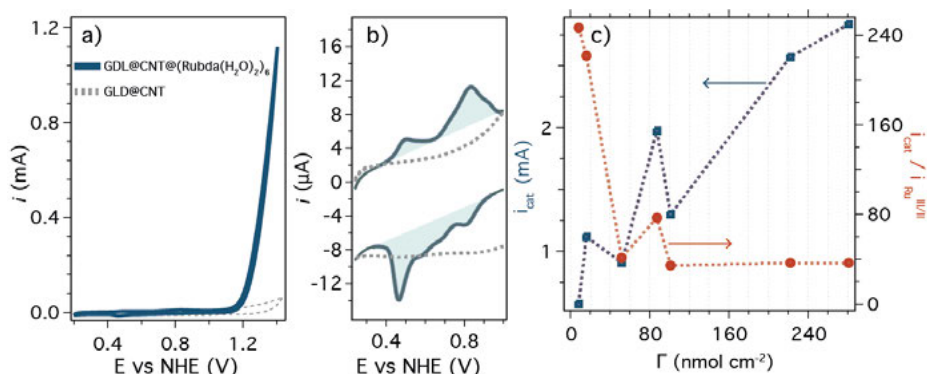


Figure 6.3. a) CV of a $1\ cm^2$ GDL@CNT@(Ru-bda(H_2O) $_2$) $_6$ anode ($20\ \mu L$ of $0.09\ mg\ mL^{-1}$ (Ru-bda) $_6$). b) Zoom of molecular ruthenium redox waves. $v\ 50\ mVs^{-1}$, PBS $0.1\ M$, pH 7.1 , working electrode GDL@(Rubda) $_6$, counter electrode Pt disk, and reference electrode Ag/AgCl. c) Electroactive loading of $1\ cm^2$ for different precursor amounts deposited ($10, 20, 45, 65, 90, 115, 140\ \mu L$ of $0.09\ mg\ mL^{-1}$). i_{cat} shows the current recorded at $1.4\ V$ (in blue), and $i_{cat} / i_{Ru^{III/II}}$ (in red) is the ratio of the catalytic current to the current of the $Ru^{III/II}$ oxidation process.

6.2.2 Stability and performance of the flow-electrolyzer

The electrochemical (EC) flow cell design is shown in Figure 6.4a; it is composed of two symmetrical compartments, each provided with a water supply inlet and outlet. Titanium current collector plates are present at each end, after which gaskets are applied to define the electrocatalytic active area ($1, 2, 3$, or $4\ cm^2$). Gas diffusion layers (GDL) are used as support electrodes for the catalytic material. A $50\ \mu m$ thick Nafion membrane separates the two compartments, allowing proton permeation from the anode to the cathode, where they are reduced to H_2 . The anode GDL@CNT@(Ru-bda) $_6$

is activated in a three-electrodes setup prior to its incorporation into the flow cell, as described above. While the anode is prepared as a catalyst-coated substrate (CCS), depositing Ru(bda)₆ onto the GDL, the cathode material (Pt/C) is spray-coated from a solution (3.75% w/w) directly onto the membrane (CCM, catalyst-coated membrane) to achieve a final loading of 1 mg cm⁻².

The electrochemical cell is assembled by pressing GDL@CNT@(Ru-bda)₆/Nafion@(Pt/C)/GDL between the titania plates and is closed by applying 0.8 Nm torque. The inlets and outlets are connected to feeding bottles with Milli-Q water, and a peristaltic pump set to 10 mL min⁻¹ supplies the cell with the substrate and, at the same time, extracts the gases formed. The water is pre-heated to 35 °C, with an effective inlets and outlets temperature of $T_{\text{in}} \approx T_{\text{out}} = 32 - 34^\circ\text{C}$ throughout the experiments. We perform a conditioning run at the open circuit potential for one hour before any experiment. This allows the system to equilibrate and the membrane to swell by absorbing water, which results in uniform contact between the membrane, catalyst layers, and electrode support interfaces.

Figure 6.4b shows the EC's three consecutively recorded polarization curves, using an active area of 1 cm² for both electrodes. The first polarization generates an anomalous response, with a current before the expected thermodynamic onset. We ascribe this behavior to incomplete equilibration of the cell, which could be due to a partial WOC deactivation before the EC is assembled, thus requiring further activation of Ru(bda)₆ after assembly of the EC. From the second polarization, the curves display an onset at ~ 1.0 V. When the potential reaches values above 1.2 V, the current plateaus, giving rise to an "S-shaped" curve. As we use Pt for the cathode in a much more significant amount (1 mg cm⁻² Pt/C), we expect the WOC to be the limiting factor responsible for the observed kinetic limitations.

Controlled potential electrolysis (CPE) at 1.4 V (Figure 6.4c) shows a stable output current of about 3 mA cm⁻² for 14 hours, after which the performance was reduced. Similarly, the potential recorded across the electrodes remains steady at ~ 1.396 V along the experiment, and it slowly increases to the theoretical, applied value when the EC's performance declines. However, a polarization curve recorded after CPE shows comparable behavior to the freshly prepared EC, with a slightly higher overpotential (Figure 6.4b, red line).

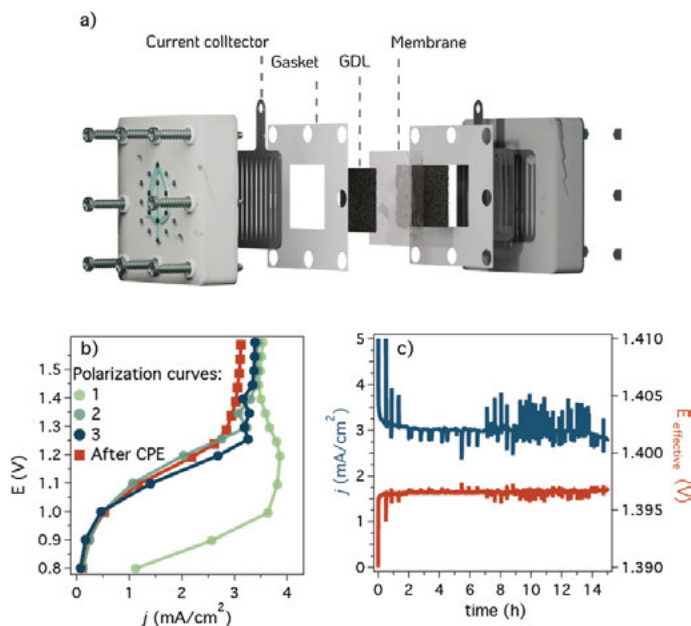


Figure 6.4. a) Electrochemical flow-cell stacks layout. b) EC potentiostatic polarization curves with 1 cm² electrodes 90 μ L of 0.09 mg mL⁻¹ CNT@(Ru-bda). c) Controlled potential electrolysis (CPE) at 1.4 V for 14 h.

We also studied the EC behavior as a function of the electrode size, maintaining about the same catalyst loading per geometrical surface area in 1 and 4 cm² electrolyzers. As expected, the galvanostatic polarization curves (Figure 6.5a) share similar potential values at low current densities. Nonetheless, when the current density applied is sufficient to drive catalysis at both electrodes, we observe that the smaller electrode performs better with lower overpotential. Increasing the catalyst loading aggravates the polarization (Figure 6.5b) and its “S-shape”. Constant current electrolysis (CCE) is used to evaluate the stability and the response of the different EC setups when currents of 1, 3, 5, and 10 mA are applied for 2 hours consecutively (Figure 6.5c). For all the electrode configuration setups, at 1 mA, we record potentials below 1 V, suggesting catalysis does not take place but only polarization of the solution-electrode interface. At 3 mA, we observe the 1 cm² EC forces the potential to 2.0 V. With 1 cm² electrodes size, the catalyst loading seems too low to sustain catalysis fully, therefore at such potential of 2.0 V, the carbon materials (GDL and CNTs) may contribute to water splitting. The 4 cm² EC configurations display a potential again below 1.0 V, with no visible catalysis in progress. At 5 mA, the 4 cm² at high Γ_{WOC} increases the potential throughout the electrolysis (> 1.5 V) with seldom drops in the potential.

The 4 cm² at low Γ_{WOC} to 1.3 V yields a progressively higher potential, but it is maintained below 1.5 V over the experiment. Nonetheless, the 1 cm² EC has lower overpotential compared to the 4 cm² EC, according to their polarization curves, larger size EC displays higher potential stability, especially when the loading is kept as low as possible. For these reasons and the fact that the absolute current produced by the EC needs to match the current output of the solar cell, we employed a 4 cm² electrolyzer for the PV-EC experiment.

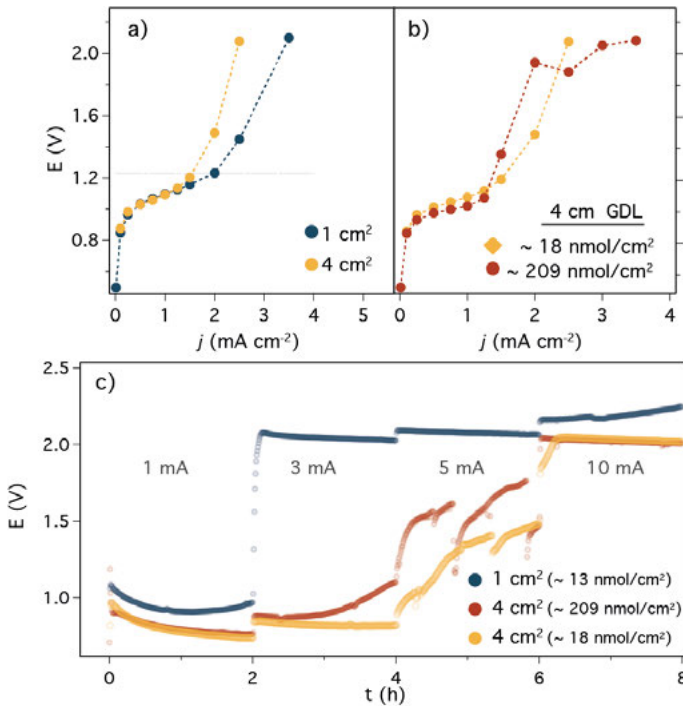


Figure 6.5. Polarization curves for a) different electrolyzer sizes, 1 and 4 cm² (WOC loading: $\Gamma_{4\text{cm}^2} = \sim 18 \text{ nmol cm}^{-2}$, $\Gamma_{1\text{cm}^2} = \sim 13 \text{ nmol cm}^{-2}$) and b) with different loading of (Rubda(H₂O)₂)₆ absorbed. c) Constant current electrolysis (CCE) at four different currents (1, 3, 5, and 10 mA) with different electrode sizes.

6.2.3 PV-powered hydrogen /oxygen evolution

To drive the water-splitting reaction, a monolithic perovskite/perovskite solar cell was used, as prepared by Datta *et al.* [18]. The schematic in Figure 6.6a shows that the anode is comprised of two sub-cells, consisting of wide bandgap ($E_g \approx 1.77 \text{ eV}$) and narrow bandgap ($E_g \approx 1.23 \text{ eV}$) photoactive materials. The wide bandgap film is a mixed-halide, mixed-cations perovskite based on FAPbI₃ (FA = formamidinium) and

MAPbBr₃ (MA = methylammonium) precursor solutions mixed in a 3:2 volumetric ratio. CsI and KI were introduced as additives to increase the film's photostability. The narrow bandgap material is a mixed Pb-Sn perovskite (nominally FA_{0.66}MA_{0.34}Pb_{0.5}Sn_{0.5}I₃). The two subcells were integrated using a C₆₀/atomic layer deposited (ALD) SnO_x/Au/PEDOT:PSS recombination junction. A self-assembled monolayer of [2-(9H-carbazol-9-yl)ethyl]phosphonic (2-PACz) was used as the hole transport front contact, and a thermally evaporated C₆₀/bathocuproine (BCP) layer as the electron transport back contact. Hydrogenated indium oxide (IOH) was used as a transparent front contact, deposited on a glass substrate, previously treated with an MgF₂ antireflection (AR) coating. The perovskite/C₆₀ interfaces were passivated in both subcells, with choline chloride in the wide bandgap and CdI₂ in the narrow bandgap. The additives were found to reduce the defects created at the layers interface, enhancing the V_{OC} of the respective subcell and, thus, the power conversion efficiency (PCE) [20,21]. The tandem cell used to run our PV-EC experiment showed a PCE of 18.7%, a value lower than the one reported initially, due to the reduced V_{OC} (1.82 V) and fill factor (FF = 0.63) that the cell exhibits after it has been stored. Figure 6.6b (red line) shows the *J*-*V* curve of the solar cell under simulated sunlight illumination.

A 4 cm² GDL@CNT@(Ru-bda) electrode was prepared and activated as described above, and the polarization curve of the integrated EC overlapped with the *J*-*V* curve of the solar cell. The crossing point reveals the expected operational condition of the PV-EC system, with an expected V_{op} = 1.5 V and an *i*_{op} = 11 mA. The EC and the monolithic perovskite tandem were wire-connected, and the solar cell was exposed to 1 sun equivalent light. The PV-EC was run for 48 hours in simulated day/night cycles of 30 minutes each (Figure 6.6c). The solar-to-hydrogen efficiency (η_{STH}) was calculated from the current output of the PV-EC system, assuming a WOC faradaic efficiency (η_F) of 0.94, as elsewhere reported^[17], according to the following equation:

$$\eta_{\text{STH}} = \frac{i_{\text{op}} E^0 \eta_{\text{F}}}{P_{\text{in}} A_{\text{PV}}}$$

Where *i*_{op} is the operational recorded current, E⁰ is the thermodynamic potential for water splitting, P_{in} is the power input provided by the light lamp (mW cm⁻²), and A_{PV} is the area of the photovoltaic cell (cm²). STH efficiency reaches values of about 12% at the beginning of each light cycle, only to drop rapidly to about 7% after 30 min. Surprisingly the initial efficiency is restored every time the light is switched back on. The reason for this behavior is not fully understood at present. The EC unit was found to be stable for several hours (Figure 6.4c), which suggests that tandem solar cell loses and then gains performance during cycling. A known reversible process that occurs in wide-bandgap perovskite solar cells is light-induced halide segregation, which may be

the reason for the oscillating performance during 30 min light on / 30 min light off cycling seen in Figure 6.6c. On the other hand, the potential is higher than expected, and after about 10 hours, it further slowly increases after each day/night cycle. This can be diagnostic of an EC deterioration, which would reduce the polarization's slope and shift the operational potential to higher values.

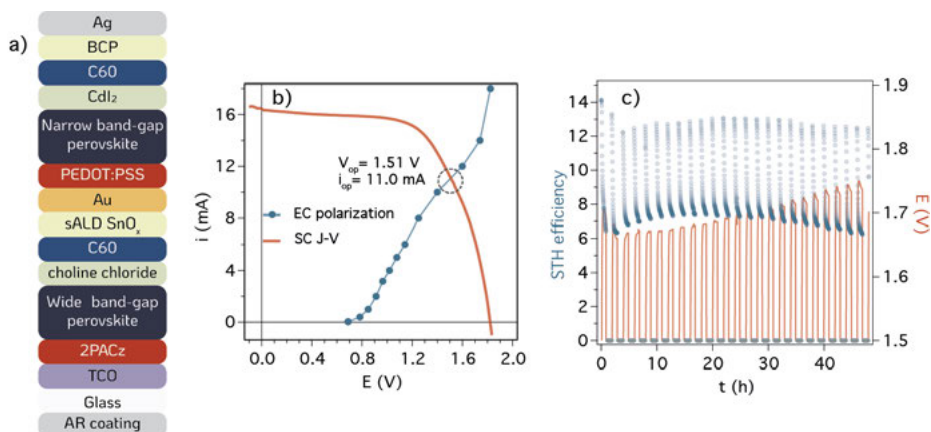


Figure 6.6. a) schematic of the monolithic perovskite/perovskite tandem solar cell used in our study. b) 4 cm² EC polarization curve ($I_{WOC}^* = 36$ nmol cm⁻²) and solar cell J-V curve prior to the PV-EC experiment. c) STH efficiency and potential experienced during the PV-EC experiment, under 1 sunlight illumination, for 48 hours, alternating light on and off every 30 minutes.

After prolonged experimental conditions, the anolyte-feeding water was found to be contaminated with a solubilized brown/black compound. A UV-vis spectrum was recorded of the contaminated water and compared to the spectrum of 2.5 $\mu\text{g ml}^{-1}$ (Rubda)₆ (Figure 6.7a). The broad and featureless absorption spectra of feeding water suggest that the WOC leaches off the electrode surface following some decomposition processes that occur in prolonged experiments. It could be due to the mechanical stress caused by the water pumped through the cell or, otherwise, by the material decomposition resulting from the increased local pH near the acidic Nafion membrane. In-situ CVs were also recorded by inserting a silver wire into the cell during the assembly process. The wire would serve as a pseudo-reference electrode in a three-electrodes setup. Figure 6.7b shows the in-situ CV before and after the PV-EC experiment, confirming that the catalyst has leached off from the electrode surface. The same applies to the polarization curve (Figure 6.7d), which reaches a low current and flat output. The solar cell also experienced degradation phenomena (Figure 6.7c), mostly from loss in the j_{sc} , while no significant loss in V_{oc} was observed. XPS analysis of the freshly activated GDL@(Rubda)(H₂O)₂ and of the anode after 12 h CPE do not show

any signal of the $\text{Ru3d}_{5/2}$, indicating the inadequacy of such a technique to detect the small amount of catalytic material that is integrated into the electrolyzer.

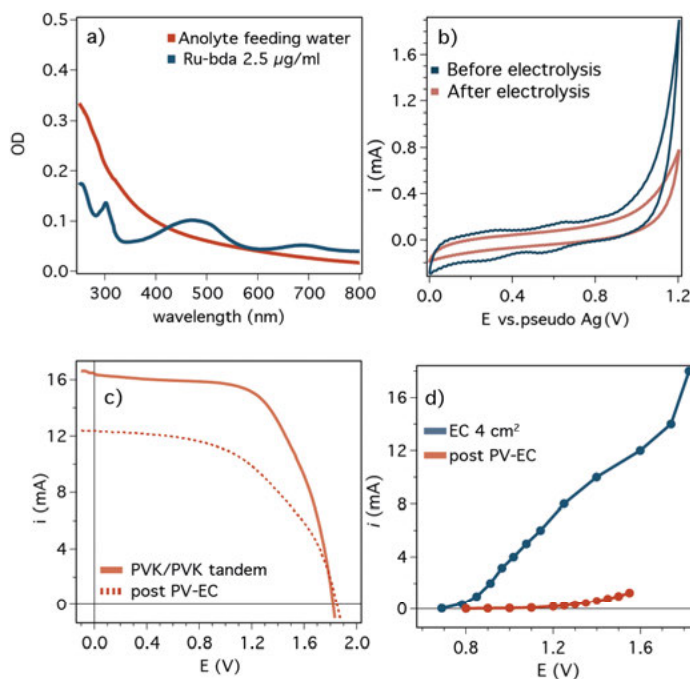


Figure 6.7. Post-light-driven electrolysis characterization. a) UV-vis spectra of $(\text{Ru-bda})_6$ and anolyte feeding water after the PV-EC experiment. b) In-situ CV of the anode into the 4 cm^2 EC, before and after PV-EC. c) J - V curves of the tandem solar cell before and after PV-EC. d) Polarization curves of the 4 cm^2 ($\Gamma_{\text{WOC}} = 36 \text{ nmol cm}^{-2}$) before and after PV-EC. Blue curve: galvanostatic polarization. Red line: potentiostatic polarization.

6.3 CONCLUSIONS

We have shown the integration of a molecular-based WOC oligomer into a flow electrolyzer operated by an external all-perovskite tandem solar cell at 1 sun equivalent light illumination. The intrinsic graphitic affinity allows the immobilization of the electroactive WOC oligomer through CH- π interactions. Other than the chemical stability, carbon-based materials, such as GDL and CNTs, are used to fabricate modified electrodes. An STH efficiency above 12% is recorded at the beginning of each illumination cycle. This value drops to about 6 - 7% during each 30 min illumination period but is restored during intermittent darkness. We ascribe the momentary

decrease in efficiency to a partial photo-degradation of the perovskite/perovskite solar cell. This process is a documented occurrence and is reversed when the solar cell is reposed in the dark for a period of time [22–24]. However, the averaged STH efficiency diminishes in the long term and the operational potential increases. We hold the EC deactivation responsible for this behavior by worsening the EC polarization. In fact, following the PV-EC experiment, no electroactive material is detected in the anode by CV, and a dark particulate is observed in the anolyte circulation system, which shows a broad and featureless absorption spectrum. The prolonged electrolysis conditions cause the decomposition of the WOC. Future studies could improve the stability of such catalysts by switching from a PEM, such as Nafion, to a less acidic membrane or to AEM, which raises local pH during electrolysis and should avoid the origin of degradation processes. Furthermore, when a stable EC device is built, it is necessary to quantify the oxygen evolved to corroborate the Faradaic efficiency of the PV-EC device.

6.4 EXPERIMENTAL DETAILS

Materials: Solvents and products were provided by Sigma-Aldrich, Alfa Aesar, or TCI chemicals unless indicated otherwise and used without further purification. Nafion® membrane NRE-212 was purchased from Ion Power. Multi-walled carbon nanotubes (CNTs) were purchased from Sigma Aldrich in bulk with >98 % purity, 6 - 13 nm OD, and 2.5 – 20 μm length. HPLC-grade water (18 M Ω), obtained by passing deionized water through a nanopure Mili-Q water purification system, was used in all electrochemical experiments

Electrochemical characterization: CVs and DPVs were measured on a Metrohm Autolab PGSTA30 potentiostat. Aqueous buffer solutions at pH 7 were prepared using specific concentrations of monobasic and dibasic phosphate salts such that the final ionic strength was 0.1 M. Ag/AgCl (KCl 3M) electrode was used as a reference, while Pt disk was used as a counter electrode.

NMR spectroscopy: ^1H NMR spectra were obtained on a 400 MHz Bruker Avance III spectrometer. All measurements were performed at room temperature in deuterated DMSO or deuterated 2,2,2-trifluoro ethanol (TFE) if not otherwise stated. Chemical shifts (δ) are reported in part per million (ppm).

UV-vis spectrometry: absorption spectra were recorded using a PerkinElmer Lambda 1050 UV-vis-NIR spectrophotometer.

Flow-electrochemical cell setup: The functionalization of CNT to form CNT@(Rubda) was done by dissolving 1 mg of (Rubda)₆ in 1 mL of pure TFE. In parallel, 10 mg of CNTs were sonicated in 10 mL of THF for 30 minutes. The CNT@(Rubda) suspension was prepared by mixing 0.1 mL of the (Rubda)₆ solution and 1 mL of the CNT suspension. The CNT@(Rubda) suspension was drop cast onto GDL support electrodes. The activated GDL@CNT@(Rubda(H₂O)₂) electrodes were obtained by cycling GDL@CNT@(Rubda) in 0.1 M PBS solution (pH 7.1) between 0.2 and 1.40 V vs. NHE at 50 mVs⁻¹. The Pt catalyst ink was prepared with 5 % w/v solid content, with a 3:1 ratio

of catalyst to Nafion® ionomer in 2-propanol:H₂O (4:1). The catalyst powder was first mixed with water to avoid combustion of the carbon particles and subsequently, the Nafion® dispersion and 2-propanol were sequentially added. The inks were sonicated for at least 10 min prior to catalyst deposition. The catalyst inks were spray-coated using a pneumatic airbrush (Aerotec) through a stainless-steel mask with a $2 \times 2 \text{ cm}^2$ opening on opposite sides of the membrane until the target loading of 1 mg cm^{-2} for Pt was reached. The catalyst loadings were calculated by weighing the membrane before and after coating. The deposition temperature was set to 85°C to evaporate the solvent upon deposition and to avoid excessive membrane swelling. Water electrolysis tests were carried out in an in-house built PEM – electrolyzer cell ($5 \times 5 \text{ cm}^2$) using high-impact polypropylene (PP) as end plates and titanium current collectors (1-mm thick) with machined parallel flow fields (1 mm wide, channel area: $2.25 \times 2.25 \text{ cm}^2$). A woven carbon fiber fabric gas diffusion layer (GDL; 255 μm , with microporous layer (MPL) and PTFE, GDL255, from Quintech) was used as a porous transport layer (PTL) at the anode and cathode, respectively. The MEA was pressed between the PTLs, and the electrolyzer was sealed with PTFE ($5 \times 5 \text{ cm}^2$, 200 mm, from Polyfluor). Polyimide film (50 μm , from Wu Xi Shun Xuan New Materials Co., Ltd) was used between the Ti PTL and the membrane to delimit the active area to 4 cm^2 . Millipore purified water (18 M Ω) was circulated using a peristaltic pump (Masterflex® L/S® Digital Miniflex®) into both anodic and cathodic compartments at 10 mL min^{-1} . Independent water lines and feeding bottles were used for each compartment. The water bottles were N₂-bubbled to prevent oxygen and hydrogen build-up.

Flow Electrochemical cell characterization: Galvanostatic and potentiostatic polarization curves and steady-state stability experiments were performed using a 2-channel Keithley 2600 SMU controlled by LabVIEW. The first channel applied the current, whereas the second measured the voltage across the PEM electrochemical cell. All measurements were done at $\sim 35^\circ\text{C}$. Water was circulated through the cell for 1 h to allow membrane swelling and equilibration before any measurements. The galvanostatic polarization curve was recorded from 0.001 to 3.5 mA cm^{-2} . Each current density step was held for 2 min to allow potential stabilization, and the average of the last 10 s was taken as the potential value

Solar cell characterization: Current density versus voltage (J - V) scans of the monolithic all perovskite tandem solar cell were done using a tungsten-halogen illumination source filtered by a UV filter (Schott GG385) and a daylight filter (Hoya LB120) with intensity adjusted to 100 mW cm^{-2} . A shadow mask with an aperture area of 1 cm^2 was used. The solar cells were operated under reverse or forward sweeps (between $+ 2.0 \text{ V}$ and $- 0.5 \text{ V}$) at a rate of 0.25 V s^{-1} using a Keithley 2400 source meter.

PV-EC water splitting experiments: Solar water splitting was performed using a homebuilt solar simulator with a tungsten-halogen illumination source filtered by a UV filter (Schott GG385) and a daylight filter (Hoya LB120) with intensity adjusted to obtain the operating current point at approximately 1 sun equivalent light intensity. All experiments took place outside the glove-box environment, so the solar cell was kept inside a nitrogen-filled box and connected to the electrochemical cell via external wiring. A Keithley 2600 SMU controlled by code written in the LabVIEW environment was used to simultaneously measure the current and the voltage across the electrochemical cell. Diurnal cycling experiments were carried out using a programmable time electric plug (Theben) to switch the lamp on and off every 30 minutes.

Synthetic details

1.a

A mixture of 2,2'-bipyridine-6,6'-dicarboxylic acid (H_2bda ; 244 mg, 1.00 mmol), $[Ru^{II}(DMSO)_4Cl_2]$ (484 mg, 1.00 mmol), and Et_3N (0.8 mL) in methanol (20 mL) was degassed with N_2 and refluxed over 4 hours. After cooling to room temperature, the precipitate was collected, washed with cold methanol, and then diethyl ether, providing the desired product as a brown powder.

Yield = 282 mg; 0.56 mmol; 76 %

1H -NMR (400 MHz, $DMSO-d_6$) δ : 8.65 (dd, $J = 8.0, 1.1$ Hz, 2H), 8.16 (t, $J = 7.9$ Hz, 2H), 8.08 – 8.01 (m, 2H), 2.54 (s, 12H).

1.b ($Rubda$)₆

A mixture of $[Ru(bda)(dmsO)_2]$ (50.1 mg, 0.10 mmol) and 4,4'-bipyridine (bpy; 15.7 mg, 0.10 mmol) were placed in a 50 mL two-neck round bottom flask and degassed by vacuum-nitrogen cycles. Then, degassed TFE (10 mL) was added, and the resulting solution was heated under nitrogen at 78 °C for 3 days. Afterward, the solution was evaporated to dryness and washed with DCM/MeOH (2:1) 5 x 5 mL. The remaining brownish solid was washed with Et_2O and dried under vacuum, yielding ($Rubda$)₆ as red-brown powder, which was stored in the glove box.

Yield: 50.6 mg; 50 %.

1H -NMR (400 MHz, TFE- d_3) δ : 8.62 (s, 4H), 8.53–8.28 (m, 16H), 8.19–7.70 (m, 51H), 7.48 (s, 4H), 7.36 (s, 4H), 7.20 (m, 20H).

6.5 REFERENCES

- [1] C. Minke, M. Suermann, B. Bensmann, R. Hanke-Rauschenbach, *Int. J. Hydrogen. Energy* **2021**, 46, 23581–23590.
- [2] F. Karimi, A. Bazylak, B. A. Peppley, *J. Electrochem. Soc.* **2017**, 164, 4, 464–474.
- [3] E. Antolini, *ACS Catal.* **2014**, 4, 5, 1426–1440.
- [4] P. Ferro, F. Bonollo, *Mater. Des.* **2019**, 177, 107848.
- [5] M. Girtan, A. Wittenberg, M. L. Grilli, D. P. S. de Oliveira, C. Giosuè, M. L. Ruello, *Materials* **2021**, 14, 8, 1826–1844.
- [6] J. Ekspong, C. Larsen, J. Stenberg, W. L. Kwong, J. Wang, J. Zhang, E. M. J. Johansson, J. Messinger, L. Edman, T. Wågberg, *ACS Sustain. Chem. Eng.* **2021**, 9, 42, 14070–14078.
- [7] K. Akamine, K. Morita, K. Sakai, H. Ozawa, *ACS Appl. Energy Mater.* **2020**, 3, 5, 4860–4866.
- [8] Y. Shi, T. Y. Hsieh, M. A. Hoque, W. Cambarau, S. Narbey, C. Gimbert-Surinäch, E. Palomares, M. Lanza, A. Llobet, *ACS Appl. Mater. Interfaces* **2020**, 12, 50, 55856–55864.
- [9] S. Ren, D. Joulié, D. Salvatore, K. Torbensen, M. Wang, M. Robert, C. P. Berlinguette, *Science* **2019**, 365, 6451, 367–369.

- [10] B. Siritanaratkul, M. Forster, F. Greenwell, P. K. Sharma, E. H. Yu, A. J. Cowan, *J. Am. Chem. Soc.* **2022**, *144*, 17, 7551–7556.
- [11] O. Pantani, E. Anxolabéhère-Mallart, A. Aukauloo, P. Millet, *Electrochem. Commun.* **2007**, *9*, 1, 54–58.
- [12] J. al Cheikh, A. Villagra, A. Ranjbari, A. Pradon, M. Antuch, D. Dragoe, P. Millet, L. Assaud, *Appl. Catal. B* **2019**, *250*, 292–300.
- [13] M. Bellini, J. Bösken, M. Wörle, D. Thöny, J. J. Gamboa-Carballo, F. Krumeich, F. Bärtoli, H. A. Miller, L. Poggini, W. Oberhauser, A. Lavacchi, H. Grützmacher, F. Vizza, *Chem. Sci.* **2022**, *13*, 13, 3748–3760.
- [14] R. Matheu, P. Garrido-Barros, M. Gil-Sepulcre, M. Z. Ertem, X. Sala, C. Gimbert-Suriñach, A. Llobet, *Nat. Rev. Chem.* **2019**, *3*, 5, 331–341.
- [15] B. Zhang, L. Sun, *Chem. Soc. Rev.* **2019**, *48*, 7, 2216–2264.
- [16] B. Zhang, L. Fan, R. B. Ambre, T. Liu, Q. Meng, B. J. J. Timmer, L. Sun, *Joule* **2020**, *4*, 7, 1408–1444.
- [17] M. Gil-Sepulcre, J. O. Lindner, D. Schindler, L. Velasco, D. Moonshiram, O. Rüdiger, S. Debeer, V. Stepanenko, E. Solano, F. Würthner, A. Llobet, *J. Am. Chem. Soc.* **2021**, *143*, 30, 11651–11661.
- [18] K. Datta, J. Wang, D. Zhang, V. Zardetto, W. H. M. Remmerswaal, C. H. L. Weijtens, M. M. Wienk, R. A. J. Janssen, *Adv. Mater.* **2022**, *34*, 11, 2110053.
- [19] Q. Daniel, L. Wang, L. Duan, F. Li, L. Sun, *Dalton Trans.* **2016**, *45*, 37, 14689–14696.
- [20] X. Zheng, B. Chen, J. Dai, Y. Fang, Y. Bai, Y. Lin, H. Wei, X. C. Zeng, J. Huang, *Nat. Energy* **2017**, *2*, 7, 17102.
- [21] W. Q. Wu, P. N. Rudd, Z. Ni, C. H. van Brackle, H. Wei, Q. Wang, B. R. Ecker, Y. Gao, J. Huang, *J. Am. Chem. Soc.* **2020**, *142*, 8, 3989–3996.
- [22] M. Prete, M. v. Khenkin, D. Glowienka, B. R. Patil, J. S. Lissau, I. Dogan, J. L. Hansen, T. Leißner, J. Fiutowski, H. G. Rubahn, B. Julsgaard, P. Belling, V. Turkovic, Y. Galagan, E. A. Katz, M. Madsen, *ACS Appl. Energy Mater.* **2021**, *4*, 7, 6562–6573.
- [23] S. W. Lee, S. Kim, S. Bae, K. Cho, T. Chung, L. E. Mundt, S. Lee, S. Park, H. Park, M. C. Schubert, S. W. Glunz, Y. Ko, Y. Jun, Y. Kang, H. S. Lee, D. Kim, *Sci. Rep.* **2016**, *6*, 38150.
- [24] W. Nie, J. C. Blancon, A. J. Neukirch, K. Appavoo, H. Tsai, M. Chhowalla, M. A. Alam, M. Y. Sfeir, C. Katan, J. Even, S. Tretiak, J. J. Crochet, G. Gupta, A. D. Mohite, *Nat. Commun.* **2016**, *7*, 11574.

7

OUTLOOK

The prospect of the world's current energetic crisis is complex and a critical issue that requires a comprehensive solution that considers social, environmental, and economic aspects. Yet, the transition from fossil fuel-based sources to renewable energy sources is a necessary step toward achieving a sustainable future, and the world must address these challenges by promoting more sustainable practices and innovations.

One promising solution for renewable energy production is the use of an artificial photosynthetic system to produce hydrogen. This system is inspired by nature, where plants use sunlight to produce chemical energy through photosynthesis. Similarly, an artificial photosynthetic system could use sunlight to split water into hydrogen and oxygen, which can be used as a clean and renewable energy source. This technology could be revolutionary in addressing the energetic crisis, as it has the potential to produce large amounts of hydrogen sustainably and at a low cost.

The essence of a water-splitting device consists of its catalysts, which role is to reduce the energetic barrier for the conversion of water into hydrogen and oxygen. There are several reasons why molecular catalysts are of strong interest. They are the core of energy generation in living matter, which already gives an idea of the significance of these compounds. Molecular catalysts are highly versatile as the first- and second-coordination spheres of the organic ligand system can be sterically and electronically modified through synthetic procedures. The tunability has a consequence on product selectivity, where competitive reactions between intermediates and reagents can occur. This is particularly the case for CO₂ reduction, where the reaction of multiple electrons and protons needs to be energetically favored over the simpler proton reduction. The control over the single active site and its coordination spheres is used to steer the selectivity towards desired products^[1]. This has a huge impact on the development of CO₂ electrolyzers, as controlled selectivity is required to increase the desired product's yield and maintain low separation and purification costs^[2,3]. The methodic investigation of these materials allows for gaining knowledge of their reaction mechanism, which information can be used to enhance their intrinsic performances^[4].

It is easily deduced from Chapters 3 and 5, that modifications of the TAML ligand system have adverse outcomes on the active complex $[\text{CuMac}]^{2-}$. Previous studies on similar ligand systems have shown that introducing more electron-donating groups on the aromatic ring reduce the overpotential of the reaction. Nonetheless, the oxidative robustness of the species is compromised, and material degradation is observed ^[5]. In the case presented in Chapter 3, electron-withdrawing groups were introduced to the TAML system. The observed suppressed activity of the catalyst is ascribed not to degradation processes but to a decrease in reaction kinetics due to a high degree of stabilization of the radical cation reaction intermediates during the catalytic cycle. Whereas, in Chapter 5, the lack of activity of the hybrid electrodes could be caused by the presence of the two anchor point functionalities on each molecule. This could lead to uncontrolled side reactions on one group after the other has successfully grafted onto the surface. In both cases, further optimization in the synthetic design or protocols might improve or leave unaltered the activity of $[\text{CuMac}]^{2-}$. This could include strategies where the grafting groups are placed further away from the core of the TAML. Therefore, ideally, catalysts need to be designed bearing in mind the strategy they will be anchored within the final device, considering that the process might modify the performances or synthetic limitations might not make it a viable solution.

Despite their advantages, molecular catalysts struggle with their life span, generally reporting under the required potential ($> 1.4 \text{ V}$) and, in most cases, extreme electrolyte pH, stabilities not yet adequate for commercialization. This is especially the case for the anodic active materials, as (partial)ligand oxidation, oxide formation, and ligand substitution are some of the processes that might diminish the performance eventually ^[6,7]. First-row transition metal complexes are particularly affected, as they have a tendency for a higher degree of thermodynamic instability and kinetic limitations ^[8]. Considering the state-of-the-art of molecular electrocatalysts, I believe that inorganic catalysts will be the immediate solution to energy production applications, as they are currently at a higher readiness level than the corresponding molecular materials. Such materials might include polyoxometalate (POM) ^[9] and metal oxyhydroxides ^[10–12]. A more hybrid approach could be the use of MOFs ^[13,14] or COFs ^[15], which retain the physical properties of heterogeneous porous catalysts, allowing the tunability of the active sites through (post)synthetic modification of their organic linkers. Similarly, metal nitrogen-doped carbon supports (MNCs) can be a promising alternative, where single-atom metals (M) are strongly coordinated to nitrogen atoms incorporated in the carbon structure, forming catalytically active material with metal-N-macrocycles like frameworks. ^[16,17].

However, research on molecular catalysts should continue to learn to control and manipulate their activity and stability, aiming at better catalysts in the future. In the same way, as nature does, a solution could be to embed catalysts into protein scaffolds, which could increase catalysts' stability, enhance their efficiency or enable the use of aqueous electrolytes for some complexes that usually require organic solvents ^[18].

The architecture of the device also has major consequences on the proper operation and overall energy conversion efficiency of electrolyzers. With the coming of the zero-gap-electrolyzers and polymer electrolyte membranes, the technology has seen large improvements in achieving high current densities, reducing resistive elements, and limiting hydrogen crossover compared to porous separators ^[19,20]. However, the cost of the membranes ^[21] is a factor that can hinder further development and commercialization. In the last few years, electrolyzers were reported where the architectures were adapted to remove such elements. One example is an electrochemical-thermally activated chemical (E-TAC) electrolyzer, where the water oxidation and hydrogen evolution reaction are temporally decoupled. During the first step, the hydrogen evolution reaction is driven electrochemically at the cathode while the anode is oxidized. A second exergonic chemical step follows with the oxidation of water, which regenerate the anode in its initial state ^[22]. By doing so, they managed to make the use of a membrane between the electrodes obsolete and improved the overall energy conversion efficiency. Another example is a capillary-fed electrolyzer ^[23], through which the electrolyte transport is induced by the capillary effect of a porous separator. Both these device designs have the potential to remodel water splitting electrolyzers.

REFERENCES

- [1] N. Elgrishi, M. B. Chambers, X. Wang, M. Fontecave, *Chem. Soc. Rev.* **2017**, *46*, 761–796.
- [2] P. Saha, S. Amanullah, A. Dey, *Acc. Chem. Res.* **2022**, *55*, 134–144.
- [3] K. P. Kuhl, T. Hatsukade, E. R. Cave, D. N. Abram, J. Kibsgaard, T. F. Jaramillo, *J. Am. Chem. Soc.* **2014**, *136*, 14107–14113.
- [4] C. Costentin, S. Drouet, M. Robert, J.-M. Savéant, *Science* **2012**, *338*, 90–94.
- [5] P. Garrido-Barros, I. Funes-Ardoiz, S. Drouet, J. Benet-Buchholz, F. Maseras, A. Llobet, *J. Am. Chem. Soc.* **2015**, *137*, 6758–6761.
- [6] P. Garrido-Barros, C. Gimbert-Suriñach, R. Matheu, X. Sala, A. Llobet, *Chem. Soc. Rev.* **2017**, *46*, 6088–6098.
- [7] A. E. Thorarinsdottir, D. G. Nocera, *Chem. Catalysis* **2021**, *1*, 32–43.
- [8] L. H. Zhang, S. Mathew, J. Hessels, J. N. H. Reek, F. Yu, *ChemSusChem* **2020**, *14*, 1, 243–250.
- [9] D. Gao, I. Trentin, L. Schwiedrzik, L. González, C. Streb, *Molecules* **2020**, *25*, 1, 157.
- [10] O. Diaz-Morales, D. Ferrus-Suspedra, M. T. M. Koper, *Chem. Sci.* **2016**, *7*, 2639–2645.
- [11] A. Peugeot, C. E. Creissen, D. Karapinar, H. N. Tran, M. Schreiber, M. Fontecave, *Joule* **2021**, *5*, 1281–1300.

-
- [12] J. Wang, S.-J. Kim, J. Liu, Y. Gao, S. Choi, J. Han, H. Shin, S. Jo, J. Kim, F. Ciucci, H. Kim, Q. Li, W. Yang, X. Long, S. Yang, S.-P. Cho, K. H. Chae, M. G. Kim, H. Kim, J. Lim, *Nat. Catal.* **2021**, *4*, 212–222.
- [13] S. Mukhopadhyay, O. Basu, R. Nasani, S. K. Das, *Chem. Commun.* **2020**, *56*, 11735–11748.
- [14] A. Howe, T. Liseev, M. Gil-Sepulcre, C. Gimbert-Suriñach, J. Benet-Buchholz, A. Llobet, S. Ott, *Mater. Adv.* **2022**, *3*, 4227–4234.
- [15] S. Karak, V. Stepanenko, M. A. Addicoat, P. Keßler, S. Moser, F. Beuerle, F. Würthner, *J. Am. Chem. Soc.* **2022**, *144*, 17661–17670.
- [16] J. S. Bates, F. Khamespanah, D. A. Cullen, A. A. Al-Omari, M. N. Hopkins, J. J. Martinez, T. W. Root, S. S. Stahl, *J. Am. Chem. Soc.* **2022**, *144*, 18797–18802.
- [17] S. Keshipour, F. Eyvari-Ashnak, *ChemElectroChem* **2023**, *10*, 7, e202201153.
- [18] S. Hanreich, E. Bonandi, I. Drienovská, *ChemBioChem* **2022**, *24*, 6, e202200566.
- [19] R. Phillips, C. W. Dunnill, *RSC Adv.* **2016**, *6*, 100643–100651.
- [20] W. J. F. Gannon, M. Newberry, C. W. Dunnill, *Int. J. Hydrogen Energy* **2022**, *47*, 30347–30358.
- [21] A. Mayyas, M. Ruth, B. Pivovar, G. Bender, K. Wipke, *Manufacturing Cost Analysis for Proton Exchange Membrane Water Electrolyzers*, **2019**, Golden CO: National Renewable Energy Laboratory. NREL/TP-6A20-72740.
- [22] H. Dotan, A. Landman, S. W. Sheehan, K. D. Malviya, G. E. Shter, D. A. Grave, Z. Arzi, N. Yehudai, M. Halabi, N. Gal, N. Hadari, C. Cohen, A. Rothschild, G. S. Grader, *Nat. Energy* **2019**, *4*, 786–795.
- [23] A. Hodges, A. L. Hoang, G. Tsekouras, K. Wagner, C. Y. Lee, G. F. Swiegers, G. G. Wallace, *Nat. Commun.* **2022**, *13*, 1, 1304.

SUMMARY

The energy crisis that society is currently facing refers to the challenge of meeting the increasing demand for energy with finite and diminishing fossil fuel resources, which are the primary source of energy for society. As the world population grows, so does the need for energy to fuel our homes, industries, and transportation. However, the use of non-renewable sources of energy such as coal, oil, and gas has led to environmental problems such as air and water pollution, climate change, and other health hazards.

In recent years, there has been a growing awareness of the need to transition to renewable energy to mitigate the effects of climate change and reduce greenhouse gas emissions. Governments, businesses, and individuals are investing in renewable energy infrastructure and technologies to create a more sustainable energy future.

In this thesis, transition metal-based molecular complexes are explored for water oxidation catalysis and integrated into water-splitting devices. Water oxidation (WO) is a key reaction in all processes intended to produce chemical fuels (e.g., hydrogen, carbon monoxide, formic acid) from water. When WO is driven by solar light, it is also referred to as artificial photosynthesis ^[1]. WO typically requires a high overpotential to overcome the kinetic barrier that is associated with O-O bond formation and the multi-electron transfer nature of the reaction.

Foreseeing scalable and industrial applications of artificial photosynthetic devices, it is crucial to incorporate molecular catalysts into solid-state electrode materials, and progress needs to be made on heterogenization techniques. In this thesis, two possible strategies were considered: the incorporation of the molecular WO catalyst into a metal-organic framework (MOF) and its immobilization into a polymeric matrix. The work focuses on a molecular copper catalyst with a tetra-amidate macrocyclic ligand (TAML), called [CuMac]²⁻, which can be isolated as a (Me₄N)₂[CuMac] salt ^[2]. Derivatives of the organic ligand scaffold, bearing either two ester or two carboxylic acids functionalities, were synthesized to enable heterogenization of [CuMac]²⁻. The compounds were characterized electrochemically and spectroscopically and were evaluated for their oxygen evolution reaction (OER) activity at different operational pH. [CuMac]²⁻ features remarkable redox and structural robustness at neutral pH, thanks to the macrocyclic effect. This is in contrast to other first-row transition metal complexes that are often structurally more labile, leading to decomposition and, thus, deactivation. However, the

introduction of the carboxylic moieties seems to be kinetically detrimental for the OER activity compared to that of the $[\text{CuMac}]^{2-}$. In addition, synthetic limitations were encountered that hampered the preparation of the $[\text{CuMac}]^{2-}$ analogues with linearly arranged carboxylates, which would be the required geometry for MOF assembly.

In the next chapter, a study on identifying possible short-lived intermediates is presented. The goal of this section was to gain insight into the catalytic mechanism of $[\text{CuMac}]^{2-}$. As water oxidation reactions occur, the catalyst must achieve higher oxidation states to fulfill the four-electron transfer per cycle. In the case of $[\text{CuMac}]^{2-}$, this was achieved with the aid of the redox non-innocent macrocyclic ligand. The Mac^{4-} ligand is tetra-anionic in nature, and its extended π delocalization, can convey and preserve radical species for later use in the catalytic cycle. To understand the early steps in the catalytic cycle, UV-visible transient spectroscopy was used to deduce the electron transfer mechanism and kinetics of catalyst oxidation. We used a flash-photolysis method, utilizing $[\text{Ru}(\text{bpy})_3]\text{Cl}_2$ and persulfate as the photosensitizer and the quencher, respectively, to gather evidence of one-electron oxidized catalyst and following intermediates that were not temporally resolved by electrochemical means.

To pursue the development of solid-state anode materials, we adopted screen-printing technologies that, in the last years, have seen low-cost fabrication of electronics thanks to printing on polymer substrates. Examples of such applications are solar cells, light-emitting diodes, transistors, gas sensors, and printed batteries [3–5]. Printed electrodes (PEs) were fabricated using graphite as the conductive material, which allows the electrodes to be readily manufactured, and a polymer binder P(MMA-*s*-HEMA), *i.e.*, a statistical co-polymer of methyl methacrylate, styrene, and hydroxy ethyl methacrylate which was custom-made for the purpose. The binder was designed to increase the PE's hydrophilicity, an important consideration when designing a water electrolyzer because gaseous products (H_2 and O_2) must readily desorb from the surface, leaving the electroactive surface available for the next turnover cycle [6–8]. The PEs were then covalently functionalized with $[\text{CuMac}]^{2-}$ using an in-situ electroreduction of the corresponding bis(diazonium) compound $(\text{N}_2)_2[\text{CuMac}]$ to anchor it onto the electrode surface. To this end the macrocyclic scaffold was modified, introducing amine moieties, to make it suitable for synthesizing the diazonium derivative and subsequent grafting to the graphite surface. The resulting heterogenized catalyst's activity was evaluated by cyclic voltammetry, to find that it was impeded compared to $[\text{CuMac}]^{2-}$ in homogeneous solution phase.

Finally, we integrated a molecular-based water oxidation catalyst in a flow-electrolyzer powered by a perovskite/perovskite tandem solar cell to drive the water splitting by light in a so-called photovoltaic-electrochemical configuration (PV-EC) [9].

We focused on a molecular ruthenium-based coordination oligomer water oxidation catalyst $[\text{Ru}(\text{bda})(4,4'\text{-bpy})]_6(4,4'\text{-bpy})$. It has been shown that the catalyst establishes CH- π interactions with graphitic surfaces providing a durable anchoring strategy^[10]. Furthermore, during catalyst activation, a new molecular species is formed, which reaches a remarkably high current density at neutral pH^[10]. We achieved an operational voltage of 1.4 V and a solar-to-hydrogen efficiency (STH) of 12.5 %. However, the stability of the system remains to be improved, as we observed the water oxidation catalyst leaching out the electrolyzer under long experimental conditions (> 12 h). This may be improved by changing the membrane separating the two electrolyte compartments, which determines the local pH surrounding the catalyst, an essential parameter for the catalyst activity, integrity, and binding.

REFERENCES

- [1] S. Berardi, S. Drouet, L. Francàs, C. Gimbert-Suriñach, M. Guttentag, C. Richmond, T. Stoll, A. Llobet, *Chem. Soc. Rev.* **2014**, *43*, 7501–7519.
- [2] P. Garrido-Barros, D. Moonshiram, M. Gil-Sepulcre, P. Pelosin, C. Gimbert-Suriñach, J. Benet-Buchholz, A. Llobet, *J. Am. Chem. Soc.* **2020**, *142*, 41, 17434–17446.
- [3] J. Wiklund, A. Karakoç, T. Palko, H. Yiğitler, K. Ruttik, R. Jäntti, J. Paltakari, *J. Manuf. Mater. Process.* **2021**, *5*, 3, 89.
- [4] S. Khan, L. Lorenzelli, R. S. Dahiya, *IEEE Sens. J.* **2015**, *15*, 6, 3164–3185.
- [5] O.-H. Huttunen, T. Happonen, J. Hiitola-Keinänen, P. Korhonen, J. Ollila, J. Hiltunen, *Ind Eng Chem. Res.* **2019**, *58*, 19909–19916.
- [6] R. Sen, S. Das, A. Nath, P. Maharana, P. Kar, F. Verpoort, P. Liang, S. Roy, *Front. Chem.* **2022**, *10*, 861604.
- [7] C. Meng, B. Wang, Z. Gao, Z. Liu, Q. Zhang, J. Zhai, *Sci. Rep.* **2017**, *7*, 41825.
- [8] S. Tanaka, S. Takaya, T. Kumeda, N. Hoshi, K. Miyatake, M. Nakamura, *Int J Hydrogen Energy* **2021**, *46*, 28078–28086.
- [9] T. J. Jacobsson, V. Fjällström, M. Edoff, T. Edvinsson, *Energy Environ. Sci.* **2014**, *7*, 2056–2070.
- [10] M. Gil-Sepulcre, J. O. Lindner, D. Schindler, L. Velasco, D. Moonshiram, O. Rüdiger, S. Debeer, V. Stepanenko, E. Solano, F. Würthner, A. Llobet, *J. Am. Chem. Soc.* **2021**, *143*, 30, 11651–11661.

SUMMARY (SWEDISH)

Den energikris som samhället för närvarande står inför handlar om utmaningen att möta den ökande efterfrågan på energi med begränsade och minskande fossila bränsleresurser, vilka utgör den primära energikällan för samhället. När världsbefolkningen växer, ökar också behovet av energi för att driva våra hem, industrier och transporter. Användningen av icke-förnybara energikällor som kol, olja och gas har dock lett till miljöproblem såsom luft- och vattenföroreningar, klimatförändringar och andra hälsorisker.

Under de senaste åren har det funnits en ökad medvetenhet om behovet av att övergå till förnybar energi för att mildra effekterna av klimatförändringen och minska utsläppen av växthusgaser. Regeringar, företag och enskilda personer investerar i förnybar energi-infrastruktur och teknik för att skapa en mer hållbar framtid.

I denna avhandling utforskas övergångsmetallbaserade molekyllkomplex för vattenoxideringskatalys och integreras i vattendelande anordningar. Vattenoxidation (VO) är en viktig reaktion i alla processer avsedda att producera kemiska bränslen (t.ex. väte, kolmonoxid, myrsyra) från vatten. När VO drivs av solenergi kallas det också konstgjord fotosyntes^[1]. VO kräver vanligtvis en hög överpotential för att övervinna den kinetiska barriären som är förknippad med O-O-bindningsbildning och för att reaktionen kräver flera elektronöverföringar.

För att förutse skalbara och industriella tillämpningar av artificiella fotosyntetiska anordningar är det viktigt att integrera molekyllära katalysatorer i fasta elektrodmaterial, och framsteg behöver göras i hur de molekyllära katalysatorerna immobiliseras på en fast elektrod. I denna avhandling övervägdes två möjliga strategier: immobilisering av komplexet i ett metallorganiskt ramverk (MOF) och dess immobilisering i en polymermatris. Arbetet fokuserar på en molekyllär koppar-katalysator med en tetra-amidatmakrocyclisk ligand (TAML), kallad [CuMac]²⁻, som kan isoleras som en (Me₄N)₂[CuMac] salt^[2]. Derivat av det organiska ligand ramverket, med antingen två ester- eller två karboxylsyrafunktionaliteter, syntetiserades för att möjliggöra immobilisering av [CuMac]²⁻. Föreningarna karakteriserades elektrokemiskt och spektroskopiskt och testades för deras OER-aktivitet vid olika pH värden. [CuMac]²⁻ har en anmärkningsvärd redox och strukturell robusthet vid neutralt pH tack vare makrocycliska effekten. Detta skiljer sig från andra övergångskomplex från första raden som ofta är strukturellt mer labila, vilket leder till nedbrytning och därmed deaktivering. Dock verkar införandet av karboxylgrupper vara kinetiskt

skadligt för OER-aktiviteten jämfört med $[\text{CuMac}]^{2-}$. Dessutom stötte man på syntetiska begränsningar som hämmade beredningen av $[\text{CuMac}]^{2-}$ -analogerna med linjärt arrangerade karboxylater, vilket skulle vara den krävda geometrin för att konstruera rätt ramverk för MOF formation.

I nästa kapitel presenteras en studie om identifiering av möjliga kortlivade mellanprodukter. Målet med denna avdelning var att få insikt in i den katalytiska mekanismen för $[\text{CuMac}]^{2-}$. När vattenoxiderationsreaktioner sker måste katalysatorn uppnå högre oxidationstillstånd för att uppfylla de fyra elektronöverföringarna som händer i en cykel. I fallet med $[\text{CuMac}]^{2-}$ uppnåddes detta med hjälp av den redox-icke-oskyddliga makrocycliska liganden. Mac^{4-} liganden är tetra-anjonisk i naturen och dess utökade π -delningsförmåga kan överföra och bevara radikala tillstånd för senare användning i den katalytiska cykeln. För att förstå de tidiga stegen i den katalytiska cykeln användes tidsupplöst UV-Vis spektroskopi för att härleda mekanismen för elektronöverföring och kinetiken för katalysatoroxidation. Vi använde en flash-fotolysmetod och $[\text{Ru}(\text{bpy})_3]\text{Cl}_2$ och persulfat som respektive fotosensibilisator och quencher för att samla bevis på en-elektron oxiderad katalysator och följande mellanprodukter som inte temporärt löstes med elektrokemiska medel.

För att följa utvecklingen av anodmaterial i fast form antog vi screentryckstekniker som under de senaste åren har möjliggjort lågkostnadsframställning av elektronik tack vare tryckning på polymera substrat. Exempel på sådana tillämpningar är solceller, lysdioder, transistorer, gasgivare och tryckta batterier [3-5]. Tryckta elektroder (PE) tillverkades med hjälp av grafit som ledande material, vilket gör att elektroderna lätt kan tillverkas, och en polymerbindare P(MMA-s-HEMA), dvs en statistisk co-polymer av metylmetakrylat, styren och hydroxietylmetakrylat som gjordes för ändamålet. Bindaren designades för att öka PE:s hydrofilicitet, en viktig faktor när man designar en vatten-elektrolysör eftersom gasformiga produkter (H_2 och O_2) måste lätt desorberas från ytan och lämna den elektroaktiva ytan tillgänglig för nästa cykel [6-8]. PE:erna funktionaliserades sedan kovalent med $[\text{CuMac}]^{2-}$ genom en in-situ elektroreduktion av det motsvarande bis(diazonium)-föreningen $(\text{N}_2)_2[\text{CuMac}]$ för att fästa det på elektrodytan. För detta modifierades den makrocycliska strukturen genom att införa aminmotiv för att göra det lämpligt att syntetisera diazoniumderivatet och efterföljande transplantation till grafitytan. Den resulterande katalysatorns aktivitet utvärderades genom cyklisk voltammetri och visade sig vara hämmad jämfört med $[\text{CuMac}]^{2-}$ i homogen lösning.

Till sist integrerade vi en molekylär vattenoxiderationskatalysator i en flödeselektrolysör som drivs av en perovskit/perovskit tandemsolcell för att driva vatten delning med ljus i en så kallad fotovoltaisk-elektrokemisk konfiguration (PV-EC) [9]. Vi

fokuserade på en molekylär ruteniumbaserad koordinationsoligomer vattenoxiderationskatalysator $[\text{Ru}(\text{bda})(4,4'\text{-bpy})_6(4,4'\text{-bpy})]$. Det har visats att katalysatorn etablerar CH- π interaktioner med grafiska ytor, vilket ger en hållbar förankringsstrategi ^[10]. Dessutom bildas en ny molekylär typ under katalysatoraktivering, som når en anmärkningsvärt hög strömtäthet vid neutral pH ^[10]. Vi uppnådde en driftspänning på 1,4 V och en sol-till-vätgasverkningsgrad (STH) på 12,5 %. Men stabiliteten hos systemet behöver förbättras eftersom vi observerade att vattenoxiderationskatalysatorn läcker ut från elektrolysören under långa experimentella villkor (> 12 h). Detta kan förbättras genom att ändra membranet som separerar de två elektrolytkompartementen, vilket bestämmer den lokala pH:n som omger katalysatorn, en väsentlig parameter för katalysatorns aktivitet, integritet och bindning.

REFERENCES

- [1] S. Berardi, S. Drouet, L. Francàs, C. Gimbert-Suriñach, M. Guttentag, C. Richmond, T. Stoll, A. Llobet, *Chem. Soc. Rev.* **2014**, 43, 7501–7519.
- [2] P. Garrido-Barros, D. Moonshiram, M. Gil-Sepulcre, P. Pelosin, C. Gimbert-Suriñach, J. Benet-Buchholz, A. Llobet, *J. Am. Chem. Soc.* **2020**, 142, 41, 17434–17446.
- [3] J. Wiklund, A. Karakoç, T. Palko, H. Yiğitler, K. Ruttik, R. Jäntti, J. Paltakari, *J. Manuf. Mater. Process.* **2021**, 5, 3, 89.
- [4] S. Khan, L. Lorenzelli, R. S. Dahiya, *IEEE Sens. J.* **2015**, 15, 6, 3164–3185.
- [5] O.-H. Huttunen, T. Happonen, J. Hiitola-Keinänen, P. Korhonen, J. Ollila, J. Hiltunen, *Ind Eng Chem. Res.* **2019**, 58, 19909–19916.
- [6] R. Sen, S. Das, A. Nath, P. Maharana, P. Kar, F. Verpoort, P. Liang, S. Roy, *Front. Chem.* **2022**, 10, 861604.
- [7] C. Meng, B. Wang, Z. Gao, Z. Liu, Q. Zhang, J. Zhai, *Sci. Rep.* **2017**, 7, 41825.
- [8] S. Tanaka, S. Takaya, T. Kumeda, N. Hoshi, K. Miyatake, M. Nakamura, *Int J Hydrogen Energy* **2021**, 46, 28078–28086.
- [9] T. J. Jacobsson, V. Fjällström, M. Edoff, T. Edvinsson, *Energy Environ. Sci.* **2014**, 7, 2056–2070.
- [10] M. Gil-Sepulcre, J. O. Lindner, D. Schindler, L. Velasco, D. Moonshiram, O. Rüdiger, S. Debeer, V. Stepanenko, E. Solano, F. Würthner, A. Llobet, *J. Am. Chem. Soc.* **2021**, 143, 30, 11651–11661.

SUMMARY (DUTCH)

De energiecrisis waar de samenleving momenteel mee kampt refereert naar de uitdaging om te kunnen voldoen aan de toenemende vraag naar energie met beperkte, en afnemende, fossiele brandstoffen die de belangrijkste energiebron zijn voor de huidige maatschappij. Naarmate de wereldbevolking groeit, neemt ook de behoefte energie om huizen, industrieën en transport te voorzien toe. Het gebruik van niet-hernieuwbare energiebronnen zoals kolen, olie en gas heeft echter geleid tot milieuproblemen zoals lucht- en watervervuiling, klimaatverandering en andere gezondheidsrisico's.

De afgelopen jaren is het besef om over te stappen op hernieuwbare energiebronnen, om de effecten van klimaatverandering tegen te gaan en de uitstoot van broeikasgassen te verminderen, gegroeid. Overheden, bedrijven en individuen investeren in hernieuwbare energie-infrastructuur en technologieën om een meer duurzame energietoekomst te creëren.

In dit proefschrift worden moleculaire complexen op basis van overgangsmetalen onderzocht voor de wateroxidatiekatalyse en geïntegreerd in waterstofsplitsingsapparaten. Wateroxidatie (WO) is een essentiële reactie in alle processen om chemische brandstoffen (bijv. waterstof, koolmonoxide, mierenzuur) uit water te produceren. Wanneer WO wordt aangedreven door zonlicht, wordt dit ook wel kunstmatige fotosynthese genoemd ^[1]. WO vereist doorgaans een hoge overspanning om de kinetische barrière te overwinnen die geassocieerd wordt met de vorming van O-O-bindingen en de meervoudige elektronoverdracht van de reactie.

Met schaalbare en industriële toepassingen van kunstmatige fotosynthetische apparaten in het vooruitzicht, is het essentieel om moleculaire katalysatoren in vastestof elektrodematerialen te incorporeren, waarbij vooruitgang moet worden geboekt in heterogenisatietechnieken. In dit proefschrift zijn twee mogelijke strategieën overwogen: de incorporatie van het complex in een metaalorganisch kader (MOF) en de immobilisatie ervan in een polymeermatrix. Het werk richt zich op een koperen moleculaire katalysator met een tetra-amidaat macrocyclische ligand (TAML), genaamd $[\text{CuMac}]^{2-}$, die geïsoleerd kan worden als een $(\text{Me}_4\text{N})_2[\text{CuMac}]$ zout ^[2]. Derivaten van het organische ligandskelet, met twee ester- of twee carboxylzuurfunctionaliteiten, werden gesynthetiseerd om de heterogenisatie van $[\text{CuMac}]^{2-}$ mogelijk te maken. De verbindingen werden elektrochemisch en spectroscopisch gekarakteriseerd en getest op hun OER-activiteit bij verschillende operationele pH-waarden. $[\text{CuMac}]^{2-}$ heeft bij neutrale pH een opmerkelijke redox- en structurele robuustheid dankzij het macrocyclische effect. Dit staat in contrast met andere overgangscomplexen op de eerste rij die vaak structureel labiel zijn en dus tot

afbraak en deactivatie leiden. De introductie van de carboxylgroepen lijkt echter kinetisch nadelig te zijn voor de OER-activiteit in vergelijking met die van de $[\text{CuMac}]^{2-}$. Bovendien werden er synthetische beperkingen ondervonden die de synthese van de $[\text{CuMac}]^{2-}$ -analogen met lineair gerangschikte carboxylaten belemmerden terwijl die de vereiste geometrie zouden hebben voor MOF-assemblage.

In het volgende hoofdstuk wordt een studie gepresenteerd waarbij mogelijke kortlevende tussenproducten worden geïdentificeerd. Het doel van dit hoofdstuk was om inzicht te krijgen in het katalytische mechanisme van $[\text{CuMac}]^{2-}$. Bij wateroxidatiereacties moet de katalysator hogere oxidatietoestanden bereiken om de vier-elektronenoverdracht per cyclus te voltooien. In het geval van $[\text{CuMac}]^{2-}$ werd dit bereikt met behulp van het redox-niet-innocente macrocyclische ligand. Het Mac^{4-} ligand is tetra-anionisch van aard en de uitgebreide π -distributie kan radicaal tussenproducten behouden voor later gebruik in de katalytische cyclus. Om de vroegtijdige stappen in de katalytische cyclus te begrijpen, werd UV-Vis-transiënte spectroscopie gebruikt om het elektronenoverdrachtmechanisme en de kinetiek van katalysatoroxidatie af te leiden. We gebruikten een flits-fotolysemethode, waarbij $[\text{Ru}(\text{bpy})_3]\text{Cl}_2$ en persulfaat respectievelijk als fotosensibilisator en donor werden gebruikt om bewijs te verzamelen van één-elektron-geoxideerde katalysator en tussenproducten die niet tijdelijk werden opgelost door elektrochemische middelen.

Om de ontwikkeling van vaste-anodematerialen voort te zetten, hebben we gebruik gemaakt van zeefdruktechnologieën die in de afgelopen jaren de productie van goedkope elektronica hebben gezorgd dankzij het drukken op polymeersubstraten. Voorbeelden van dergelijke toepassingen zijn zonnecellen, lichtgevend diodes, transistors, gasdetectoren en gedrukte batterijen^[3-5]. Gedrukte elektroden (PE) werden gefabriceerd met behulp van grafiet als geleidend materiaal, waardoor de elektroden gemakkelijk konden worden geproduceerd, en een polymeerbindmiddel P(MMA-s-HEMA), dat wil zeggen een statistisch copolymeer van methylmethacrylaat, styreen en hydroxyethylmethacrylaat, dat speciaal voor dit doel werd gemaakt. Het bindmiddel was ontworpen om de hydrofiliciteit van de PE's te vergroten. Dit was een belangrijke overweging bij het ontwerpen van een water-elektrolyseapparaat omdat de gasvormige producten (H_2 en O_2) gemakkelijk van het oppervlak moeten desorberen, waardoor het elektro-actieve oppervlak beschikbaar blijft voor de volgende omzettingscyclus^[6-8]. De PE's werden vervolgens covalent gefunctionaliseerd met $[\text{CuMac}]^{2-}$ door middel van een in-situ elektroreductie van de overeenkomstige bis(diazonium)-verbinding $(\text{N}_2)_2[\text{CuMac}]$ om aan het elektrodeoppervlak te verankeren. Hiertoe werd het macrocyclische skelet gewijzigd door aminegroepen toe te voegen om het geschikt te maken voor de synthese van het diazoniumderivaat en de daaropvolgende enting op

het grafietoppervlak. De activiteit van de resulterende geheterogeniseerde katalysator werd geëvalueerd door cyclische voltammetrie, waarbij werd vastgesteld dat deze werd belemmerd in vergelijking met [CuMac]²⁻ in homogene oplossingsfase.

Ten slotte hebben we een op moleculen gebaseerde wateroxidatiekatalysator geïntegreerd in een perovskiet/perovskiet tandem-zonnecel aangedreven flow-elektrolyser om de waterstofsplitsing door licht te bevorderen door middel van een zogenaamde fotovoltaiisch-elektrochemische configuratie (PV-EC) ^[9]. We hebben ons hierbij gericht op een moleculaire rutheniumgebaseerde coördinatie-oligomeerwateroxidatiekatalysator [Ru(bda)(4,4'-bpy)]₆(4,4'-bpy). Er is aangetoond dat de katalysator CH- π -interacties aangaat met grafietoppervlakken, wat een duurzame verankeringsstrategie biedt ^[10]. Bovendien wordt er tijdens de activering van de katalysator een nieuwe moleculaire specie gevormd, die bij neutrale pH een opmerkelijk hoge stroomdichtheid bereikt ^[10]. We hebben een operationele spanning van 1,4 V en een zon-naar-waterstofefficiëntie (STH) van 12,5 % bereikt. De stabiliteit van het systeem moet echter nog worden verbeterd, sinds er is waargenomen dat de wateroxidatiekatalysator onder langdurige experimentele omstandigheden (> 12 uur) uit de lekt. Dit kan worden verbeterd door het membraan die de twee elektrolytcompartimenten scheidt te veranderen, wat de lokale pH rond de katalysator bepaalt, een essentiële parameter voor de katalysatoractiviteit, -integriteit en -binding.

REFERENCES

- [1] S. Berardi, S. Drouet, L. Francàs, C. Gimbert-Suriñach, M. Guttentag, C. Richmond, T. Stoll, A. Llobet, *Chem. Soc. Rev.* **2014**, 43, 7501–7519.
- [2] P. Garrido-Barros, D. Moonshiram, M. Gil-Sepulcre, P. Pelosin, C. Gimbert-Suriñach, J. Benet-Buchholz, A. Llobet, *J. Am. Chem. Soc.* **2020**, 142, 41, 17434–17446.
- [3] J. Wiklund, A. Karakoç, T. Palko, H. Yiğitler, K. Ruttik, R. Jäntti, J. Paltakari, *J. Manuf. Mater. Process.* **2021**, 5, 3, 89.
- [4] S. Khan, L. Lorenzelli, R. S. Dahiya, *IEEE Sens. J.* **2015**, 15, 6, 3164–3185.
- [5] O.-H. Huttunen, T. Happonen, J. Hiitola-Keinänen, P. Korhonen, J. Ollila, J. Hiltunen, *Ind Eng Chem. Res.* **2019**, 58, 19909–19916.
- [6] R. Sen, S. Das, A. Nath, P. Maharana, P. Kar, F. Verpoort, P. Liang, S. Roy, *Front. Chem.* **2022**, 10, 861604.
- [7] C. Meng, B. Wang, Z. Gao, Z. Liu, Q. Zhang, J. Zhai, *Sci. Rep.* **2017**, 7, 41825.
- [8] S. Tanaka, S. Takaya, T. Kumeda, N. Hoshi, K. Miyatake, M. Nakamura, *Int J Hydrogen Energy* **2021**, 46, 28078–28086.
- [9] T. J. Jacobsson, V. Fjällström, M. Edoff, T. Edvinsson, *Energy Environ. Sci.* **2014**, 7, 2056–2070.
- [10] M. Gil-Sepulcre, J. O. Lindner, D. Schindler, L. Velasco, D. Moonshiram, O. Rüdiger, S. Debeer, V. Stepanenko, E. Solano, F. Würthner, A. Llobet, *J. Am. Chem. Soc.* **2021**, 143, 30, 11651–11661.

CURRICULUM VITAE

Ludovico Riccardi was born on January 30th, in Verbania, Italy where he grew up. After finishing his secondary education at Istituto Tecnico L. Cobianchi in Verbania, he pursued his B.Sc. studies in 2012 at the University of Pavia in Chemistry. He continued his M.Sc. at the same university, completing his graduation project in 2017, at Rheinische Friedrich-Wilhelms-Universität Bonn, Germany, within the Erasmus program. During that period, he worked on the intramolecular radical arylation of epoxides catalyzed by electro-activated titanium complexes under prof. dr. Andreas Gansäuer. In 2018 he started his Ph.D. within the eSCALED project, a European program funded by the Horizon 2020 Marie-Sklodowska-Curie Actions Innovative Training Network, aimed to contribute to the artificial photosynthesis technology to produce solar fuels from water from renewable energy sources. His work concerned the study and development of molecular-based catalysts for water oxidation under the supervision of prof. dr. Sascha Ott and prof. dr. ir. René Janssen.

ACKNOWLEDGMENTS

Completing this PhD has been an incredible journey that has taken me across Europe, allowing me to meet amazing people along the way. I cannot express enough how grateful I am for this experience and for the support and help of so many individuals who made this journey possible.

First and foremost, I would like to thank my thesis advisors, *René Janssen* from Eindhoven University and *Sascha Ott* from Uppsala University, whose guidance and enthusiasm made this journey a remarkable one. *Rene*, thanks for all the input, feedback, and energy, even when the research I was bringing to the table was not your expertise. You truly showed interest and dedication. Also, thanks for all the comments and edits you provided during the writing of this thesis. *Sascha*, thanks for your support and scientific discussions during these last four years and also for your care, both professionally and personally. Your positive energy is contagious and creates a vibrant atmosphere within your group.

I am also grateful to those who actively organized the eSCALED project and made it possible, particularly to *Laia Francesch* and *Antoine Bousquet*, who put much effort and time into coordinating twelve different institutes and supported us, PhDs, during these last few years in our nomad lifestyle, existential crisis, and bureaucratic processes. My thanks also go to my fellow students within the program, *Domenico*, *Robin*, *Andrew*, *Bruno*, *Olivera*, *Saeed*, *Naomi*, *Ignazi*, *Andy*, *Silvia*, *Afridi*, *Diogo*, and *Van*. Some of which I spent more or less time in the labs or in spare time activities; nonetheless, we all bound since our very first meeting in the struggle of our program.

I would like to extend my gratitude to the people I met during my stay in ICIQ, Tarragona. Firstly, to *Antoni Llobet* and *Carolina Gimbert*, to co-supervise my work throughout my first year's work. My PhD could not have started in a better way due to the people from this group. Particularly, I am thankful to *Marta* and *Nataliia*. We had a great connection from the first day and many adventures; your enthusiasm reflected the spirit of the group. Next in line is *Dr. Marcus* (!), who, other than being the sexiest doctor, patiently showed me the more elaborate electrochemical setups and was always available to discuss science even after my departure. I cannot omit his obsession with changing monitor wallpapers with the grossest images. All very funny until you realized that it was your computer. A special thank is to *Primavera* for her "good morning" faces and for proving that not every Italian is cut out for cooking since she mastered two main dishes: lentils soup in winter and gazpacho in summer. Thanks to the rest of the group, namely *Jan*, *Jan II*, *Sergi*, and *Martina*, for the atmosphere and cooperation in the lab

and for sharing your expertise and providing continuous assistance. Thanks to the routine tapas, which chronically would end up dancing at Cau or on the beach. Also, a big thanks to many of them being my extended climbing family with the addition of *Joan, Cristina, and Rosie*. Every weekend was an opportunity to explore the Catalan mountains and enjoy rock, nature, and good company.

I would like to thank *Leif Hammarström*, who gave me the chance to work in his labs and co-supervised my research during my permanence at Uppsala University. Thanks to *Nidhi* and *Robin* for introducing me to nanosecond laser spectroscopy and its setup. Even though the initial trauma from moving from Spain to Sweden, people made the transitions so much enjoyable that I almost forgot the absence of sun for six months. Particular thanks go to *Starla, Nicoo, and Dani* for being tenacious buddies in climbs and late clubbing taking place in either Stockholm or in random Swedish forests. We shared many passions and we had such a great time together, I am grateful our paths crossed in Uppsala. Thanks to *Anna, Leon, Brian, Kate, Kelly, and Manuel* for more outdoor adventures, hikes, and ski trips. Also, I would like to thank the rest of the people in *Ångström hus 7, Emilie, Maxime, Hemlata, Ben, Anna, Martin, Astrid, Belinda, Sigrid, Sara, Timofey, Salauat, Moritz, Luca, Mariia, Sergei, Alenka, Andrea*. Each of you brought positive vibes and made the stay in Sweden brighter.

My secondment in France at IPREM, although brief, was intense, taking into account the pandemic and other restrictions related to it. I want to thank *Laurent Billon*, to co-supervised the work done during that time, and *Pierre*, who really assisted me and introduced me to practical procedures and lab instruments from day zero. Once again, I would like to thank *Laia*, who incessantly helped with paperwork and administration, proving that the Italian bureaucracy is not the only one to be quite bad. I also want to thank *Domenico*, who had me over to his apartment for dinners and social activities as an adopted housemate, regardless of the ongoing restrictions and possible fines. One thanks also go to the eSCALED *tiny house crew*, namely *Silvia, Andy, Andrew, and Bruno*, who made the time much more bearable in that situation, with pâté, wine, and bread knives being the heart of most evenings.

My last stay took place in Eindhoven. Thus, I want to express my gratitude to the members of the M2N group. Thank you, *Martijn, Nicolas, Bruno, and Wietse*, for all the discussion during the synthesis meetings, which quickly enough became unofficially the electrochemistry meetings. Also, thanks to *Stefan*, you showed me the time-resolved photoluminescence set-up I used for my experiments. I need to thank *Alessandro*, who, despite being the most annoying officemate, he was also the best *pizzaiolo* in Eindhoven. I could not give that up easily. I am proud I got you obsessed with climbing and I hope we will find the occasion to go on real rock sometimes. I want to thank *Margot*

for her aid and availability, spanning from moving to Eindhoven during a not-an-easy time to all the administrative processes. A big thanks also to the rest of the group, *Kunal, Simone, Willemijn, Lana, Tom, Junke, Bas, Peter, Guus, Laura, Lois, Xiao, Riccardo, Cristoph, Mahyar*, for all the nice conversations and the (too) many coffee breaks. I can definitely say you all taught me something about solar cells, even though I have never fabricated one myself.

Finally, I cannot express enough how thankful I am to Starla. Simply meeting you would have been a great reason alone to enroll in this program, and I'm so glad I did. Your limitless energy and love for all beings make you a true superwoman. Thank you for providing emotional support over the years and for sharing your scientific expertise when necessary.

Last but not least, voglio ringraziare la mia famiglia, per il loro sostegno, amore durante il mio percorso accademico. Grazie in particolar modo a mia *Madre*, che dandomi la possibilità di studiare e incoraggiandomi costantemente ha reso possibile che raggiungessi questo traguardo. Contrariamente allo stereotipo italiano, ha sempre sostenuto che lasciassi il paese per inseguire nuove opportunità ed espandere le mie esperienze. Grazie ai miei zii *Claudia, Alfonso e Riccardo* per il loro supporto durante questi ultimi anni, che sono stati tutt'altro che facili, ma anche per riuscire a sdrammatizzare in queste situazioni. Non troverete nessuna scoperta del secolo qui, dovrete aspettare il prossimo dottorato per quello. I miei ultimi pensieri vanno a mio *Padre*, immaginando quanto possa essere orgoglioso di questo mio traguardo raggiunto.

Acta Universitatis Upsaliensis

Digital Comprehensive Summaries of Uppsala Dissertations from the Faculty of Science and Technology 2276

Editor: The Dean of the Faculty of Science and Technology

A doctoral dissertation from the Faculty of Science and Technology, Uppsala University, is usually a summary of a number of papers. A few copies of the complete dissertation are kept at major Swedish research libraries, while the summary alone is distributed internationally through the series Digital Comprehensive Summaries of Uppsala Dissertations from the Faculty of Science and Technology. (Prior to January, 2005, the series was published under the title "Comprehensive Summaries of Uppsala Dissertations from the Faculty of Science and Technology".)



Distribution: publications.uu.se
urn:nbn:se:uu:diva-501240

ACTA UNIVERSITATIS
UPSALIENSIS
2023